

TIME-DEPENDENT SEARCHES FOR NEUTRINO POINT SOURCES WITH  
THE ICECUBE OBSERVATORY

*by*

MICHAEL FRANCIS BAKER

A dissertation submitted in partial fulfillment of the  
requirements for the degree of

DOCTOR OF PHILOSOPHY  
(PHYSICS)

*at the*

UNIVERSITY OF WISCONSIN – MADISON

2011

© 2011 Michael Francis Baker

All Rights Reserved

## Abstract

The IceCube Neutrino Observatory is a  $\text{km}^3$  detector which completed construction at the geographic South Pole in December 2010. Here we present several searches for flaring point-sources of neutrinos using IceCube data using maximum-likelihood techniques. For the first time, a search is performed over the entire parameter space of energy, direction and time with sensitivity to neutrino flares lasting between  $20 \mu\text{s}$  and a year from astrophysical sources. This work is also an important step for the IceCube experiment in utilizing a multi-messenger approach, driving IceCube neutrino analysis with information from photon observatories. Timing information is useful since integrated searches over time are less sensitive to flares as they are affected by a larger background of atmospheric neutrinos and muons that can be reduced by the use of additional timing information. Flaring sources considered here, such as active galactic nuclei and gamma-ray bursts, are promising candidate neutrino emitters.

One search is "untriggered" in the sense that it looks for any possible flare of different time scales in the entire sky. Two other searches are triggered by multi-wavelength information on flares. One triggered search uses light curves from Fermi-LAT which provides continuous monitoring. A second triggered search uses information where the flux states have been measured only for short periods of time near the flares. Finally, a search for periodic emission of neutrinos is also performed on binary systems in the galaxy which are thought to be sources of particle acceleration. The searches use data taken by 40 strings of IceCube between Apr 5, 2008 and May 20, 2009 and by 59 strings of IceCube between May 20, 2009 and May 31, 2010. The results from all searches are compatible with a fluctuation of the background.





## Acknowledgements

There are a number of people who have been instrumental in making this work possible. First, I would like to thank my advisor, Teresa Montaruli, for her time, energy, and enthusiasm for high-energy astrophysics. Thanks to Chad Finley for introducing me to the world of likelihood analysis and for his steady and curious nature which has been an inspiration throughout.

I owe many thanks to Jon Dumm, Juanan Aguilar, Naoko Kurahashi, and Jim Braun. Working with them on myriad different point-source analyses over the years in Madison has been a pleasure. Thanks also to my office-mates Nathan Whitehorn and Laura Gladstone for their conversations and help with things large and small. Thanks to Reina Mauryama for the opportunity to be involved with DOM testing in Madison and at the South Pole. Thanks also to the IceCube collaboration as a whole for their astounding efforts which make this and many other analyses possible.

I also am grateful to for my parents, Jack and Shelly for their support over the years and the opportunities that support gave me. I would also like to thank my wife Michelle for coming with me to Madison and for her encouragement, which has made all the difference in making this possible.

# Contents

<b>Abstract</b>	<b>i</b>
<b>Acknowledgements</b>	<b>iii</b>
<b>1 Neutrinos and Neutrino Astronomy</b>	<b>1</b>
1.1 The Neutrino . . . . .	2
1.2 Lepton Propagation . . . . .	3
1.2.1 Electrons . . . . .	4
1.2.2 Muons . . . . .	4
1.2.3 Taus . . . . .	4
1.2.4 Čerenkov radiation . . . . .	5
1.3 Cosmic Rays . . . . .	6
1.3.1 Cosmic Ray Acceleration . . . . .	9
1.3.2 Cosmic Ray Air Showers . . . . .	11
1.3.2.1 Atmospheric Neutrinos . . . . .	11
1.4 Neutrino Oscillations . . . . .	12
<b>2 Candidate Sources of Flaring Neutrino Emission</b>	<b>16</b>

2.1	Extra-Galactic Source Candidates . . . . .	17
2.1.1	Active Galactic Nuclei . . . . .	17
2.1.2	Gamma-Ray Bursts . . . . .	22
2.2	Galactic Source Candidates . . . . .	23
2.2.1	Supernova Remnants . . . . .	23
2.2.2	Soft Gamma-Ray Repeaters . . . . .	25
2.2.3	Microquasars and Binary Objects . . . . .	26
2.3	Acceleration potential of sources . . . . .	28
<b>3</b>	<b>Multi-Wavelength Observations</b>	<b>30</b>
3.1	Optical Monitoring of Blazars . . . . .	32
3.2	High Energy Photon Observatories . . . . .	33
3.2.1	Swift Gamma-Ray Burst Mission . . . . .	35
3.2.2	Fermi Gamma-Ray Space Telescope . . . . .	35
3.2.3	Ground-Based Observatories . . . . .	37
3.2.3.1	Imaging Atmospheric Čerenkov Telescopes . . . . .	39
3.2.3.2	Water Čerenkov Detectors . . . . .	39
<b>4</b>	<b>The IceCube Detector</b>	<b>41</b>
4.1	Digital Optical Module . . . . .	42
4.2	Trigger and Data Acquisition . . . . .	45
4.3	Optical properties of the South Pole Ice . . . . .	48
4.4	Data Filtering . . . . .	50
<b>5</b>	<b>IceCube Event Reconstruction</b>	<b>55</b>

5.1	Hit Cleaning . . . . .	55
5.2	Track Reconstructions . . . . .	56
5.2.1	Line Fit First-Guess Reconstruction . . . . .	57
5.2.2	Maximum Likelihood Track Reconstruction . . . . .	58
5.2.2.1	Pandel Function . . . . .	59
5.2.2.2	Single Photo-Electron . . . . .	59
5.2.2.3	Multiple Photo-Electron . . . . .	60
5.2.2.4	Paraboloid Fit . . . . .	61
5.2.2.5	Bayesian Track Reconstruction . . . . .	61
5.3	Coincident Muons . . . . .	63
5.3.1	Split Track Reconstructions . . . . .	63
5.3.2	Topological Trigger Hit Cleaning . . . . .	64
5.4	Energy Reconstruction . . . . .	65
<b>6</b>	<b>The 40 and 59-string Datasets</b>	<b>67</b>
6.1	Event Selection Techniques . . . . .	68
6.2	Data Selection . . . . .	69
6.2.1	40-string Event Selection . . . . .	71
6.2.2	59-string Event Selection . . . . .	73
6.2.2.1	Up-going region of 59 strings . . . . .	73
6.2.2.2	Down-going region of 59 strings . . . . .	76
<b>7</b>	<b>Analysis Method</b>	<b>80</b>
7.1	Maximum Likelihood Method . . . . .	80
7.2	Event Weight . . . . .	84

7.2.1	Local Coordinate Dependence . . . . .	87
7.3	Combining Datasets . . . . .	89
7.4	Sensitivity and Discovery Potential . . . . .	90
7.5	Systematic Errors . . . . .	92
<b>8</b>	<b>Simulation and Detector Performance</b>	<b>95</b>
8.1	Simulation Chain . . . . .	96
8.1.1	Neutrino Simulation . . . . .	96
8.1.2	Cosmic Ray Simulation . . . . .	96
8.1.3	Propagation . . . . .	97
8.1.4	Detector Simulation . . . . .	97
8.2	Detector Performance . . . . .	98
8.2.1	Neutrino Point Spread Function . . . . .	98
8.2.2	Neutrino Effective Area . . . . .	100
<b>9</b>	<b>All-Sky Time-Scan</b>	<b>102</b>
9.1	Method and Expected Performance . . . . .	103
9.2	Results . . . . .	108
<b>10</b>	<b>Triggered Searches for Flares of Neutrino Point Sources</b>	<b>115</b>
10.1	Triggered Searches Based on Continuous Photon Observations . . . . .	116
10.1.1	Method and Expected Performance . . . . .	116
10.1.2	Results . . . . .	119
10.2	Triggered Searches Based on Intermittent Photon Observations . . . . .	133
10.2.1	Method and Expected Performance . . . . .	133

10.2.2 Results . . . . .	134
<b>11 Periodic Emission Search</b>	<b>135</b>
11.1 Method and Expected Performance . . . . .	136
11.2 Results . . . . .	137
<b>12 Conclusions</b>	<b>141</b>
12.1 Summary . . . . .	141
12.2 Outlook . . . . .	142

# Chapter 1

## Neutrinos and Neutrino Astronomy

The field of neutrino astronomy is still very young, and stands to provide a new window on the universe. Many of the candidate sources of high-energy neutrinos are still poorly understood, they also exhibit wild fluctuations in energy output on many different time scales.

High-energy neutrinos can be produced by the interaction of the high-energy protons with matter or photon fields. Neutrinos are unique astrophysical messengers, as they have no charge and interact weakly, traveling directly from their point of creation essentially without absorption. This differentiates them from cosmic rays which will be deflected by magnetic fields and high energy photons which can be strongly absorbed. Neutrinos are key in understanding the mechanisms of cosmic ray acceleration, and their detection from an astrophysical point source would be a clear indication of hadronic acceleration in that source. This chapter covers the relationship of cosmic ray interactions to neutrinos.

One of the major challenges in understanding the properties of neutrinos and the development of neutrino astronomy is their small interaction cross-sections. In order to build up sufficient statistics, neutrino telescopes must have an enormous volume instrumented, on the order of a cubic kilometer. Natural bodies of water or clear ice can be used as a

target medium, light from the neutrino interaction products can also be measured in such a detector.

## 1.1 The Neutrino

Neutrinos are subatomic particles which interact only via the weak nuclear force. They were first theorized to explain the spectrum of electron energies created in beta-decay nuclear processes in 1930 [1]. They were first discovered in 1956 by observing electron neutrino capture producing positrons [2].

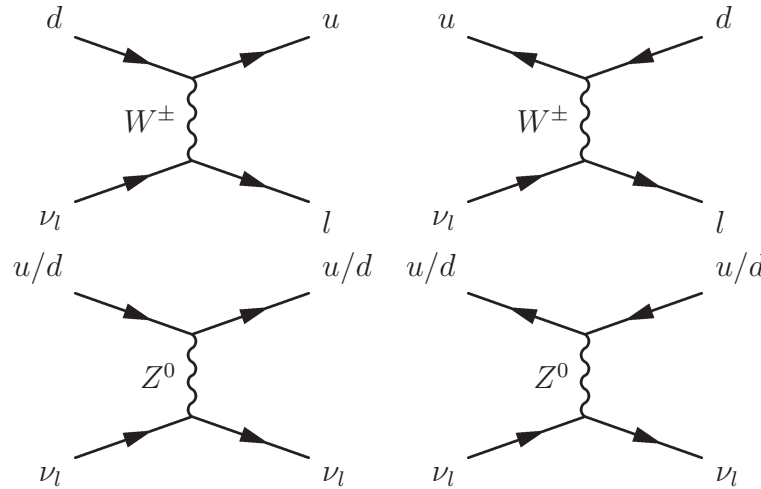


Figure 1.1 Feynman diagrams for the neutrino-quark charged-current (top row) and neutral-current interactions (bottom row).

Neutrino interactions with atomic nuclei have two primary modes: charged-current (CC) and neutral-current (NC). In charged-current interactions, the incident neutrino is replaced by an outgoing charged lepton in a reaction mediated by a  $W$  boson. Neutrinos are typically detected through charged-current interactions, where a neutrino with flavor  $l$  (or anti-neutrino  $\bar{\nu}_l$ ) undergoes a charged-current interaction with a nucleus and produces a



charged lepton with flavor  $l^-$  (or a charged anti-lepton  $l^+$ ):

$$\nu_l(\bar{\nu}_l) + q \rightarrow l^\mp + q' \quad (1.1)$$

where  $q$  is a quark in the nucleus and  $q'$  is a quark of a different flavor.

Neutral current interactions feature the neutrino recoiling off of the nucleus, mediated by a Z boson. The Feynman diagrams for CC and NC interactions can be seen in Figure 1.1. There is also the interaction of anti-electron neutrinos with electrons  $\bar{\nu}_e + e^- \rightarrow W^-$ , which has a resonance at neutrino energies of 6.3 PeV. Analogous interactions with muon and tau flavors are possible, but are not practical for neutrino astronomy.

For NC interactions, there will be a shower of photons from the hadronic cascade, which can be seen if within the detector volume. In this thesis CC interactions are the focus, specifically those of muon (anti-)neutrinos. Since IceCube does not have a magnetic field strong enough to distinguish leptons from anti-leptons, we refer to particles e.g. anti-muons and muons as simply muons throughout. Muons created by high-energy neutrino interactions can travel for tens of kilometers before decaying. Electrons, by comparison, will lose their energy over several meters, and using the reconstruction techniques of IceCube are currently indistinguishable from a NC cascade.

## 1.2 Lepton Propagation

Leptons lose energy as they travel due to pair production, ionization, stochastic losses due to bremsstrahlung, and photo-nuclear interactions. These contribute in different amounts depending on the lepton energy before, in the case of a muon or a tau, it decays and produces another shower.

### 1.2.1 Electrons

Above 1 GeV the energy losses from electrons are mainly due to Bremsstrahlung radiation [3]. The energy is lost within a few meters water equivalent (mwe), making it a point-like source of light compared to the scales of neutrino telescopes. Energy reconstruction is possible, but directional information is lost with scattering lengths typical of the South Pole ice.

### 1.2.2 Muons

Due to the larger mass of the muon, energy losses per mwe are smaller than that of electrons, so their energy can be lost over much longer track distances. At energies below the muon critical energy of 1 TeV in water (similar for ice) [4] to energies below IceCube can resolve a muon track, ionization losses dominate, producing a continuous track of 200 MeV per mwe. Above this energy, stochastic losses become more prevalent, which are proportional to the muon energy. The energy loss per unit distance can be modeled as:

$$-\frac{dE}{dx} = a + bE, \quad (1.2)$$

where  $a$  is the ionization losses of 0.268 GeV per mwe and  $b$  is the stochastic loss term which is roughly  $3.6 \times 10^{-4}$  per mwe in ice. This yields track lengths for TeV energy muons which are roughly 2.5 km, above 1 TeV the length increases logarithmically, and at 1 PeV the typical distance is  $\sim 20$  km. This means that IceCube is sensitive to muons due to interactions far outside of the instrumented volume.

### 1.2.3 Taus

Tau energy losses per mwe are even less than that of muons, but due to the particle's  $2.9 \times 10^{-13}$  s lifetime, typical propagation lengths are much shorter for similarly energetic

particles. The particle's decay will reproduce a tau neutrino along with a cascade of light due to the daughter lepton or meson. This gives taus a "double-bang" topology, where there will be initial cascades when the tau is created and later decays, with a connecting track from Čerenkov radiation, which could be resolved if the tau travels a few hundred meters (expected of taus with energy  $\geq 1$  PeV). Taus with  $\geq 30$  PeV will experience extreme enough time dilation for them to travel roughly 1 km, far enough to travel through IceCube with a signature of a less energetic muon. The branching ratio to decay to a muon is 17.7%, so it is also possible for the daughter muon to be detected by a neutrino telescope.

#### 1.2.4 Čerenkov radiation

When a charged particle moves faster than  $c/n$ , where  $n$  is the index of refraction of the medium, the particle's radiation forms a coherent front (see Figure 1.2). This wavefront will propagate at a specific angle determined by the index of refraction at a specific wavelength  $n(\lambda)$  and the speed  $\beta = v/c$ :

$$\cos \theta_c = \frac{1}{\beta n(\lambda)}. \quad (1.3)$$

For particles with energies used in this work, particles have  $v/c \sim 1$ , and the index of refraction of ice  $n_{\text{ice}} = 1.32$ , yielding  $\theta_c \sim 41^\circ$ . The wavelength distribution of Čerenkov photons is given by the Franck-Tamm formula:

$$\frac{d^2 N}{dx d\lambda} = \frac{2\pi\alpha}{\lambda^2} \left( 1 - \frac{1}{\beta^2 n^2(\lambda)} \right), \quad (1.4)$$

where  $\alpha$  is the fine structure constant. The distribution is peaked at shorter wavelengths, giving Čerenkov light a bluish color. Taking the integral of Equation 1.4 from 365 nm to 600 nm yields 210 photons per centimeter, where the wavelength limits are chosen to reflect the glass and ice transparency.

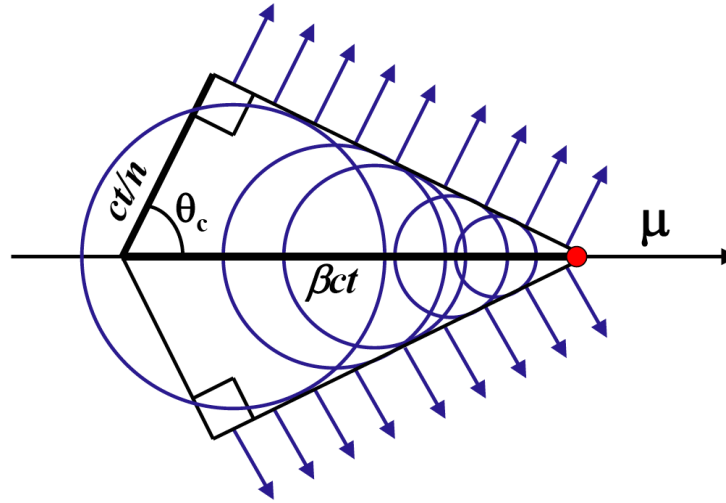


Figure 1.2 Illustration of Čerenkov emission. While a particle travels  $\beta ct$  in a time  $t$ , its emitted light only travels  $ct/n$ , forming a coherent front in a cone around the direction of motion. Use of this directionality is used in the reconstruction of the particle's properties.

### 1.3 Cosmic Rays

The Earth is constantly bombarded with charged particles from space, predominantly protons, but also heavier nuclei, electrons, positrons and photons. Ionizing radiation was discovered to be coming from space in 1912 by Victor Hess, who discovered that an electroscope will discharge faster at high altitudes than at sea level when he ascended in a hot air balloon up to altitudes of 5.3 km.

In the one hundred years since Hess's discovery, cosmic rays from energies of  $10^9$  eV up to  $10^{20}$  eV have been measured using a variety of detection mechanisms from balloon and satellite-borne detectors to arrays covering thousands of square kilometers to detect extensive air showers from cosmic rays interacting with particles in the atmosphere. The

spectrum follows a power-law spectrum for energies above 1 GeV:

$$\frac{dN}{dE} \propto E^{-\gamma}, \quad (1.5)$$

where  $\gamma$  is the power-law index of the spectrum. There are several interesting structures in the cosmic ray spectrum (Figure 1.3) in addition to a turnover at low energies due to the solar wind: there is a steepening in the spectral index at approximately 3 PeV in primary energy, called the "knee" of the spectrum; at several EeV the spectrum hardens to an  $E^{-3.1}$  spectrum, called the "ankle". The cosmic ray spectral indices  $\gamma$  for different energy ranges of interest are [5]:

$$\gamma = \begin{cases} 2.67 & \log(E/\text{GeV}) < 6.4, \\ 3.10 & 6.4 < \log(E/\text{GeV}) < 9.5, \\ 2.75 & 9.5 < \log(E/\text{GeV}). \end{cases} \quad (1.6)$$

Finally, for energies above 60 EeV, the spectrum steepens sharply.

The cause for the steepening of the cosmic ray spectrum for particles above 3 PeV could be due to particles escaping the confines of the galaxy, or it could be due to a petering out of the galactic cosmic ray accelerators (i.e. an inability to accelerate above the knee). It is believed that at the ankle, there is a transition from galactic objects to more powerful extra-galactic sources as the primary accelerators. The steepening above 60 EeV is evidence of the cutoff predicted by Greisen, Zatsepin and Kuzmin (GZK, [7, 8]), where protons above the energy threshold for photo-pion production with the cosmic microwave background will lose energy due to that mechanism as they travel (see Equation 1.7).

Protons and other nuclei are the primary component of cosmic rays; electrons and positrons form a smaller contribution. The relative ratios of protons to heavier nuclei across the spectrum is still an active area of research but there are hints that the fraction of heavy nuclei rises above EeV energies [9]. Some models for the knee use spectral breaks at different energies for each species of nucleus as energies grow too large for galactic objects

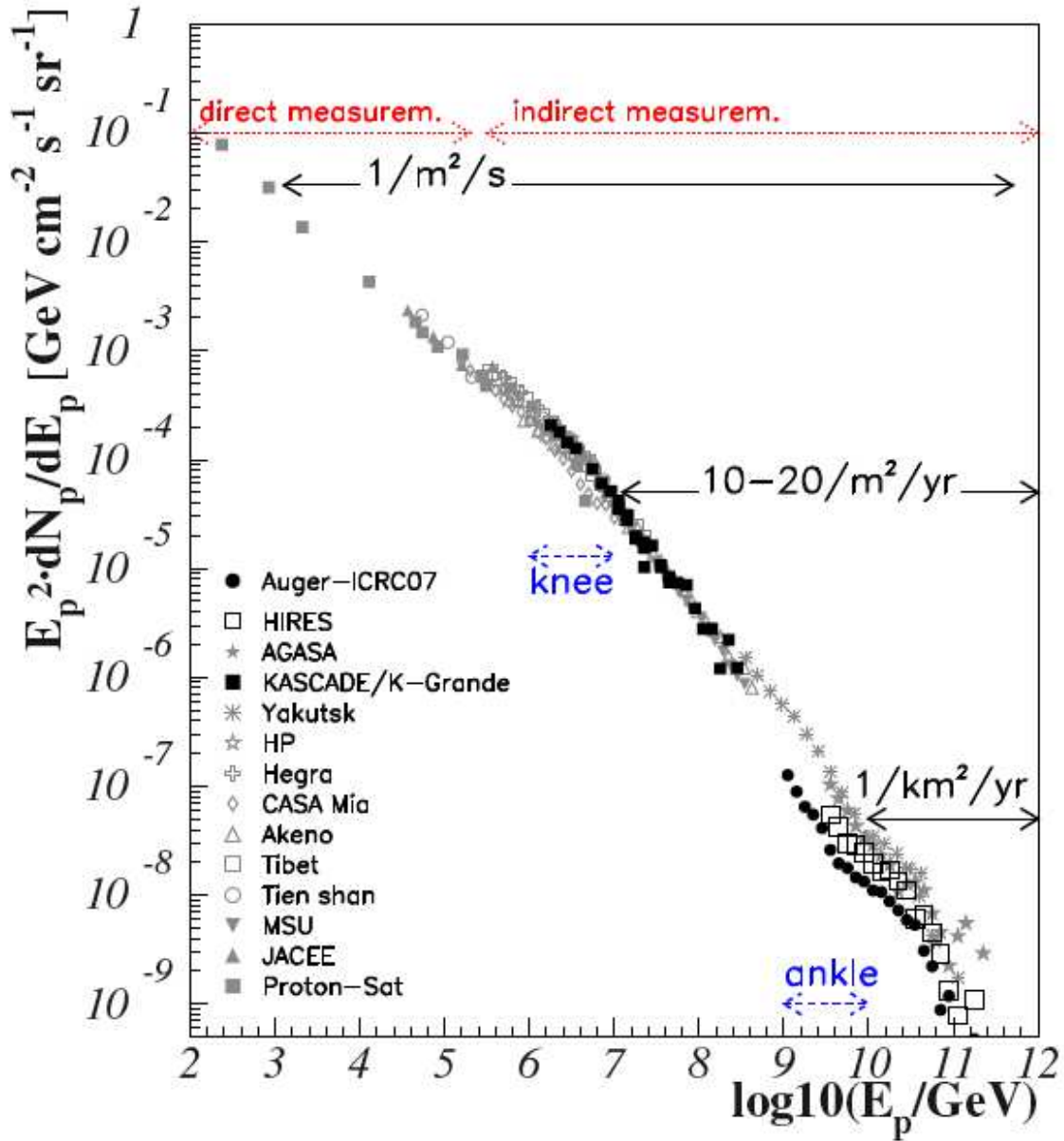


Figure 1.3 The cosmic ray energy spectrum measured by a number of different experiments. The cosmic ray flux has been multiplied by  $E^2$  to enhance features such as the knee and ankle, which are marked. Figure from [6] and references therein.

to accelerate or become unconfined in the galaxy (e.g. the poly-gonoto or "many-kneed" model).

At TeV energies, deflection in the galactic magnetic fields make the arrival directions for cosmic rays nearly isotropic, though a small ( $10^{-4}$ ) anisotropy exists, though it is not known what is the cause [10, 11]. It may be due to a nearby accelerator, or it may be due to structures in the galactic magnetic field near the solar system, or even the heliotail structure in the Sun's magnetic field.

### 1.3.1 Cosmic Ray Acceleration

Fermi acceleration is thought to be the most promising candidate for the acceleration mechanism of cosmic rays. The expectation is that charged particles are accelerated through a series of interactions across a relativistic shock front. These particles are confined to the shock due to inhomogeneities in the magnetic field, and are given energy with each pass through the shock front. This idea was first presented by Fermi [12, 13], and further developed by others [14, 15, 16]. The resulting particle spectra follow a power-law close to  $E^{-2}$ . Detailed calculations show, however, that depending on the shock conditions, the spectra can also be somewhat flatter or steeper, see e.g. [17, 18]. Here, we use an  $E^{-2}$  spectrum as a first order estimate.

Neutrinos will be produced in interaction with the accelerated particles in the dense region. The initial nuclear reactions produce charged and neutral pions in the following

reactions:

$$p\gamma \rightarrow \Delta^+ \quad (1.7)$$

$$\Delta^+ \rightarrow p + \pi^0$$

$$\Delta^+ \rightarrow n + \pi^+$$

$$n\gamma \rightarrow \Delta^0 \quad (1.8)$$

$$\Delta^0 \rightarrow p + \pi^-$$

$$\Delta^0 \rightarrow n + \pi^0$$

$$pp \rightarrow p + p + \pi^0 \quad (1.9)$$

$$p + n + \pi^+$$

$$pn \rightarrow p + p + \pi^- \quad (1.10)$$

$$p + n + \pi^0$$

Once the pions are produced, the charged species will overwhelmingly decay to muons and neutrinos, while neutral pions decay to gamma-rays which can be observed in GeV energies:

$$\pi^+ \rightarrow \mu^+ + \nu_\mu \quad (1.11)$$

$$\mu^+ \rightarrow e^+ + \nu_e + \bar{\nu}_\mu$$

$$\pi^- \rightarrow \mu^- + \bar{\nu}_\mu \quad (1.12)$$

$$\mu^- \rightarrow e^- + \bar{\nu}_e + \nu_\mu$$

$$\pi^0 \rightarrow \gamma\gamma \quad (1.13)$$



This results in a flavor ratio of neutrinos produced by pions to be  $\nu_e : \nu_\mu : \nu_\tau = 1 : 2 : 0$  at the source.

### 1.3.2 Cosmic Ray Air Showers

The main source of muons seen by IceCube is from cosmic rays in both the Northern and Southern hemispheres (up-going and down-going regions, respectively). High energy cosmic rays collide with atoms in the atmosphere, creating extensive air showers of photons, electrons, muons, pions, kaons and neutrinos (see Figure 1.4). IceCube detects mainly muons produced in air showers in the atmosphere above the South Pole, but it also detects muons from neutrinos produced in air showers on the opposite sides of the Earth. These atmospheric neutrinos are the predominant background for astrophysical neutrinos in regions where atmospheric muons are absorbed by the Earth.

#### 1.3.2.1 Atmospheric Neutrinos

Conventional atmospheric neutrinos are produced by the decay of muons, pions and kaons. Since the Earth's atmosphere is much more dense than typical astrophysical media, air shower products are more likely to interact before decaying. This affect is energy-dependent; particles below a threshold energy will likely decay before having a chance to interact, and the decay products will have roughly the same spectrum as the incident cosmic rays ( $\sim E^{-2.7}$ ). Above this threshold (115 GeV for  $\pi^\pm$ ), the particle will most likely interact, losing energy in the process. The spectrum of these particles is typically  $\sim E^{-3.7}$ . Because the threshold for muon detection in IceCube is roughly 1 TeV, this is the spectrum of atmospheric muon measured. Prompt atmospheric fluxes from the decay of relatively heavy, charmed mesons have not been measured, but are expected to follow the CR spectrum.

These atmospheric neutrinos make up an irreducible background for Northern Hemisphere neutrino point-source searches. The rate is mostly flat (see Chapter 6), with roughly  $\pm 5\%$  annual fluctuations due to the change in the density of the upper atmosphere as a result of temperature fluctuations averaged over the Northern Hemisphere.

## 1.4 Neutrino Oscillations

The neutrino has a peculiar property which allows it to change flavor, which has been observed in a deficit of anti-electron neutrinos from the Sun [19]. Neutrino oscillation has also been observed using atmospheric neutrinos [20, 21, 22]. There are three neutrino mass eigenstates, which do not directly map onto the three flavor eigenstates. As a neutrino propagates, this difference in mass eigenstates leads to an interference between the flavor eigenstates. These oscillations induce changes in flavor as a neutrino propagates, with different probabilities of interacting as a given flavor for different baselines. The relationship between the flavor and mass eigenstates is

$$|\nu_\alpha\rangle = \sum_i U_{\alpha i}^* |\nu_i\rangle, \quad (1.14)$$

where  $|\nu_\alpha\rangle$  is a specific flavor state,  $\alpha = e$  (electron),  $\mu$  (muon), or  $\tau$  (tau), and

$$|\nu_i\rangle = \sum_\alpha U_{i\alpha} |\nu_\alpha\rangle, \quad (1.15)$$

where  $|\nu_i\rangle$  is a specific mass state,  $i = 1, 2, 3$ . The terms  $U_{\alpha i}$  map to elements of the Maki-Nakagawa-Sakata (MNS) matrix [23]. The MNS matrix is given by:

$$U = \begin{pmatrix} c_{12}c_{13} & s_{12}c_{13} & s_{13}e^{-i\delta} \\ -s_{12}c_{23} - c_{12}s_{23}s_{13}e^{i\delta} & c_{12}c_{23} - s_{12}s_{23}s_{13}e^{i\delta} & s_{23}c_{13} \\ s_{12}s_{23} - c_{12}c_{23}s_{13}e^{i\delta} & -c_{12}s_{23} - s_{12}c_{23}s_{13}e^{i\delta} & c_{23}c_{13} \end{pmatrix} \begin{pmatrix} e^{i\alpha_1/2} & 0 & 0 \\ 0 & e^{i\alpha_2/2} & 0 \\ 0 & 0 & 1 \end{pmatrix}, \quad (1.16)$$

where  $c_{ij} = \cos \theta_{ij}$  and  $s_{ij} = \sin \theta_{ij}$ , with  $\theta_{ij}$  referred as the mixing angle between two mass eigenstates. In the case that neutrinos violate CP symmetry,  $\delta$  is non-zero. The phases  $\alpha_1$  and  $\alpha_2$  cover a potential difference between neutrinos and anti-neutrinos, both being zero unless the neutrino is a Majorana particle, such that it is its own antiparticle.

We can write the probability of a neutrino converting from a flavor  $\beta$  to a flavor  $\alpha$  as  $|\langle \nu_\beta | \nu_\alpha \rangle|^2$ . This expands to:

$$\begin{aligned}
 P_{\alpha \rightarrow \beta} &= |\langle \nu_\beta | \nu_\alpha \rangle|^2 \\
 &= \left| \sum_i U_{\alpha i}^* U_{\beta i} e^{-im_i^2 L/2E} \right|^2 \\
 &= \delta_{\alpha\beta} - 4 \sum_{i>j} \text{Re}(U_{\alpha i}^* U_{\beta i} U_{\alpha j} U_{\beta j}^*) \sin^2\left(\frac{\Delta m_{ij}^2 L}{4E}\right) \\
 &\quad + 2 \sum_{i>j} \text{Im}(U_{\alpha i}^* U_{\beta i} U_{\alpha j} U_{\beta j}^*) \sin\left(\frac{\Delta m_{ij}^2 L}{2E}\right), \tag{1.17}
 \end{aligned}$$

where  $\Delta m_{ij}^2$  is the difference between the squares of the two mass eigenstates  $m_i^2 - m_j^2$ ,  $L$  is the distance traveled, and  $\delta_{\alpha\beta}$  is the Kronecker delta. The total magnitude of oscillations can be determined from the elements of the MNS matrix, the frequency of oscillation can be expressed (putting back in terms of  $\hbar$  and  $c$  to go from natural to metric units) as:

$$\frac{\Delta m_{ij}^2 L}{4E} \approx 1.27 \Delta m_{ij}^2 (\text{eV}^2) \frac{L(\text{km})}{E(\text{GeV})}. \tag{1.18}$$

A review of neutrino oscillation physics can be found in [24].

The experimental limits have been produced in the analyses presented here assuming a flux of only muon neutrinos. The scenario using the standard neutrino oscillation parameters has MNS matrix elements  $|U_{e3}|^2 \ll 1$  and  $|U_{\mu i}| \simeq |U_{\tau i}|$  for each mass state  $i$ . Using a baseline of astronomical distances ( $L \rightarrow \infty$ ) ensures that neutrino oscillations occur at all energies; this scenario results in a source producing neutrinos via pion decay with a ratio of

$\nu_e : \nu_\mu : \nu_\tau = 1 : 2 : 0$  resulting in a flavor ratio at Earth of  $1 : 1 : 1$  [25]. It is also possible that there is a contribution at very high energies to the flavor ratio of tau neutrinos due to the decay of charmed mesons [26].

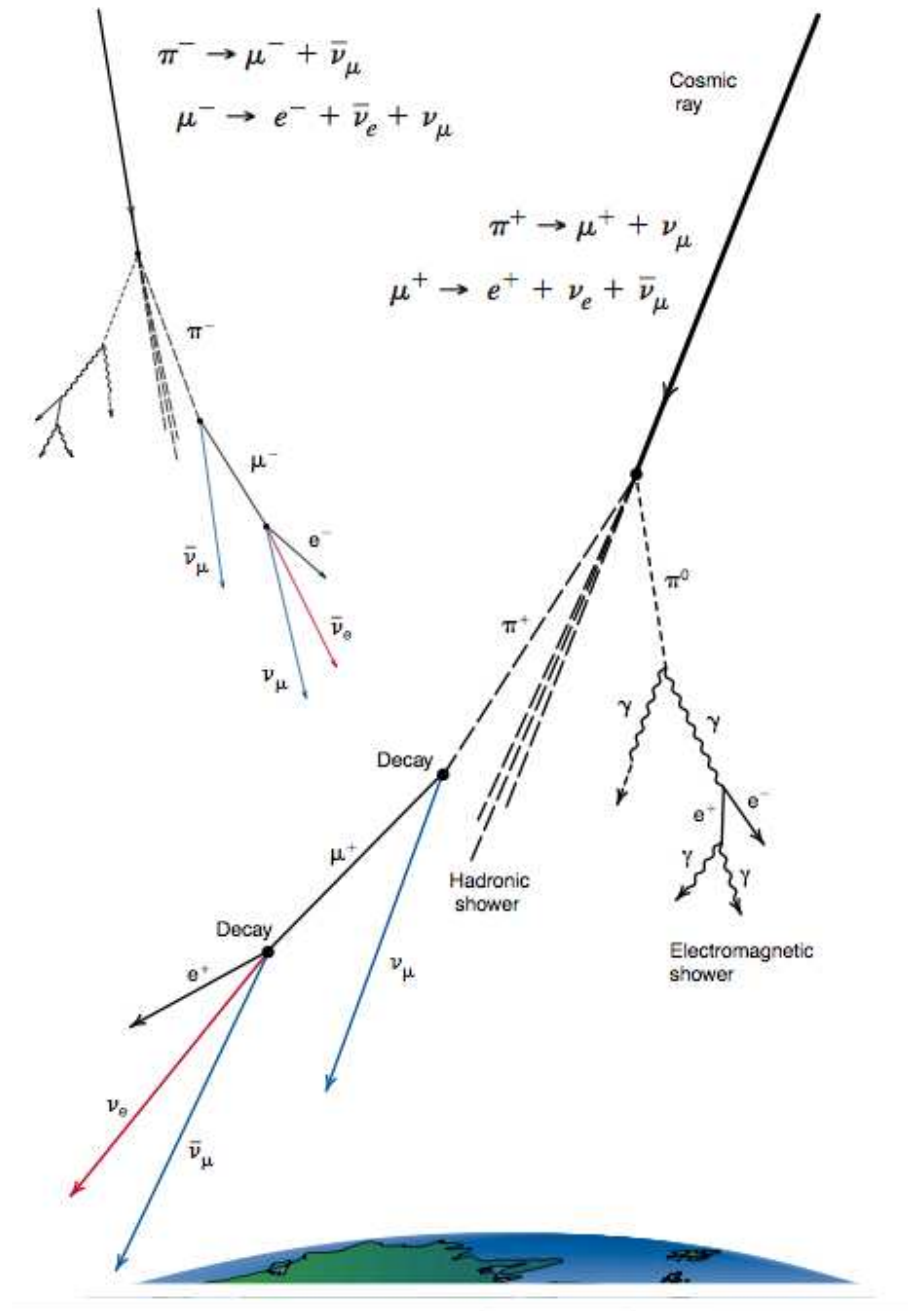


Figure 1.4 Cosmic rays produce extensive air showers upon collision with particles in the upper atmosphere, shown here. Muons and neutrinos are penetrating particles which can reach the IceCube detector through the overburden of ice or through the bulk of the Earth, respectively.

## Chapter 2

### Candidate Sources of Flaring Neutrino Emission

This chapter describes candidate classes of sources for high energy neutrino production. Neutrinos are interesting as messenger particles as their low cross sections allow them to escape regions where photons and charged particles would be absorbed or deflected. Neutrinos offer a new way of examining the universe which would otherwise be inaccessible.

Sources described in this chapter are interesting candidates for high energy neutrino production due to their non-thermal photon spectra. Thermal spectra exhibit an exponential cutoff at high energies: even objects with temperatures of millions of Kelvin typically fade out in the keV, far before the TeV particles of interest to IceCube. Non-thermal spectra could indicate particle acceleration in the shocks created in supernovae explosions and in jets of matter created in dynamic regions in the center of galaxies. These spectra are hints that these non-thermal sources could be capable of accelerating particles to extremely high energies which are seen in the cosmic ray spectrum. The most likely mechanism for this particle acceleration was proposed by Fermi and is covered in Section 1.3.1. Currently no source of neutrinos of  $\gtrsim 100$  GeV energy has been identified with significance above a  $5\sigma$  threshold [27, 28, 29]. The Sun [30, 31] and supernova 1987a have been identified as sources of MeV energy neutrinos, however. SN1987a was detected in three detectors:

Kamiokande II (11 neutrinos [32]), IMB (8 neutrinos [33]), and Baksan (5 neutrinos, [34]).

Classes of Galactic and extra-galactic astronomical sources exhibit time-dependent emission that range from short bursts of the order of seconds and minutes from Gamma-Ray Bursts (GRBs) or Soft Gamma Repeaters (SGRs) up to longer flares from Active Galactic Nuclei (AGN) which last hours to weeks. Sources thought to be steady are also included here because surprises are expected. For example, the Crab Nebula supernova remnant, used as a 'standard candle' for TeV photon emission, exhibited two large flares observed in GeV photons in 2010-11 [35].

## 2.1 Extra-Galactic Source Candidates

The cosmic ray spectrum extends to energies well above that of particles which can be contained in the Milky Way. The two main classes of extra-galactic objects thought to be powerful enough to accelerate particles above EeV energies are active galactic nuclei and gamma-ray bursts.

### 2.1.1 Active Galactic Nuclei

The first known AGN, now classified as 3C 273, was known to not be a star because it did not have typical absorption features and had very strong radio emission. It was theorized and shown to be a distant galaxy with a bright core region [36]. AGN are powered by super-massive ( $\gtrsim 10^6$  solar mass) black holes. Matter is collected in an accretion disk around the black hole, which heats up as due to friction and radiates in optical wavelengths. The hot rotating gas results in a magnetic field perpendicular to the disk. It is thought that this field results in two collimated relativistic jets of matter which are expelled from the active center of the galaxy [37]. Blobs of matter are occasionally emitted from the central region down

the jets, which emit brightly (see Figure 2.1) and are expected to be shock environments for particle acceleration. Now hundreds of AGN are known [38, 39], and their observed emission features are mainly determined by the angle between the relativistic jet with the Earth (see also Figure 2.2). Other classification features are the strength of the object in radio bands, and the overall luminosity.

Faranoff Riley (FR) galaxies are observed from the side, such that the jet and inner torus is visible. These galaxies are split into low and high overall luminosity branches (FR-I and FR-II, respectively). Seyfert Galaxies are also oblique like FR galaxies, but are radio quiet and exhibit strong absorption lines.

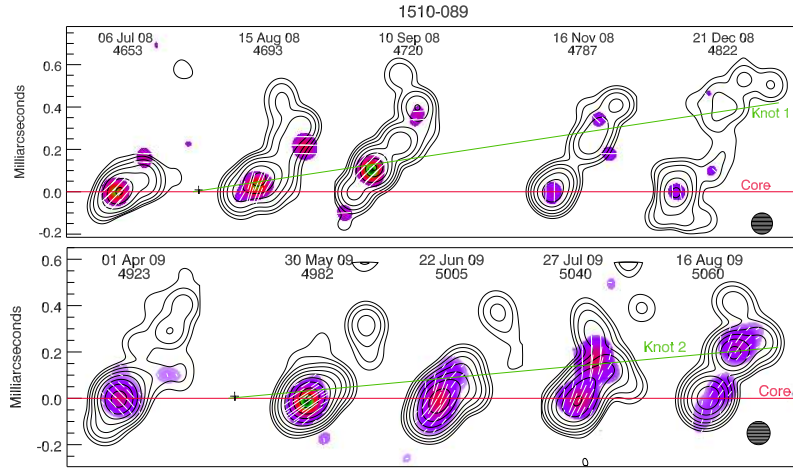


Figure 2.1 The motion of ejected blobs of material from the blazar PKS 1510-089 seen with 43 GHz radio images. The images are convolved with a circular Gaussian beam of the shaded circle at the lower right. Dates are given by calendar and with TJD (JD-2450000). The color shows the polarization intensity. Figure from [40].

For active galaxies with one of the jets pointing directly at the Earth, their observed emission features are nearly all due to the beamed emission of the relativistic particles form-



ing the jet. These are classified as BL Lac type objects (radio loud, low luminosity) or Flat Spectrum Radio Quasars (FSRQs, which are radio loud with high overall luminosity). These are the most interesting for neutrino astronomy, since nuclear decay products from the jet will also be beamed in the direction of the Earth. These objects also exhibit strong and fast variability due to the small emission region compared to the rest of the galaxy. The AGN tested for flaring behavior in Chapter 10 are exclusively BL Lacs or FSRQs, commonly unified in the AGN class of blazars.

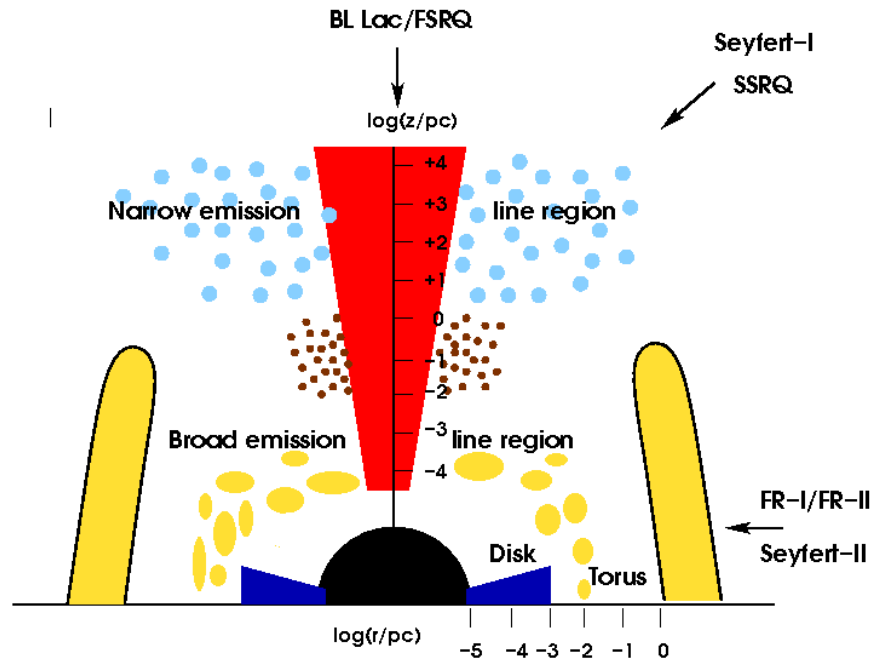


Figure 2.2 Schematic of a cylindrically-symmetrical center of an AGN. Axes are logarithmic in units of parsec. Regions of the AGN are marked. The classifications of AGN are marked off by arrows approximating the viewing angle of the observer. Figure from [6].

The emission from blazars is known to be variable at all wavelengths. Simultaneous multi-wavelength (MWL) observations are crucial for understanding the cause of this variability [41, 42, 43, 44, 45]. The intensity of these objects can vary by more than an order of

magnitude between different observing epochs. The typical time scales of AGN flares vary from hours to days, though high-energy variability has been observed on much shorter time scales, in some cases even down to just a few minutes [46, 47].

The spectral energy distributions (SEDs) of blazars extend orders of magnitude across the electromagnetic spectrum and are characterized by structures of low and high energy non-thermal peaks (see Figure 2.3). The low energy component in the radio to soft x-rays is due to synchrotron radiation of electrons gyrating in a magnetic field. The high energy component (x-ray to gamma ray) currently has two main models: leptonic and hadronic.

The most prominent candidate model for the SED structure of blazars explains the emission using only relativistic electrons (and positrons). Synchrotron radiation accounts for the lower-energy emission hump. These synchrotron photons are up-scattered via the inverse Compton effect on the same population of electrons, establishing the Synchrotron Self Compton (SSC) model for blazar emission. The intensity and peak of the second emission hump are controlled by the energy and density of the electron population, and fluctuations in emission from both peaks will be correlated. Hadronic models explain the observed high energy photon emission component as a result of a population of relativistic protons accelerated in the emitted blobs, which will undergo  $pp$  and  $p\gamma$  interactions and produce pions. Neutral pions decay to gamma rays up to TeV energies, forming the high energy peak. Charged pions will also be produced, which will produce TeV neutrinos upon decay, such that the detection of neutrinos would be unambiguous evidence of hadronic acceleration. Proton synchrotron emission can also contribute to the high-energy component if they are accelerated to very high energies (reviews on models can be found in [48, 49, 50] and references therein).

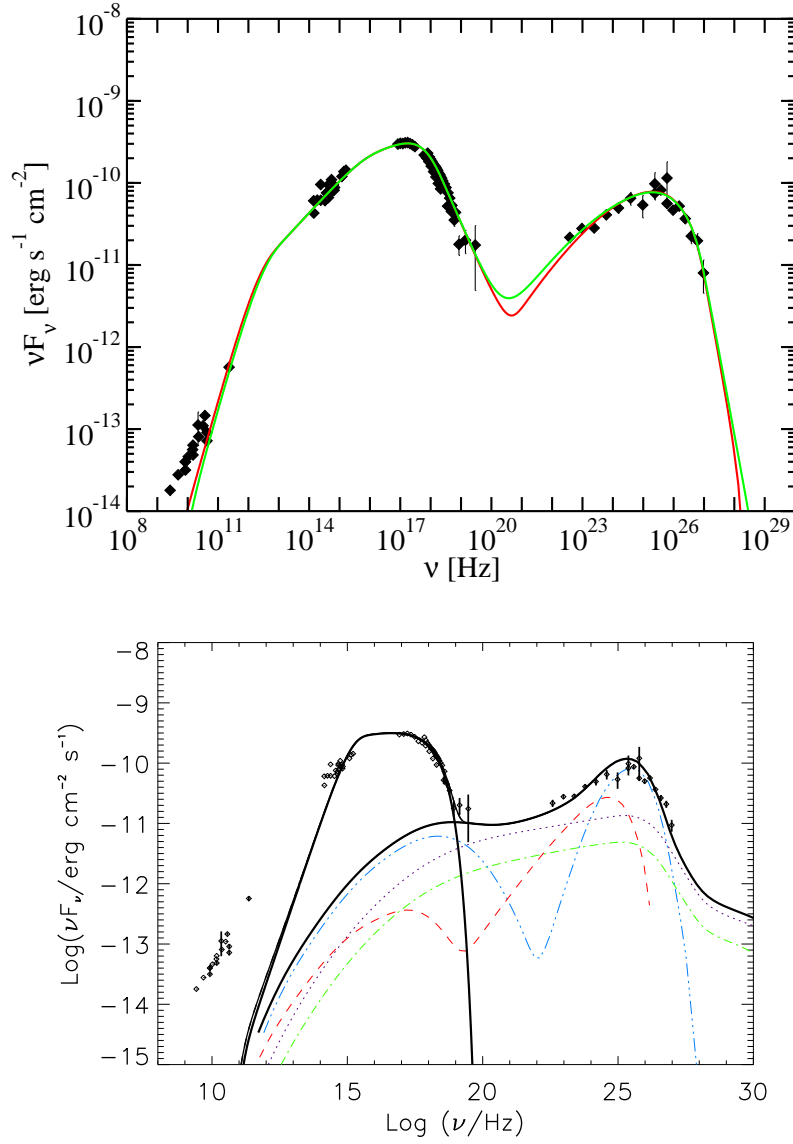


Figure 2.3 Leptonic model (top) and Hadronic model (bottom) fits to the spectral energy distribution of the blazar Markarian 421. In the hadronic model, the black dotted line is the contribution of  $\pi^0$  cascades, the green dash-dotted line is for  $\pi^\pm$  cascades, the blue dash-triple-dotted line is  $\mu$  synchrotron and cascade, and the red-dashed line is for proton synchrotron and cascade emission. The sum of all components (including the synchrotron emission of electrons forming the low bump) is the solid black line. The leptonic model uses two minimum variability timescales to determine the size of the emission region: 1 day for the red curve, 1 hour for the green. Figures from [51].

Perhaps the most compelling evidence of hadronic models are observations of “orphan” flares, defined as TeV photon emission without accompanying x-rays, such as the 1ES 1959+650 flare in 2002 [52]. An a posteriori observation with AMANDA-II of two events [53], one exactly during the flare and another 31 days later, triggered some theoretical calculations [54, 55]. A previous stacking search for neutrinos from AGNs used AMANDA data [56]. Two recent flares included in the MWL triggered searches (see Sections 10.1 and 10.2, also [57, 58, 59, 60]) are suspected to be orphan flares, but x-ray observations were not simultaneous with gamma-ray observations and there is a possibility of having missed the x-ray flare.

### 2.1.2 Gamma-Ray Bursts

Gamma-Ray Bursts are believed to be produced by the most powerful phenomena in the universe [61, 62]. They are also interesting as time-dependent candidate neutrino sources [63, 64]. IceCube conducts dedicated searches using satellite information for these objects [65, 66, 67]. Untriggered searches are also sensitive to this source class if two or more neutrinos can be detected from the same GRB. While the dedicated searches are in general much more sensitive due to the timing and directional information from GRBs observed in gamma rays or x-rays, the untriggered search performed here has the potential to detect a burst which was not observed in photons (due to e.g. absorption or lack of monitoring).

Presently the best candidate model for high-energy emission from GRBs is the fireball model. The prompt gamma rays are made in expanding shocks in plasma ejected in a relativistic, highly beamed ( $\Gamma = 100 - 1000$ ) jet. These jets may be produced by the merger of neutron stars or by the formation of a black hole, and may also accelerate hadrons to TeV energies leading to the production of neutrinos. GRBs are seen to have a bimodal distribu-

tion of the durations of high-energy emission, GRBs less than two seconds are thought to be due to neutron star mergers, while those longer than two seconds are thought to be due to black hole formation in supernova explosions.

The dedicated searches from IceCube using a combined sample from the 40 and 59-string detectors presently sets strict limits on models of neutrino emission from GRBs. A sample of 300 GRBs from the Northern and Southern Hemispheres was tested, and no events were found. The limit from this result is 5% with respect to GRB models using the hypothesis that all cosmic rays  $\gtrsim 3$  PeV are extra-galactic and created in GRBs [68]. This suggests that other objects are the sources of cosmic rays, or that the parameters entering the model need to be rethought.

## 2.2 Galactic Source Candidates

Source candidates in the Milky Way are thought to dominate the cosmic ray spectrum up to the knee at 3 PeV. The estimated number of supernovae in the Milky Way is about 3 per century, and the observed flux over the cosmic ray spectrum up to the knee corresponds to roughly 10% of the energy from the shock front of material released in these massive explosions. Above 3 PeV, objects outside of the galaxy are thought to be the sources, as cosmic rays with this much energy will not be confined to the galaxy.

### 2.2.1 Supernova Remnants

As a star ages, it gradually begins to fuse successively more massive nuclei in its core, until it reaches iron, at which point fusion becomes an endothermic reaction. Hot material which does not contribute to the energy budget of the star accumulates in the core while fusion continues in shells outside the core, where electron fermion degeneracy sustains the

core against the pressure of outer layers. As the mass of the degenerate core or a white dwarf increases, the radius decreases until the mass approaches the value of 1.44 solar masses when the theoretical radius of the object approaches zero [69, 70]. Before that happens, it becomes energetically favorable for the protons in the star to capture electrons, forming neutrons. This releases much of the gravitational energy of the dwarf or stellar core in a shower of electron neutrinos in what is classified as a supernova. The compact remnant depends on the mass of the original star, and can be either a black hole or a neutron star. Neutron star remnants are roughly 10 km in size, exhibit strong magnetic fields ( $10^{12}$  G) and a rotational period of as low as milliseconds. Neutron stars also exhibit a narrow, bright beam of electromagnetic radiation which can be seen if it crosses the observer's line of sight. Black holes are so compact they are hidden behind a shroud where their escape velocity is equal to the speed of light.

When a star explodes in a supernova, much of its material is ejected in a spherical shell with typical radial velocities of  $10^5$  m/s. As the shell expands, it will push out into the thin material of the interstellar medium, forming a shock front. This environment will energize particles via Fermi acceleration (see Section 1.3.1). These objects show hard energy spectra with a cutoff for gamma rays at a few TeV, but for some the cutoff is slightly above 10 TeV [71].

Supernova remnants (SNRs) can be broken up into two broad categories. The first class, pulsar wind nebulae (PWN), have rapidly rotating neutron stars at their center which is the source of a quickly changing magnetic field that accelerates particles. This effect generates an additional particle wind from the central object. The second class of SNR are those which are shell-like. PWN include the Crab nebula and Geminga while shell-

like SNR include Cassiopeia A. Recently the Crab pulsar has been seen to emit pulsed photons of  $> 100$  GeV energy by VERITAS [72], so the central region of a PWN can be very energetic. SNRs evolve as they spread, at first the shell is dominated by the matter initially ejected from the star, gradually accumulating matter until the shell is mainly swept-up gas. Models beyond simple diffusive shock acceleration using non-linear instabilities in the shock can also be used to trap particles and accelerate them to higher energies before they escape [73].

### 2.2.2 Soft Gamma-Ray Repeaters

SGRs are x-ray pulsars that show variability at different timescales and a persistent x-ray emission with luminosity  $L \sim 10^{35}$  erg/s with short bursts of x-rays and gamma rays with  $L \sim 10^{41}$  erg/s lasting  $\sim 0.1 - 1$  s (for review see [74]). These x-ray pulsars, together with anomalous x-ray pulsars, are considered to be the best candidates for magnetars, which are isolated neutron stars powered by huge magnetic fields ( $B \sim 10^{15}$  G). At times these sources emit giant flares with initial spikes of hard non-thermal radiation up to luminosities of  $\sim 10^{46}$  erg/s lasting some seconds. Smaller bursts from these objects are thought to be caused by episodes of magnetic reconnection and ‘glitches’ where the neutron star has a sudden change in the rotational period [74], but it is not clear if the largest flares are caused by these mechanisms or something else. These flares may also accelerate baryons and produce neutrinos [75, 76, 77]. Limits for photons in the 10 TeV-100 PeV energy range using AMANDA-II data were published from the powerful giant flare observed in Dec. 2004 from SGR 1806-20 [78]. In the catalogue used in one of our triggered flare searches (Section 10.2), we have a period of intense flares from SGR 0501+4516 discovered by SWIFT on Aug. 22, 2008, and observed also by RXTE/ASM, Konus-Wind and the Fermi

GBM [79].

### 2.2.3 Microquasars and Binary Objects

When two stars of unequal masses are in a binary system, they will evolve through the main sequence at different rates [80], one expiring before the other. If the more massive star is large enough to explode in a supernova, the stellar remnant, a neutron star or black hole, will remain and stay gravitationally bound with its companion star. X-ray binaries are systems with a companion star and a stellar-mass compact object. There are two classes of binary systems: high mass x-ray binaries (HMXB), where the companion star is a large O/B star; and low mass x-ray binaries (LMXB), where the companion is only a few solar masses. When the companion star overfills the Roche lobe of the system, the overflow falls into the gravitational well of the compact object, forming an accretion disk. In the disk, the material accelerates and heats up due to friction closer to the last stable orbit.

Microquasars are special cases of x-ray binaries, where photon emission is visible from two jets from the compact object, similar to AGN but for the scale (see Figure 2.4). X-ray, and in some cases gamma ray emission, are observable from the central part of the system. Optical to radio emissions are observable from farther out along the jet. These systems are variable; some, such as Cygnus X-1 and Cygnus X-3, exhibit occasional bursts of activity on timescales of days, possibly producing neutrinos from 1-100 TeV [81]. Others, such as LS I +61 303, have highly elliptical orbits and are seen to emit TeV photons during the part of the orbit when the binary objects are farthest (apastron) [82].

In the case of LS I +61 303, the stellar partner is a massive, rapidly rotating B0Ve main sequence star. The star loses mass through a strong stellar wind thought to be formed by a fast, low-density polar wind and a slow, high-density equatorial decretion disk [84].



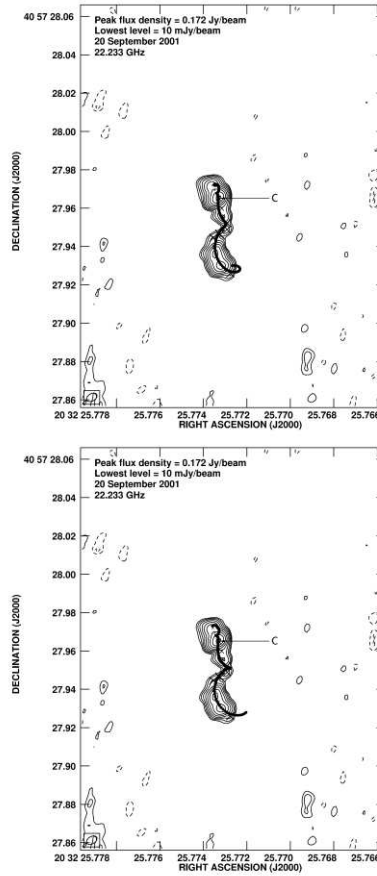


Figure 2.4 Figure of Cygnus X-3 during a radio outburst on September 20, 2001 taken in 22-GHz waveband with the Very Long Baseline Array, where jet emission is clearly visible. The black lines on the top and bottom images are model fits for the motion of knots along the ejected jet of material. Image from [83].

The dynamic binary system of LS I +61 303 has been observed to be periodic in a broad range of wavelengths from radio [85], soft and hard x-ray [86, 87], GeV [88], and TeV photons [89, 90]. It remains open if the TeV photon emission stems from a microquasar scenario [91] or a pulsar scenario [92]. At present, observations of the system cannot rule out the presence of hadrons in the pulsar wind, but the detection of TeV neutrinos would be

positive proof of hadronic acceleration.

## 2.3 Acceleration potential of sources

Charged particles can be accelerated in the shock fronts of SNR or AGN. Rotating neutron stars can also have tremendous time-dependent magnetic fields with the potential to accelerate particles. However, a given source will have a maximum energy to which it can accelerate particles depending on the strength of the magnetic field and the size of the region permeated by the field.

A charged particle will no longer be confined to a region with a magnetic field when the Larmor radius is greater than the size of the region, which sets an upper limit on the energy of particles that can be produced. The Larmor radius of a particle with momentum  $\vec{p}$  in a magnetic field with perpendicular component  $B_{\perp}$  is expressed as:

$$R = \frac{|\vec{p}|}{qB_{\perp}} = \frac{E/c}{ZeB_{\perp}}. \quad (2.1)$$

The equation for the maximum particle energy is then:

$$\frac{E_{\max}}{\text{GeV}} \simeq 3 \times 10^{-2} \times Z \times \frac{R}{\text{km}} \times \frac{B}{\text{G}} \quad (2.2)$$

The maximum energy is proportional to the charge of the particle  $Z$ , the size of the region and the strength of the magnetic field, leading to a plot showing the candidate accelerators for the highest energies of the cosmic ray spectrum (see Figure 2.5).

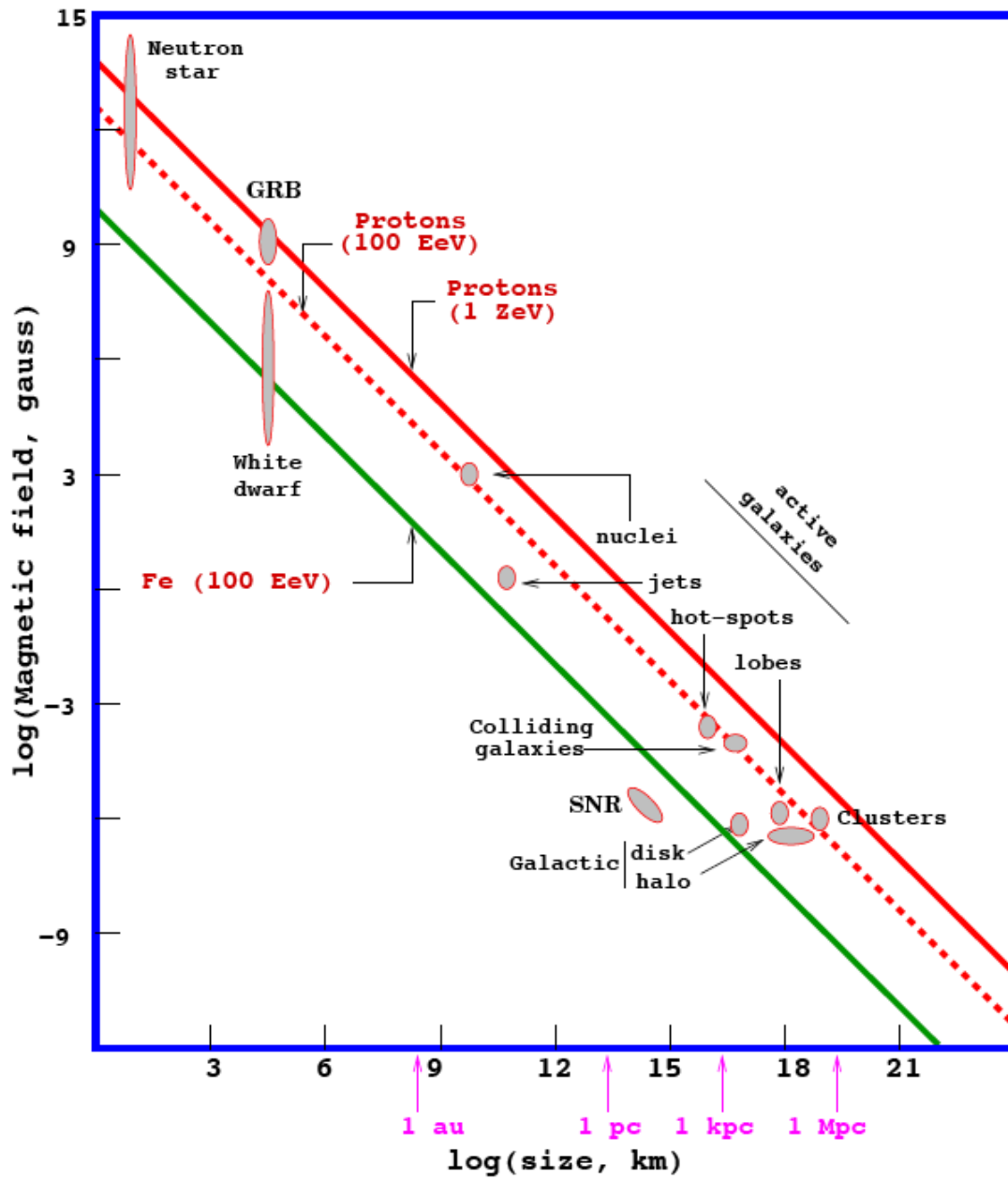


Figure 2.5 The Hillas plot of the distribution of source sizes and magnetic field strengths required to accelerate cosmic rays to specific energies for protons and iron, here marked off using the diagonal lines to indicate the minimum size and magnetic field strength. Classes of astronomical objects which may be accelerators are marked. Plot from [93].

## Chapter 3

### Multi-Wavelength Observations

Observations of sources in photons is essential for their characterization, because the processes which accelerate particles to relativistic energies will also exhibit emission of high-energy photons with a characteristic spectrum. A number of sources have been observed to emit photons of  $> 1$  TeV in energy, which makes them of particular interest to IceCube. This section covers the nature of the multi-wavelength observations used to motivate IceCube searches and touches on the different emission models that can be differentiated by observations in photon energy bands.

As an example, the blazar Markarian 421 is an object with frequent flares in multiple energy bands, and has been frequently the subject of multiwavelength campaigns from radio to TeV energy photons. The nature of outbursts from Markarian 421 is not clear; some flares see the x-ray wavebands tracking the same as gamma rays, while others see activity in only one or the other [94, 44], potentially pointing to different underlying causes of different outbursts.

The correlation of high energy emission from blazars is important in the effort to model the emission mechanism of objects such as Markarian 421 and other blazars. The main mechanisms use either a leptonic model where a single population of relativistic elec-

trons is responsible for the synchrotron emission and also the high energy radiation as being due to the inverse Compton effect, or a hadronic model where the high energy emission is due to a separate population of relativistic protons (see Figures 2.3 and 3.1). Presently both models have enough freedom to fit the measured spectral energy distributions. Multi-wavelength observations are useful for directing neutrino searches, and as more is known about blazars and other objects, neutrino searches will be able to be directed to specific kinds of flares which are most likely to be associated with cosmic ray acceleration and neutrino production.

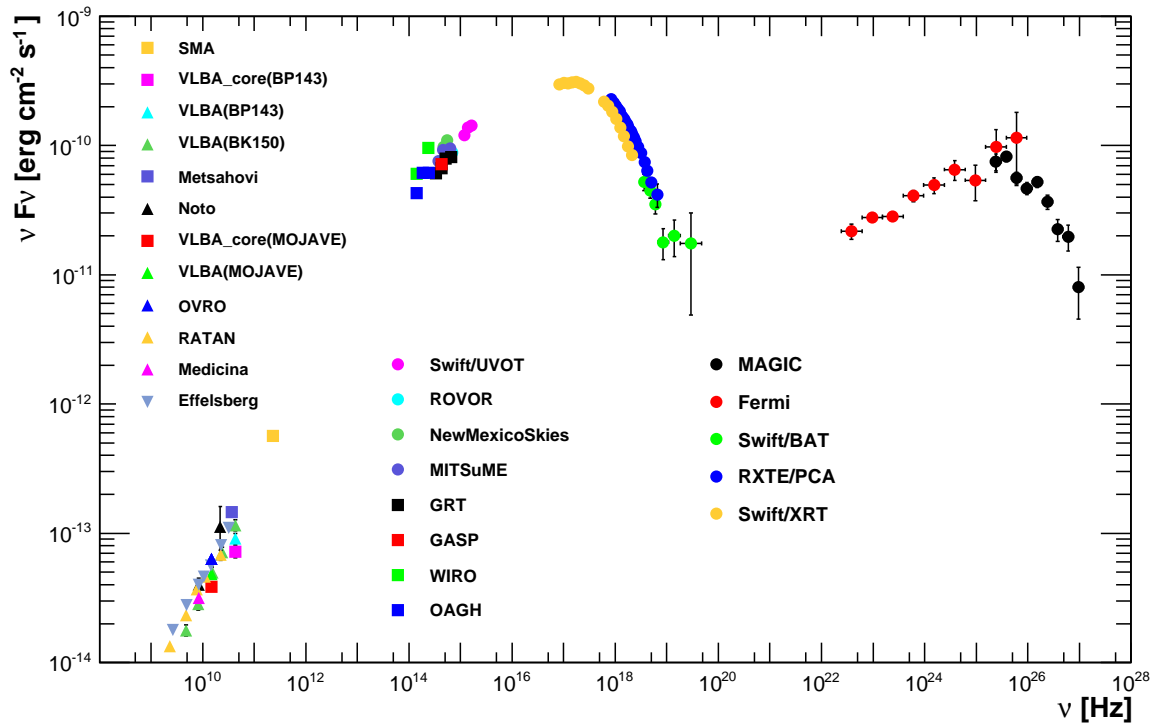


Figure 3.1 Spectral energy measurements for the blazar Markarian 421, showing the low-energy hump in  $10^9$  to  $10^{20}$  Hz, and the high-energy hump from  $10^{20}$  to  $10^{28}$  Hz, including data taken from radio, infrared, optical, ultraviolet, x-ray and gamma-ray observatories. Figure from [51].

One particularly interesting flare signature is called an *orphan flare*, where a blazar exhibits a heightening in the TeV photon band, but not in other energy ranges. This type of flare was seen twice from 1ES 1959+650, and is not currently explainable by leptonic emission models. There was an *a posteriori* check using AMANDA neutrino data during these orphan flares, which saw two on-source events during these peculiar flares, roughly a  $3\text{-}\sigma$  result [53].

Other objects, such as microquasars, are also highly dynamic in x-ray and gamma-ray bands, the light curves of which are typically more complicated than for AGNs. The variability can depend on the orbital parameters of the system and the amount of material surrounding the compact object, which can vary more than in the case of blazars, accreting and occasionally being blown off in a large burst. This information has also been used elsewhere [95] to guide other searches for neutrino emission from the binary system Cygnus X-3 during outbursts.

### 3.1 Optical Monitoring of Blazars

Part of the work done in this IceCube analysis was to contribute to a multiwavelength campaign monitoring blazars known to exhibit rapid changes in flux across many wavebands (see Table 3.1 for a list of sources). This was done to complement the observations in high-energy photons used in the likelihood analysis. The results for the blazar Markarian 421 from this campaign with other multiwavelength contributions can be found in [44] and [94]. The instrument used is the WIYN 0.9 meter optical telescope located at the National Optical Astronomy Observatory at Kitt Peak, Arizona.

Since 2006 we have used it in a synoptic program for multiwavelength monitoring of a number of blazars using the Johnson B and V and Cousins R optical filters and a single-chip

CCD with a 20 arcmin field of view. The images are reduced using the IRAF data package [96, 97]. Bias images and dome flat-field images taken on each night are used to subtract backgrounds due to the CCD camera and the telescope optics using the `ccdproc` routine. Photometry is done differentially using the `qphot` routine using a minimum of three known reference stars per object [98]. The fluxes are not corrected to account for the emission of the host galaxy, because in the IceCube analysis, we are more interested in measuring the relative variation in flux over time from each source. Examples of the light curves produced as a result of this program, including that for Markarian 421 which has been observed since 2006, can be seen in Figure 3.2.

Source	Dates
Markarian 421	2006-2011
1ES 1959+650	2006-2011
BL Lacertae	2010-2011
1ES 2344+514	2008-2010
3C 66A	2009-2011
H 1426+428	2009-2011
W Comae	2009-2011
3C 273	2010-2011
1ES 1218+304	2007
1ES 0806+525	2008-2011
CGRaBS J0211+1051	2011

Table 3.1 List of the sources covered by the WIYN synoptic program and dates when data was collected.

## 3.2 High Energy Photon Observatories

The multiwavelength observations also involve several observatories designed to detect much higher energies. For photons of x-rays and GeV gamma rays, the Earth's atmosphere is opaque and satellite-based telescopes are required. At photon energies above

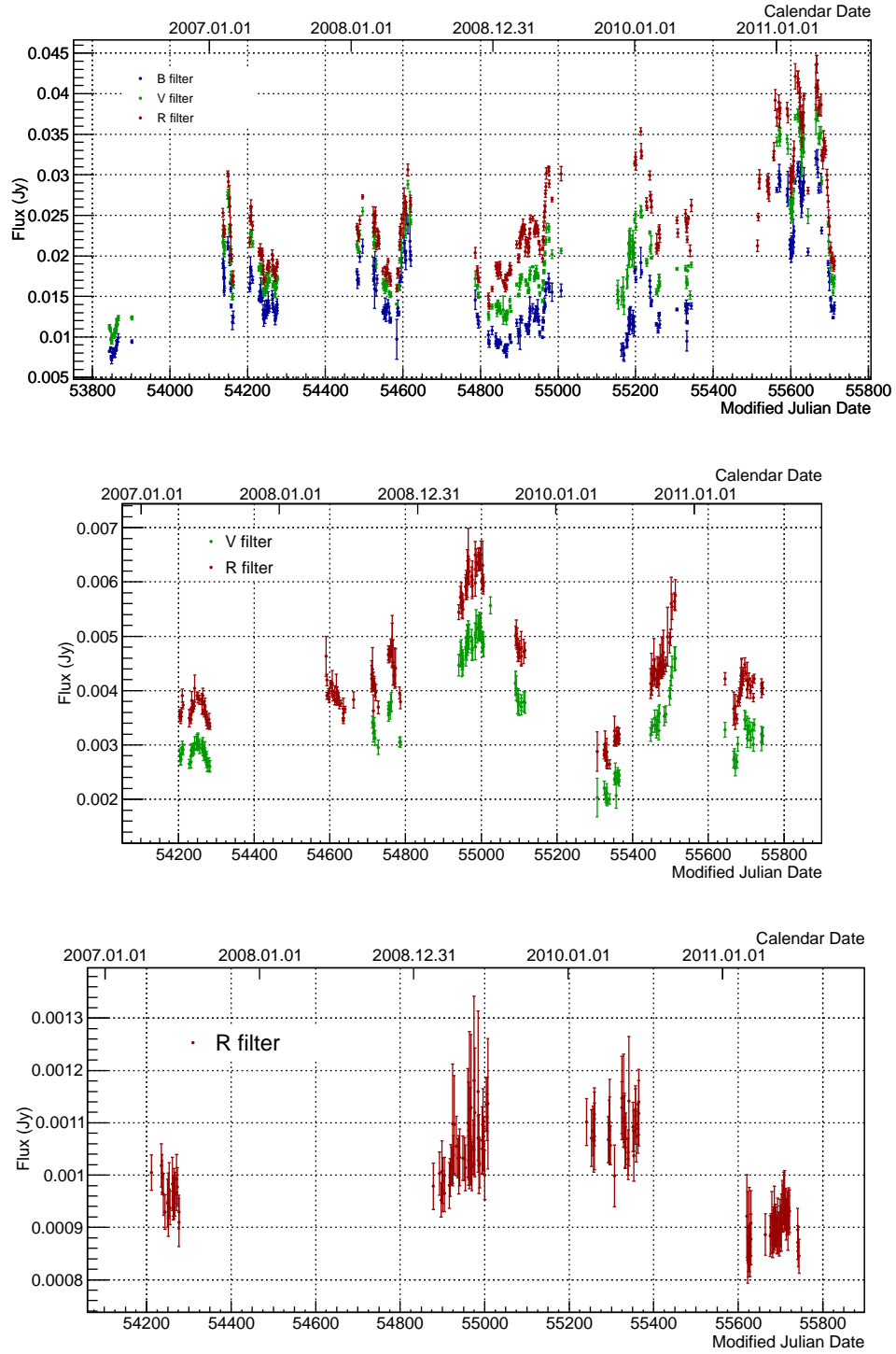


Figure 3.2 Three of the optical light curves from the WIYN synoptic program. Top is Markarian 421, middle is 1ES 1959+650, bottom is H1426+428.



roughly 1 TeV, showers from the interaction of these photons in the upper atmosphere can be detected from ground-based instruments, typically situated at high elevation. This section covers the observatories which took data used in IceCube searches.

### 3.2.1 Swift Gamma-Ray Burst Mission

The *Swift* satellite was launched on November 20, 2004 with multiple instruments to detect and study GRBs, in order to both detect the initial burst and to study the afterglow after slewing to the burst coordinates [99]. The Burst Alert Telescope (BAT) is designed to cover a 3 str piece of the sky, with a randomly distributed coded mask of lead tiles. The angular response of the BAT has a FWHM of 20 arcmin. The BAT energy range is 15-150 keV, and light curves are provided in the 15-50 keV range. Swift also has pointed instruments for ultraviolet and optical measurements (the UVOT) and the X-Ray Telescope (XRT) to take images and spectra of GRB afterglows.

### 3.2.2 Fermi Gamma-Ray Space Telescope

The *Fermi* satellite was launched on June 11, 2008. It has two primary instruments: the Large Area Telescope, or LAT [100], and the Gamma-Ray Burst Monitor, or GBM, which is designed to detect GRBs over a 9.5 str field of view [101].

The LAT is a pair-production telescope with a 2.4 str field of view. It operates in a continuous scanning mode, so it is able to scan the entire sky every two orbits, or about 3 hours, and for any object it samples the light curve several times per day. The main component is a 4x4 array of silicon-strip pair tracker with tungsten conversion foils and a Cesium Iodide calorimeter for energy measurement. The tracker and calorimeter are covered by a plastic scintillator anti-coincidence detector to veto tracks due to the much larger numbers

of cosmic rays. The angular resolution is strongly energy dependent; the angle between the true direction and reconstructed direction is less than  $3^\circ$  for 68% of events at 100 MeV to less than  $0.04^\circ$  for 68% of events at 100 GeV. Energy resolution of the LAT is typically better than 10% for the nominal energy range of 100 MeV to 300 GeV.

After 11 months of operation, the Fermi-LAT collaboration published their first AGN catalogue [102] containing 709 GeV-sources associated with AGNs, many of which are in the previously published Bright Source list catalogue [103]. The Fermi-LAT collaboration has studied the fluctuations of a sample of blazars using the first 11 months of data [104], featuring many of the sources tested with IceCube for coincident gamma and neutrino emission. Of the 132 sources which are seen with very high confidence by the LAT, 57 are FSRQs and 42 are identified as BL Lac objects [105], which can be seen in Figure 3.3.

The LAT photon-by-photon data, exposure maps, and a set of analysis tools are provided to the public, and the light curves in this work are produced using these data and tools. Cosmic-ray induced events are also included; light curves here use the diffuse class event selection used for events which have a high probability of being photons. For each source the *Fermi* Science Tools v9r15p2 package is used. Photons are selected using the `gtselect` tool from within  $2^\circ$  of each source. Photon events with zenith angles greater than  $105^\circ$  were excluded to avoid contamination due to the Earth's albedo. Photons during bad runs and those arriving while the satellite was in the South Atlantic Anomaly are excluded using the `gtmktime` tool. The total exposure is calculated using the `gtexposure` tool. Time bins of one day width were then made with the `gtbin` tool to calculate an average daily flux.

These light curves are used to test a correlation between emission in GeV photons and TeV neutrinos in the analysis presented in Section 10.1. This method does not take into

account diffuse background emission, which is high for sources in the galactic plane. However, the analysis in Section 10.1 assumes a constant level of emission due to background and the quiescent source state.

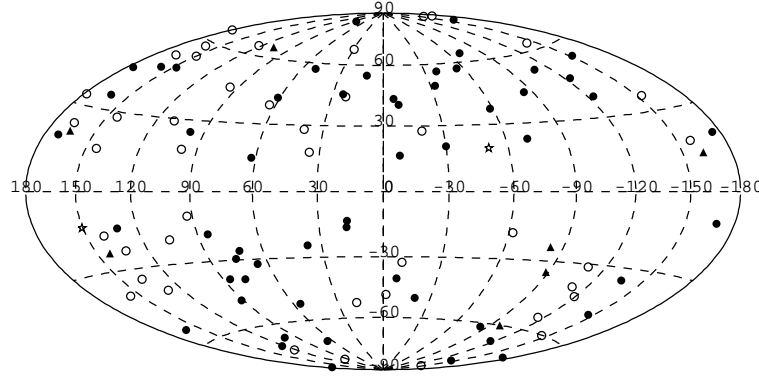


Figure 3.3 Map of the locations of the LAT Bright AGN Sources in galactic coordinates. FSRQs are marked as closed circles, BL Lacs as open circles, Uncertain type as closed triangles, and Radio Galaxies as open stars. Figure from [105].

### 3.2.3 Ground-Based Observatories

At photon energies above 1 TeV, satellite based observatories no longer have the area necessary to get sufficient statistics for the purposes of point-source astronomy. TeV energy photons interacting in the atmosphere create electromagnetic cascades through bremsstrahlung and electron-positron pair production. These cascades propagate down through the atmosphere in a thin pancake of photons and other particles which can be detected by ground based observatories.

Hadronically-induced showers are also detected and care must be taken to separate hadronic from photon showers. Hadronic showers will produce many more muons, which

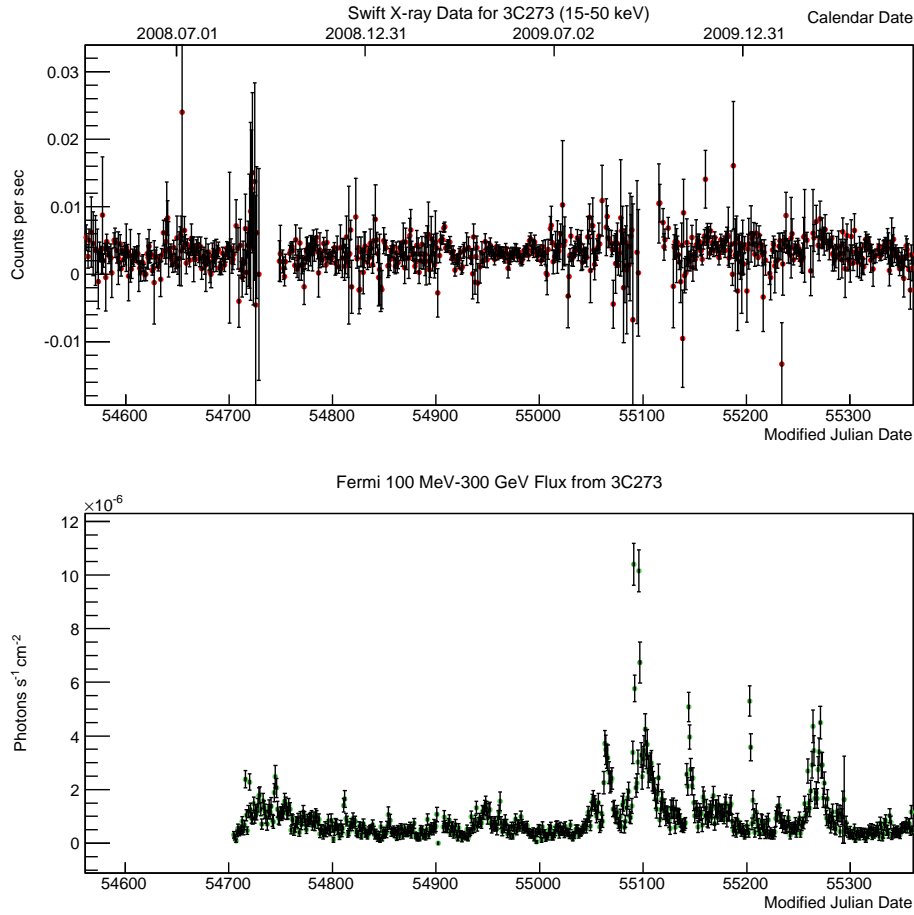


Figure 3.4 The light curves of the blazar 3C 273 from the Swift and Fermi telescopes, using 1-day binned data. The time scale covers the whole of the 40 and 59-string data taking. The source saw several large flares in photons of GeV energies during 2009 and 2010.

give the shower a profile which is clumped at certain locations with more energy near the muons. Muon production is strongly disfavored from photon showers, giving them a much more uniform signature.

### 3.2.3.1 Imaging Atmospheric Čerenkov Telescopes

IACTs use a telescope to focus the light from these cascades with about a  $4^\circ$  diameter view of the sky onto arrays of photomultiplier tubes, forming an image of the shower track. The photons created by the shower are detected directly. Due to this detection technique, data can only be taken on clear, moonless nights, resulting in a duty cycle of roughly 10%. The energy sensitivity ranges from 100 GeV to 10 TeV. Showers from hadrons typically appear blurrier compared to elongated and sharp showers from photons [106]. The first of this type of this detector is the single Whipple 10 m telescope, which first detected TeV photon emission from the Crab nebula [107].

Detecting the same shower in multiple telescopes, however, allows for a better angular resolution, on the order of  $0.05^\circ$  to  $0.1^\circ$ . The VERITAS array of four telescopes is located at the base camp of the Fred Lawrence Whipple Observatory in southern Arizona. MAGIC is a set of two 17 m diameter telescopes on the Canary Island of La Palma. The four 13 m telescopes of H.E.S.S. are located in the Khomas Highland of Namibia.

### 3.2.3.2 Water Čerenkov Detectors

A second method of detecting air showers from TeV photons is to have a ground array of detectors. The Milagro experiment [108] was a large water pool with outriggers located at Los Alamos, New Mexico that performed a scan of Northern Hemisphere sources. Milagro used two layers of photomultipliers 5m apart, the top layer detecting the electromagnetic component of showers and the lower layer is designed detect the muonic component. Another experiment, the High Altitude Water Čerenkov (HAWC) detector, consists of many independent tanks of water and is under construction in Mexico beneath the peak of the Sierra Negra mountain [109].

These detectors have a large field of view, but typically worse angular resolution than IACTs ( $\sim 1^\circ$  for Milagro). A shield is used to block out light, so Čerenkov light from the leptonic component of the shower is detected and used for reconstruction, leading to a high duty cycle which is not dependent on the weather or daylight.

## Chapter 4

### The IceCube Detector

The IceCube Neutrino Observatory is a kilometer-scale neutrino telescope situated at the geographic South Pole [6, 110]. It consists of three sub-detectors working in concert: IceCube, IceTop, and DeepCore, which are described here (see Figure 4.1). Each of the sub-detectors make use of one principal detector component, an optical detector with a 10-inch photomultiplier (PMT) with digital readout, or Digital Optical Module (DOM). The In-Ice portion of the detector is composed of a deep array of 86 strings each holding 60 DOMs, which are deployed between 1450 and 2450 m below the glacial surface. IceCube strings are horizontally separated by about 125 m with DOMs positioned vertically 17 m apart along each string. The bulk of ice above the detector shields muons from cosmic rays of less than 200 GeV from reaching the detector.

Eight of the IceCube strings in the middle of the detector have DOMs with high quantum efficiency photomultiplier tubes and a smaller spacing than the rest of the detector: 6 strings with 70m spacing and two more with spacing of 42m. All 8 of these strings have 7m vertical spacing between DOMs, which are placed in the bottom half of the detector, where the ice is the clearest. These 8 strings, along with the seven neighboring strings represent the DeepCore sub-detector, the purpose of which is to improve the neutrino energy detection

for energies below 1 TeV. Because Deep Core is situated in the center of the detector, the outer strings can be used to veto down-going cosmic ray muons and select neutrinos which interact inside of the DeepCore fiducial volume.

A surface array, IceTop, consists of 162 tanks of highly pure ice, each with two DOMs frozen to the top of the ice. Each of the 81 stations has two tanks, placed near the top of the main grid of strings. IceTop is designed to detect the electromagnetic component of cosmic ray air showers. This information can be used to reject events seen in the ice as being from air showers for tracks less than  $\lesssim 30^\circ$  from vertically down-going.

The construction of IceCube started with the first string installed in the 2005-6 season [111] and was completed in the austral Summer of 2010-11. The configurations of IceCube that have been used for the analyses performed in this thesis are shown in Figure 4.2.

The prototype for IceCube, the Antarctic Muon And Neutrino Detection Array (AMANDA), consisted of 677 optical modules with 8-inch PMTs arranged on 19 vertical strings mostly between 1500 and 2000 m below the surface. Ten of these strings were deployed before 1997, and the final nine were added by the 1999-2000 austral summer. AMANDA operated independently from 2000-2006, after which it was integrated into IceCube. AMANDA was decommissioned in 2009, and is not used in this work.

## 4.1 Digital Optical Module

IceCube is composed of thousands of independent data acquisition (DAQ) devices. The electronics of each DOM (see Figure 4.3) are housed in a 35.6cm diameter, 13mm thick sphere of borosilicate glass. This bathysphere is designed to resist a pressure of up to 400 atm, which can withstand the pressure of deployment and the re-freezing of the ice afterwards.



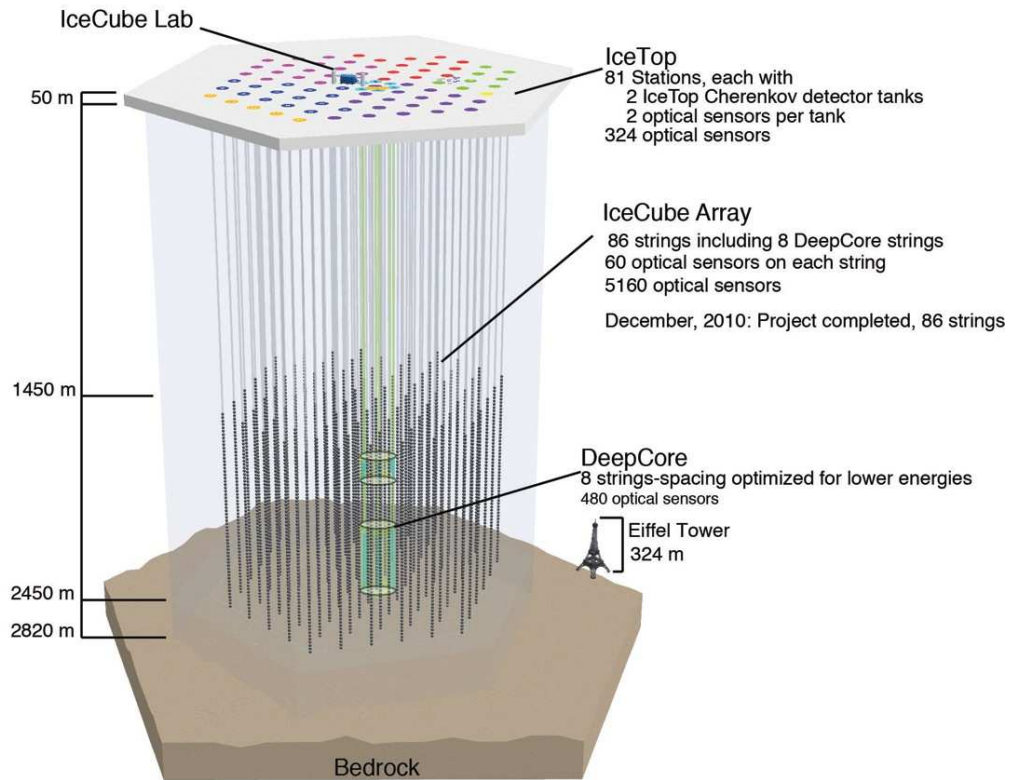


Figure 4.1 Schematic view of the IceCube Neutrino Observatory and its sub-detectors at the geographic South Pole.

The most prominent feature of each DOM is a R7081-02 Hamamatsu photomultiplier (PMT) with a diameter of 25 cm [112]. The quantum efficiency of the PMT peaks at 25% for light with a wavelength of 390 nm, and the spectral response is between 300-650 nm. The PMT is optically coupled to the glass with a layer of silicone gel. A mu-metal grid of a nickel-iron alloy shields the photomultiplier from the Earth's magnetic field, which would otherwise degrade the collection efficiency of the PMT. Each DOM also contains a modular, digitally-controlled high voltage supply for the PMT.

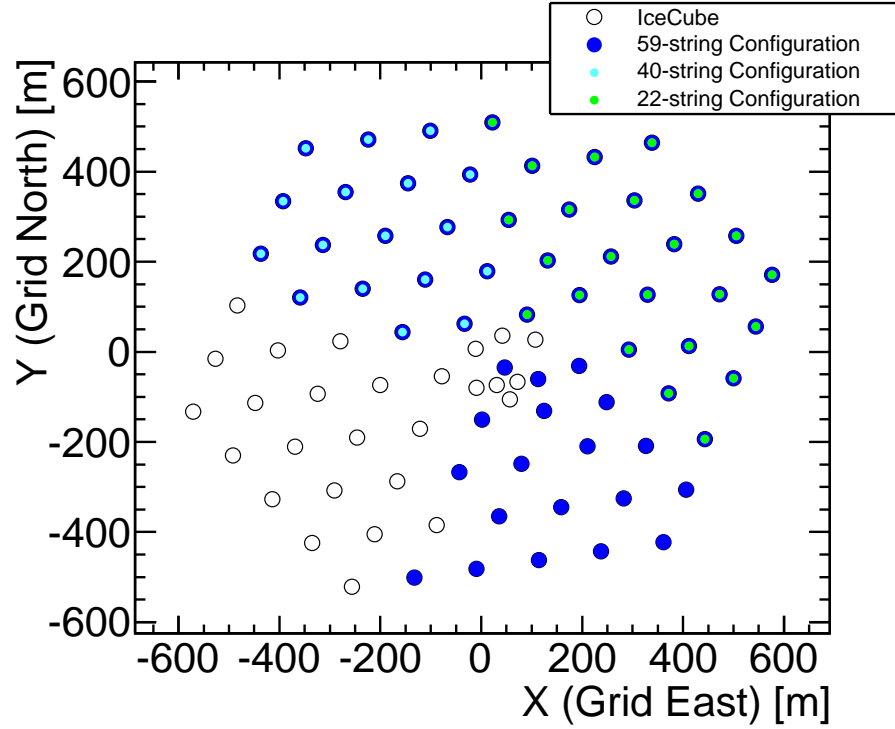


Figure 4.2 The growing IceCube detector seen from the top. Filled circles inside empty circles indicate deployed strings for each configuration, where all strings used in the 40-string configuration were also used in the 59-string configuration, and likewise all strings in the 22-string configuration were used in larger configurations.

A main electronics board in each DOM [113] reads, digitizes and time-stamps the analog PMT anode signals. This is done with two types of waveform digitizers. First, an Analog Transient Waveform Digitizer (ATWD) chip collects 128 samples for the first 420 ns. Three digitizers act in parallel on the signal fed through amplifiers with gains of  $\times 16$ ,  $\times 2$  and  $\times 0.25$ . The data uses the highest unsaturated gain channel. Two chips are included because after triggering, the ATWDs take  $29 \mu\text{s}$  to perform the digitization and reset and are used alternately to minimize dead time. The PMT signal to the ATWDs is read through

a line on the delay board, allowing digitization of roughly 70 ns of waveform before the trigger. The second waveform digitizer is a fast Analog to Digital Converter (fADC) which takes 256 samples of the PMT voltage over  $6.4 \mu\text{s}$ . This gives a coarser sampling than with the ATWD, but the fADC has a much longer readout time and a dead time of only two clock cycles (50 ns) between separate readouts. The transmission of the data after digitization to the surface are handled by field-programmable gate arrays (FPGAs), also on the main board.

Finally, the DOM contains a flasher board with twelve light emitting diodes (LEDs), which are used for *in situ* calibration of the ice properties. Half of the LEDs point radially outwards from the top half of each DOM and the rest are angled upward at an angle of  $48^\circ$ . The flashers are typically peaked at a wavelength of 405 nm, though during the 2010/11 deployment season, DOMs with LEDs peaked at 340, 370, 450, and 505nm were also deployed to study the wavelength dependence of the scattering and absorption in the ice.

All DOMs are connected to the surface via twisted-pair cables which enter the DOM on the penetrator assembly. On the surface near each string is a junction box where the IceTop DOMs are connected, and a cable to the IceCube Lab (ICL) connects each string to a single DOM Hub for readout.

## 4.2 Trigger and Data Acquisition

Hits on DOMs can come in two modes. Hits which arrive within  $\pm 1 \mu\text{s}$  from another hit on the neighbor or next-to-nearest neighboring DOM on the same string register as Hard Local Coincidence (HLC) hits. All other hits are referred to as Soft Local Coincidence (SLC) hits. The HLC correlation condition greatly reduces the noise rate due to PMT noise

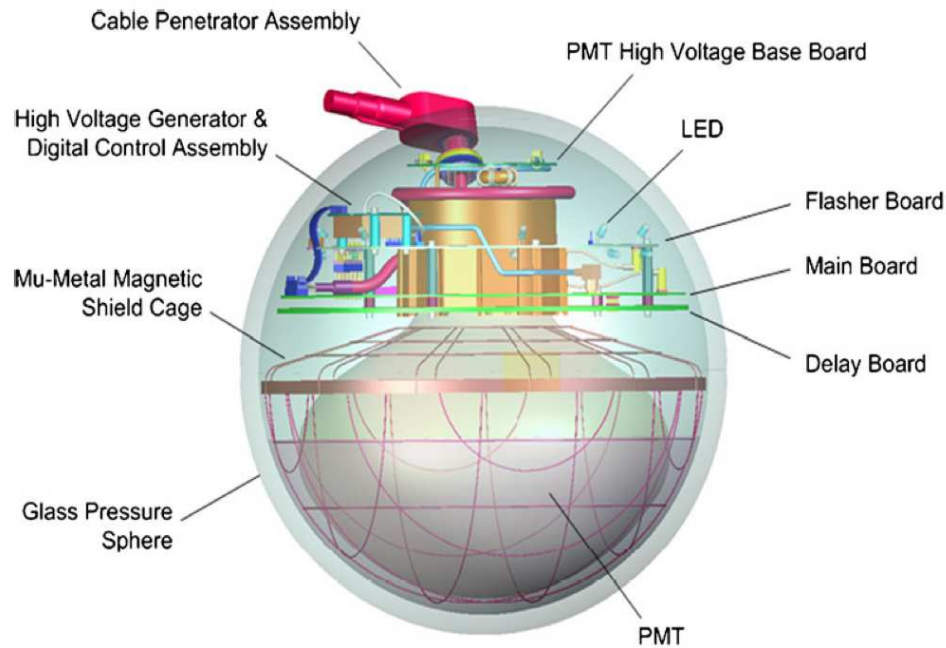


Figure 4.3 Outline of the IceCube Digital Optical Module, with component pieces labeled.

or photons from radioactive decay in the glass housing. SLC hits were kept starting with the 59-string data taking period for improved reconstruction of low-energy events and enhanced capability to identify neutrinos which interact inside of the detector.

IceCube uses a simple multiplicity condition as the primary in-ice trigger. It requires that at least eight DOMs are triggered within  $5 \mu\text{s}$ . For a DOM to trigger, it is required that the DOM PMT voltage crosses the discriminator threshold (0.25 of a typical photoelectron), and that this “hit” is in coincidence with at least one other hit on the nearest or next-to-nearest neighboring DOMs on a string within  $\pm 1 \mu\text{s}$  (i.e. that the hits meet the HLC condition). Once the simple multiplicity condition is satisfied in the 40 and 59-string detectors, information from all triggered DOMs within a  $\pm 10 \mu\text{s}$  window is read out and merged to create an event. This means that  $20 \mu\text{s}$  is the effective limit on how close two events

can be in time for the 59-string or 40-string data. Improvements in physics event definition removed this constraint for data taken with the completed detector.

Once transmitted to the surface, the digitized waveforms are read over using a Bayesian unfolding algorithm, extracting the total number of photoelectrons and their arrival times (hits) using a template single photoelectron response. These hits are used in various event reconstructions to determine if events pass one of the filters for transmitting the event information over the satellite.

Standard IceCube data-taking runs are eight hours long, with roughly two minutes between the end of one run and the beginning of the next. Downtime can be due to runs with active flashers, calibration runs, or temporary issues. IceCube has approximately a 99% uptime for data taking, but not all data is useful for analysis. Calibration runs (prevalent during the commissioning of new strings after deployment) and runs with active flashers are excluded. Also, some runs will have one or multiple strings missing while problems with particular DOMs are fixed. These runs remain capable of detecting extraordinary astrophysical events, such as a galactic supernova or a particularly bright GRB.

Runs which fail within 20 minutes are typically unstable and are excluded in analysis. Run monitoring in the North is performed for all runs to check for rate irregularities for individual filters and individual DOMs and to check DOMs for other issues, such as a higher current draw or a change in the PMT response shape or temperature. We further monitor the rate of each run and check for any deviation from a rolling average which accounts for seasonal and temperature variations [114]. To ensure stable detector conditions, the event rates of runs are required to be within  $5\sigma$  from a rolling average over  $\pm 2$  days. This loose constraint allows for short-term weather variability.

### 4.3 Optical properties of the South Pole Ice

The glacial ice beneath the South Pole is the clearest material known for wavelengths between 330 and 500 nm [115], but it has deposits of dust of varying amounts in layers depending on the global climate at the time the ice was formed (up to  $\sim 200,000$  years ago, see [116]). Characterizing the optical properties and how they change in the glacier is important to properly simulate light in the detector. The major variation in the optical properties of the ice of the instrumented volume between 1450 and 2450 m is the presence of vertical variations in the dust concentrations due to changes in the climate and volcanic activity, which alter the scattering and absorption coefficients in those layers (see Figure 4.4). Less than 1400 m below the surface of the glacier, air bubbles are the primary cause of scattering of light in the glacier. Below this depth, the pressure from the ice above over time has caused the air and ice to form clathrates, and dust particles are the primary cause of scattering. For IceCube, the light seen by PMTs has typically been scattered several times.

The simulation of scattering follows the Mie treatment of [115], which is highly peaked in the forward direction, with  $\langle \cos \theta \rangle = 0.94$ . The effective scattering length,  $\lambda_e$ , is defined in terms of the scattering length  $\lambda_s$  and the mean scattering angle:

$$\lambda_e = \frac{\lambda_s}{1 - \langle \cos \theta \rangle} \quad (4.1)$$

which functions as the distance required to randomize the direction of an average photon. IceCube has an average effective scattering length of about 20 m for light at 400 nm, the peak of the Čerenkov spectrum, which is much shorter than the typical absorption length of 110 m. This compares to neutrino telescopes in water, such as ANTARES in the Mediterranean Sea, where the effective scattering length is significantly longer at 100 m, while the absorption length is shorter at 57 m [117].

One additional characteristic of the ice results from the residual air bubbles left in the column melted during deployment of the DOMs. Since the 2010/11 austral summer, a video camera deployed at the bottom of one of the IceCube strings has made observations of the re-freezing. The camera has observed that the hole freezes from the outside in, forcing the air bubbles toward the center of the region. This leaves only a narrow column of ice with higher scattering than the surrounding glacial ice. Functionally this line of ice with more scattering intersecting with the DOMs smooths out the angular response function of the PMTs.

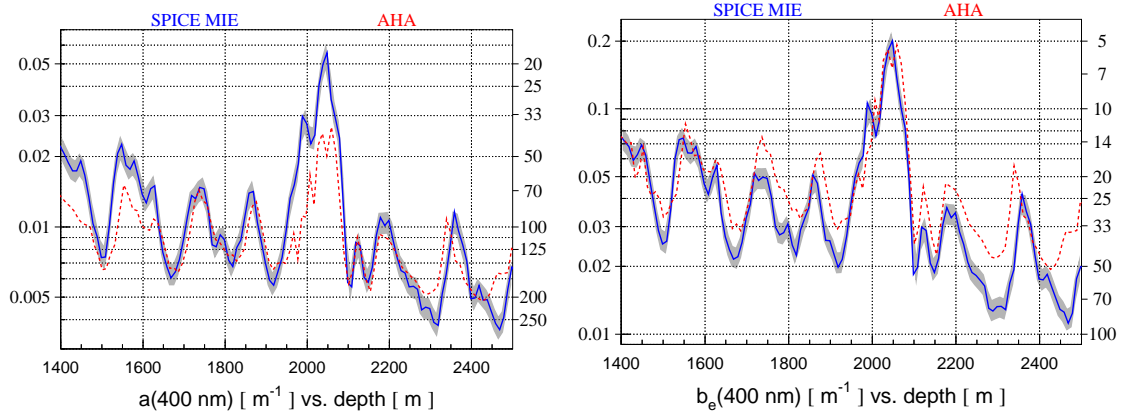


Figure 4.4 The parameters of the scattering length and absorption versus depth used to model the South Pole ice. Shown are two models of the ice properties: the AHA model [115] which was first developed using flasher data from the AMANDA detector and extrapolated to the deep ice using dust logger data, and the SPICE MIE model [118] which is more recent and uses an iterative fit with IceCube flasher data to model the dependence of the scattering and absorption versus depth.

## 4.4 Data Filtering

Due to constraints on the amount of data which can be transmitted to the Northern Hemisphere via satellite from the South Pole, IceCube uses various filters to select events for transmission. All events, however, are saved on tape and physically transported to the North every year. All events have initial reconstructions performed using track and cascade-based hypotheses, some of which are selected for transmission over satellite to the Northern Hemisphere for additional processing and analysis. The muon filter focuses on the selection of upward-going track-like events.

Before quality cuts or prescale factors are applied, IceCube data are dominated by down-going atmospheric muons. This is the case in the up-going signal region as well, because a small fraction of atmospheric muons are misreconstructed as up-going and must be rejected in the process of applying analysis cuts. This is mainly due to light which does not fit a single track hypothesis, such as noise or light due to multiple particles passing through the detector in a short time.

The atmospheric muon rate exhibits a seasonal variation of roughly  $\pm 10\%$  due to changes in density of the atmosphere at the South Pole [114]. This variation in the rate of up-going muon-filtered events for three detector configurations can be seen in Figure 4.7. During the austral summer when the atmosphere is warmer, the fraction of pions and kaons in air showers that decay before interacting is increased compared to the fraction in winter. The muon rate also varies several percent on timescales of several days as a result of weather phenomena in Antarctica. For up-going atmospheric neutrinos the seasonal variations are smaller, approximately 5%, because neutrinos are created over a wide range of Earth's latitudes compared to the atmospheric muons created near the South Pole.



	40-strings	59-strings
Triggered events	$3.3 \times 10^{10}$	$4.2 \times 10^{10}$
Track-like filtered events	$8.0 \times 10^8$	$1.0 \times 10^9$
Events in final sample	36,900	107,569

Table 4.1 Summary of the total number of events which trigger IceCube, pass filter selection, and are used in the final point-source selections from the 40 and 59-string configurations.

Filters include the muon filter for track-like events, the cascade filter for spherically-shaped events, the extremely high energy filter for events with a large amount of detected light, and the minimum bias filter, which selects a sample of all events with a specified prescale factor. The number of all triggered events, muon-filtered events, and events in the final analysis sample can be seen in Table 4.1.

Figure 4.5 shows an example of a cascade-like event from the 40-string detector. Figure 4.6 shows a high-energy down-going muon from the 59-string detector.

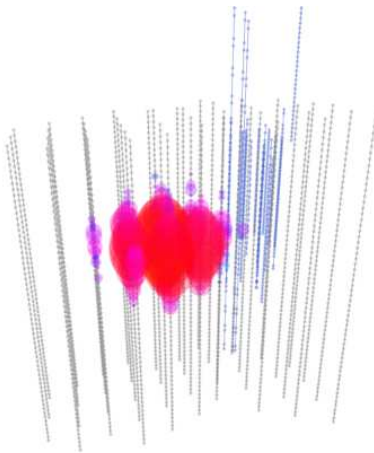


Figure 4.5 Example of an event from the 40-string data taking which was reconstructed as a cascade and passed the cascade-like filter. The color of the hits is a measure of timing; here we see a ball of light.

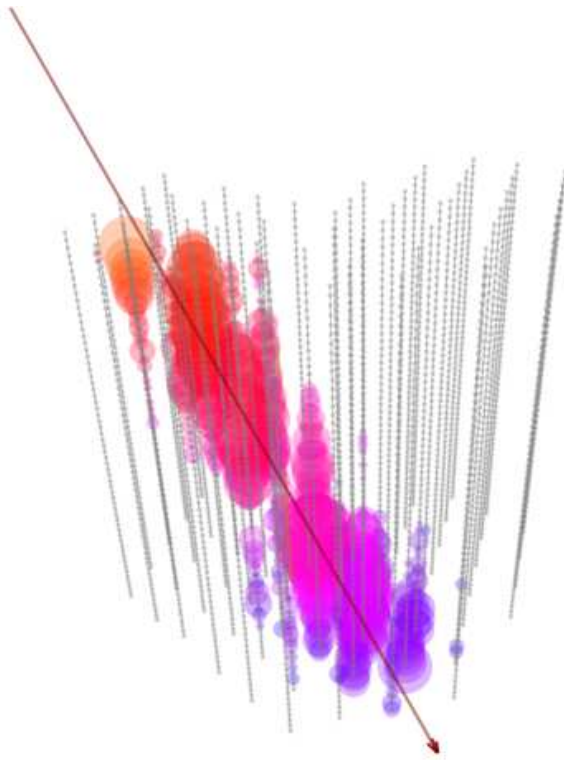


Figure 4.6 Example of an event from the 59-string data taking which was reconstructed as a high-energy down-going track and passed through the muon-like filter. The color of the hits is a measure of timing, with red representing earlier hits and purple later. The red line is the MPE track reconstruction of the event

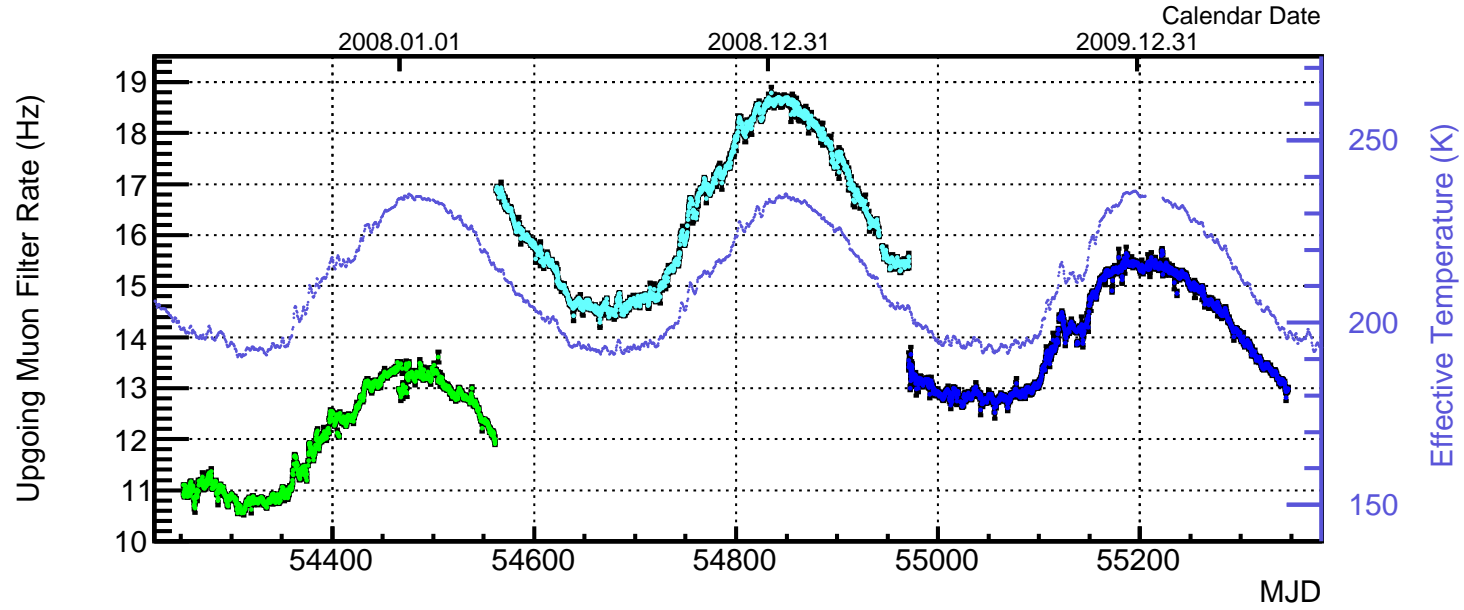


Figure 4.7 The rate per run of the filtered stream of muon events with zenith angle  $\geq 80^\circ$  selected at the South Pole for the 22-string (dark green points before MJD 54560), 40-string (light blue points between MJD 54560 and 54971) and 59-string (dark blue points after MJD 54971) detectors as a function of MJD. The small modulations around the main seasonal oscillation are due to short-term weather variability (plotted in light blue). The rate increase with respect to the 40 to 22-string data was due to the increased detector size; between the 40 and 59-string periods the muon filtered events required events to have better initial reconstruction parameters, so the filter rate decreases slightly to conserve satellite bandwidth. The effective temperature can be seen in lavender.

## Chapter 5

### IceCube Event Reconstruction

This chapter focuses on the treatment of the data after the initial filtering at the South Pole and transmission to the North and before the final event selection for analysis. This treatment involves performing a number of muon reconstructions on the data, with the goal of finding a track which represents the data well. This chapter describes the first-guess reconstruction, as well as likelihood-based reconstructions, which use information about scattering and absorption of light in the ice. Different methods of hit cleaning are also covered.

Several different assumptions are made in different reconstructions. Some assumptions are designed to find mis-reconstructed background and use the down-going atmospheric muon distribution as a starting point, others assume that the event is best described as two separate muon tracks.

#### 5.1 Hit Cleaning

The first step in cleaning hits is to remove hits from DOMs which are known to have issues; some do not communicate, some have high current throughput or high noise rates compared to other DOMs, and some have a broken local coincidence connection to neighboring DOMs. For the 40 and 59-string configurations, bad DOMs are only about 2% of the

total deployed.

The event builder at Pole uses all hits from  $\pm 10 \mu\text{s}$  from the trigger, which is much wider than the transit time of a particle from one side of the detector to the other ( $3.3 \mu\text{s}$  per km). This means that the readout window can contain a significant amount of noise or even multiple particles from separate air showers. This additional light in the detector which is not described by a single-track hypothesis can confuse the reconstructions, causing good neutrino events to be cut out or, more likely, to cause atmospheric muons to appear to make up-going tracks. A first hit cleaning designed to minimize the effect of noise is used to select hits in each event with a sliding time window of  $6 \mu\text{s}$ . It scans over the entire readout window and selects the time window where the sum of the charge of hits in the window is at a maximum, thus retaining the most information with which to reconstruct the track. The hits outside that window are removed and are not used for reconstruction. Other implementations of hit-cleaning algorithms are used at higher levels of processing in order to better distinguish coincident events and noise hits (see Section 5.3).

Additional work has been done such that offline reconstructions can be done using a dynamic, topologically motivated hit cleaning. This technique was used in the analysis of the 59-string data as a part of the cut logic, but will be used starting with the 79-string data to split separated hits from one trigger of the detector into topologically separate events for physics analysis.

## 5.2 Track Reconstructions

This work only considers track-like events depositing light in the detector. Other analyses, however, can look for cascade-like spheres of light inside the detector due to electron neutrinos or neutral current interactions. For all reconstructions we find the parameters of

some track:

$$\vec{a} = (\vec{r}_0, t_0, \theta, \phi, E_0) , \quad (5.1)$$

where a particle with energy  $E_0$  passes through some position  $\vec{r}_0$  at time  $t_0$ , moving in the direction given by the zenith and azimuthal angles  $(\theta, \phi, \text{respectively})$ .

### 5.2.1 Line Fit First-Guess Reconstruction

The initial reconstruction done on all events uses all HLC hits to reconstruct an event as a plane wave passing through the detector. This is used to calculate the average velocity  $\vec{v}$  in each direction ( $x, y$ , and  $z$ ) to form a track passing through the center of gravity for the event, which is calculated using the charge to weight each DOM. The assumption is that the hits can be described as the plane wave passes through the detector, so the position of each hit  $\vec{r}_i$  can be described as:

$$\vec{r}_i = \vec{r}_0 + \vec{v}t_i \quad (5.2)$$

where  $\vec{r}_0$  is the initial location and  $t_i$  is the time of the  $i$ th hit since some  $t_0$ . The  $\chi^2$  distribution of the hits is then:

$$\chi^2 = \sum_i (\vec{r}_i - \vec{r}_0 - \vec{v}t_i)^2 . \quad (5.3)$$

This can be minimized analytically by differentiating with respect to  $\vec{r}_0$  and  $\vec{v}$ , yielding the direction and vertex of the track:

$$\vec{r}_0 = \langle \vec{r}_i \rangle - \vec{v} \langle t_i \rangle \quad (5.4)$$

and

$$\vec{v} = \frac{\langle \vec{r}_i t_i \rangle - \langle \vec{r}_i \rangle \langle t_i \rangle}{\langle t_i^2 \rangle - \langle t_i \rangle^2} . \quad (5.5)$$

In the data processing this track and starting vertex are used as the first guess for an initial track reconstruction using a maximum likelihood method.

### 5.2.2 Maximum Likelihood Track Reconstruction

More sophisticated reconstructions use the information about the angle of Čerenkov radiation with respect to the particle track and the expectation of scattering and absorption in the ice to define the likelihood of observing a photon at a particular time and distance from a particular muon track. The goal is to reconstruct a set of unknown muon track parameters  $\vec{a}$  given a series of photon arrival times and locations  $\vec{x}_i$ .

The likelihood  $\mathcal{L}$  of a track  $\vec{a}$  given the data  $\vec{x}_i$  is the product of the probabilities of each hit:

$$\mathcal{L} = \prod_i p(\vec{x}_i | \vec{a}) , \quad (5.6)$$

where  $p(\vec{x}_i | \vec{a})$  is the probability density function (PDF) of observing each hit  $\vec{x}_i$  given the muon track parameters  $\vec{a}$ . The best-fit track is not calculable analytically, so  $-\mathcal{L}$  is minimized using a numerical minimizer, MINUIT [119]. The MINUIT SIMPLEX routine is used, and iterated with different starting conditions to increase the chances of finding the global minimum for the event, which is the most likely track.

The expectation of the photon arrival times at each hit DOM at location  $r_i$  would be:

$$t_{exp} = t_0 + \frac{d(\vec{r}_i - \vec{r}_0 + d \tan \theta_c)}{c} \quad (5.7)$$

with  $d$  as the closest approach of the muon track to the DOM and  $\theta_c$  the Čerenkov angle in the medium. The time residual of the hit is calculated as the difference between the expected and actual ( $t_{hit}$ ) hit times:

$$t_{residual} = t_{hit} - t_{exp}. \quad (5.8)$$



The likelihood reconstruction models the track as a series of hits at a certain distance  $d$  from the track with a certain timing offset from a direct photon of  $t_{\text{residual}}$ .

### 5.2.2.1 Pandel Function

In order to use scattering and absorption of light in the ice in particle reconstruction, an analytic expression is used to characterize photon propagation. The Pandel function [120] is this analytic expression, which is designed to express the distribution of Čerenkov photons from a particular track arriving at each hit DOM at the reconstructed time residual:

$$p(t_{\text{residual}}) = \frac{1}{N(d)} \frac{\tau^{-\frac{d}{\lambda}} t_{\text{residual}}^{\frac{d}{\lambda}-1}}{\Gamma(d/\lambda)} e^{-\left(t_{\text{residual}}\left(\frac{1}{\tau} + \frac{c}{n\lambda_a} + \frac{d}{\lambda_a}\right)\right)} \quad (5.9)$$

where

$$N(d) = e^{\frac{-d}{\lambda_a}} \left(1 + \frac{c\tau}{n\lambda_a}\right)^{\frac{-d}{\lambda}}. \quad (5.10)$$

Here  $n$  is the index of refraction of the ice,  $\lambda_a$  is the absorption length with an average value of 98 m, and  $d$  is the distance of the detected photon from its point of emission.  $\Gamma(d/\lambda)$  is the Gamma function and  $N(d)$  is a normalization factor. Parameters  $\lambda$  and  $\tau$  are free parameters determined by Monte Carlo simulation. The time residual probability distribution for two different distances can be seen in Figure 5.1.

### 5.2.2.2 Single Photo-Electron

This first method uses the time of only the first hit in each DOM but the photon arrival expectation distribution for an arbitrary photon from the track (hence single photo-electron, or SPE). This method uses the Line Fit first guess as a seed, and is run with one iteration for the online filtering of events. The process of testing multiple initial conditions designed to evenly fill the zenith and azimuth space was run 32 times in the offline processing of

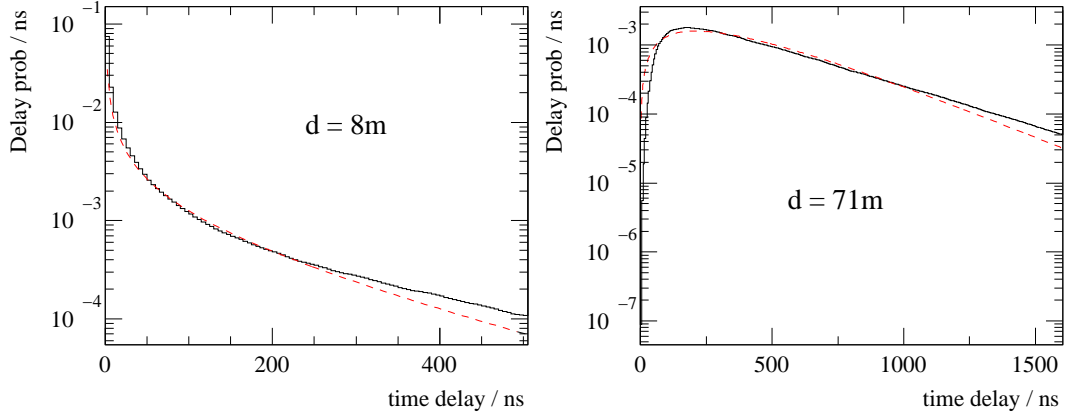


Figure 5.1 Diagrams of the time residual distribution comparing the Pandel function (dashed curves) to the detailed simulation (in black) at two distances from the simulated muon track.

40-string data, while 8 iterations were found to be sufficient for the 59-string data.

### 5.2.2.3 Multiple Photo-Electron

This formation of the likelihood uses the timing of the first hit with the photon arrival expectation for the correct number of hits (hence multiple photo-electron, or MPE). Each DOM which has more than one photon is given an additional weight in the likelihood. The multiple photo-electron PDF for the first of  $N$  photons can be constructed as

$$p_N^1(t_{\text{residual}}) = N p_1(t_{\text{residual}}) \left( \int_{t_{\text{residual}}}^{\infty} p_1(t) dt \right)^{N-1}. \quad (5.11)$$

This is also useful for the fact that the first photoelectron will typically experience less scattering than an average photon. This reconstruction typically uses the result of the Single Photo-Electron reconstruction as a first guess. That reconstruction is better at sampling the likelihood space over the sky to find the global minimum, since the additional information from the number of hits per DOM causes the likelihood space of the track on the sky to have more features and local minima, and as such it requires a starting point near the global

minimum.

#### 5.2.2.4 Paraboloid Fit

This reconstruction samples the likelihood space near the minimum found in the MPE track fit, testing the likelihood values of tracks with a known angular offset from the best track, and fits a two-dimensional parabola to the result. The point where the likelihood is half of the value of the maximum is defined as the average expected error of the event [121]. Three concentric circles with a maximum radius of  $2^\circ$  with eight sampling points on each are used, so this reconstruction typically takes 24 times longer than the basic likelihood fits. In practice a correction factor is applied as a function of energy using simulation due to additional stochastic losses not modeled by the Pandel function (see Figure 5.2).

The fits to the functions use the reconstructed energy of the MPE track  $E_{\text{MUE}}$ , and are different in the 40-string and 59-string data. The rescaling function used for the 40-string data is:

$$\sigma'_{\text{MPE}} = \sigma_{\text{MPE}} \times (5.916 - 2.340 \times \log_{10}(E_{\text{MUE}}) + 3.219 \times \log_{10}(E_{\text{MUE}})^2), \quad (5.12)$$

and for the 59-string data it is:

$$\sigma'_{\text{MPE}} = \sigma_{\text{MPE}} \times (31.91 - 24.56 \times \log_{10}(E_{\text{MUE}}) + 7.197 \times \log_{10}(E_{\text{MUE}})^2 \quad (5.13)$$

$$- 0.9082 \times \log_{10}(E_{\text{MUE}})^3 + 0.04311 \times \log_{10}(E_{\text{MUE}})^4). \quad (5.14)$$

#### 5.2.2.5 Bayesian Track Reconstruction

This method uses the known zenith distribution of muons from cosmic ray showers as an additional weight in the Pandel likelihood method. The known zenith distribution is fit

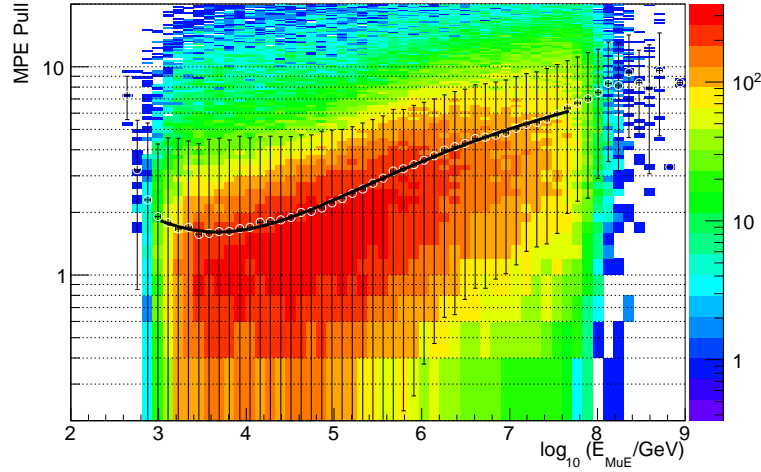


Figure 5.2 A plot of the uncorrected pull distribution of the MPE paraboloid reconstruction versus energy for the 40-string configuration. The pull is the angle between the true and reconstructed tracks divided by the reconstructed angular error, so values larger than one indicate a reconstructed error which is too small. In practice, at higher energies stochastic energy losses along the track confuse the reconstruction, causing a narrower minimum than should be found. Finding a narrower minimum is much more detrimental to point-source analyses, as this will cause events which come from a common source to appear from separate sources, increasing the signal needed to make a discovery. We apply a correction, which is done as a fit to the median of the pull distribution shown here.

with a polynomial and used as a prior using Bayes' theorem:

$$P(\vec{a}|\vec{x}) = \frac{P(\vec{x}|\vec{a})P(\vec{a})}{P(\vec{x})} \quad (5.15)$$

where  $P(\vec{a}|\vec{x})$  is the probability of there being a muon track with parameters  $\vec{a}$  given the set of hits  $\vec{x}$ . The probability using the Pandel formula of a muon to produce a set of hits is  $P(\vec{x}|\vec{a})$ , and  $P(\vec{a})$  is the prior probability from the known distribution of cosmic ray

muons. This weight requires the track to have a zenith angle above the horizon. Because the background due to air showers is  $O \sim 10^5$  larger than the neutrino background, the ratio of the likelihoods from the Bayesian and standard reconstructions is a powerful rejection factor for events in the up-going region.

### 5.3 Coincident Muons

Roughly 10% of events at trigger level have more than one atmospheric muon in the detector in a single readout window. The atmospheric muon spectrum is quite steep, so often only one particle is easily identifiable. Typically noise in the detector is handled appropriately by the reconstruction algorithm, even when there are two separate air shower muons in the detector at the same time. Occasionally, however, noise hits or multiple tracks will be offset with the proper time to mimic a through-going track. If the timing of two of these tracks is right, it can mimic the signature of an up-going track, and also receive a very good track likelihood value. This background can be rejected more efficiently with track reconstructions done with specially cleaned portions of the hits. Two algorithms are used to split each event into separate sub-events.

#### 5.3.1 Split Track Reconstructions

A simple way of splitting events into different sets of hits is performed, which takes half of the events split both by the geometry and the arrival time of the hits. Each of the four sub-events has the standard likelihood track reconstructions applied. Events which are made of coincident muons will be expected to have one of the sub-events reconstructed as a down-going track. Upward going neutrinos will be expected to have both sub-events reconstructed as up-going tracks with a small space angle separating their direction.

### 5.3.2 Topological Trigger Hit Cleaning

A more sophisticated method of splitting events uses information about the average expected travel distance of a photon in the ice and the timing and the distance of hits for an event to iterate over all hits and separate them into causally-connected sub-events. The settings used for the 59-string processing counted hits as being causally connected when they were less than 300m apart horizontally (about two string spacings), fewer than 30 DOM spacings vertically (or 510 m), and were within 450 ns (roughly the expected lifetime of photons in the detector) from being consistent with coming from the same track-like event.

We introduced this hit cleaning in the 59-string muon event processing as a cut parameter. A cut was applied to events where the event was reconstructed as up-going, but the largest topologically split sub-event was reconstructed as down-going. This method is especially useful in rejecting coincident events. If a different series of hits was found by the topological splitting, up to three sub-events were kept and had the first-guess reconstruction, 8-fold iterative SPE and a final MPE fit performed on the separated hit clusters. In setting up the muon processing, other settings for determining the connected-ness of hits were tested, and we found that the settings used were in a broad minimum where 40 to 50% of misreconstructed down-going events were split up and correctly found to be down-going, while only 1% of up-going neutrino-induced muons were mistakenly split and found to be down-going. An example of a coincident muon event divided by the topological trigger can be seen in Figure 5.3.

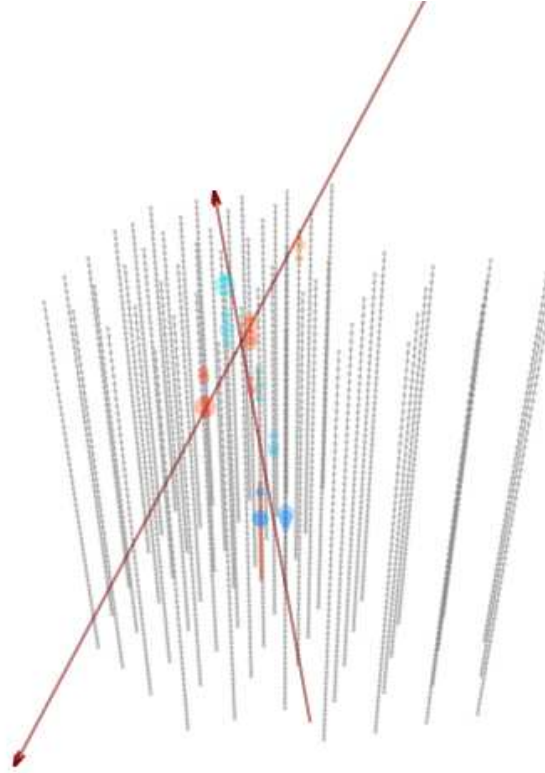


Figure 5.3 Example of an event from the 59-string data taking which was split up by the Topological Trigger algorithm. The color of the hits is a measure of timing, here we see an up-going event in blue and a down-going event in orange. The red lines are track reconstructions performed on the separated hit series.

## 5.4 Energy Reconstruction

The energy of the particle is determined by the  $MuE$  energy reconstruction algorithm. It uses the average density of the photons along the muon track compared to the density expected given a certain energy. The reconstruction requires a track as the seed, and it uses this seed track to calculate the photon density using the DOM angular acceptance, distance

to the track, and the scattering and absorption in the ice. Above energies of roughly 1 TeV, the energy loss per meter water equivalent scales with the energy of the muon (see Section 1.2.2). The energy resolution is roughly 0.3 in  $\log_{10}$  of the muon energy at closest approach to the center of the detector for particles with energies between  $\sim 10$  TeV and  $\sim 100$  PeV. Figure 5.4 shows the distribution of this energy of the particle in the detector versus the true neutrino energy for a simulated spectrum  $d\Phi/dE \propto E^{-2}$ .

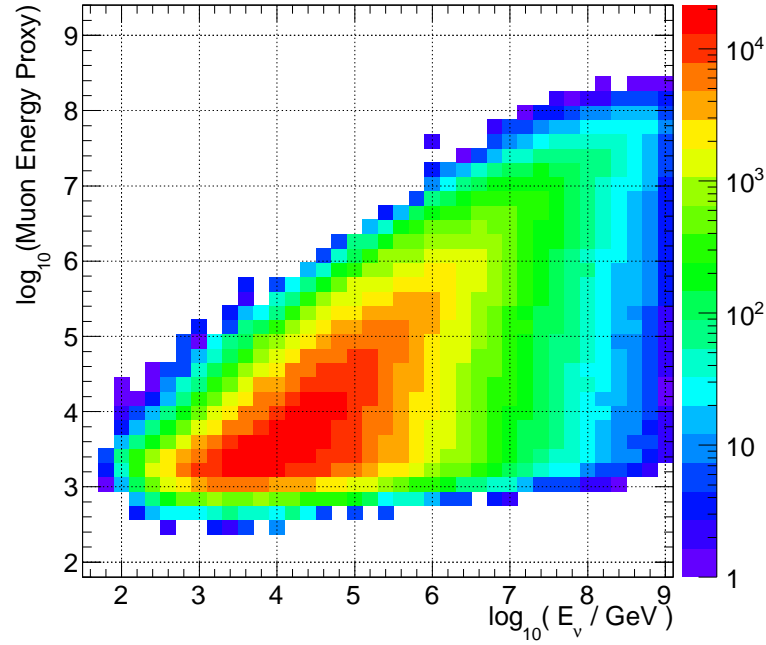


Figure 5.4 Plot of the reconstructed muon energy in the detector vs the primary neutrino energy for events from 59-string data-taking used in analysis for a flux  $d\Phi/dE \propto E^{-2}$ . The z-axis is in arbitrary units.



## Chapter 6

### The 40 and 59-string Datasets

This work utilizes data taken with both 40 and 59 strings of IceCube. The detector took data with the 40-string configuration from April 5, 2008 until May 20, 2009, and the 59-string configuration from May 20, 2009 until May 31, 2010.

IceCube data at trigger level is overwhelmingly due to muons produced in cosmic ray air showers, of which a small fraction are mis-reconstructed as up-going tracks. Even then, this fraction is many times more prevalent than the flux of atmospheric neutrinos. This requires us to develop and apply quality selection criteria to achieve a sample from the upward-going region, which consists predominantly of neutrinos. The datasets also include a sample of high-energy muons from cosmic ray air showers in the down-going region. The expected spectra of neutrino sources is harder than that of the atmospheric muon flux, and the goal is to leverage this difference to search for sources of PeV to EeV energy neutrinos on top of the background of atmospheric muons.

There were several changes in the method of data processing and event selection between the 40 and 59-string configurations, which will be covered below.

## 6.1 Event Selection Techniques

One method of event selection is for the analyzer to manually choose a set of cuts, testing the fraction of signal versus the fraction of background kept for a range of values for each parameter. This process is iterated over for several different variables, to find the most efficient parameter to cut on at each stage until a data sample of sufficient purity of atmospheric neutrinos is obtained. The purity is typically  $\gtrsim 95\%$  for a time-integrated analysis, but it could be lower for analyses with strong *a priori* cuts in time, such as a GRB analysis. This method was used in the selection of the 40-string sample [27], and was tested against a Boosted Decision Tree event selection for the 59-string sample.

A Boosted Decision Tree (BDT) is a machine learning algorithm designed to separate two different populations. The decision tree is similar to the manual selection of cuts described above in that an automated program makes a series of choices on predefined cut parameters, choosing at each step which is the most efficient in sequence at separating signal and background for a given sample. Implementing this as an automatic algorithm allows for a more complex iterative process, where for each step in the decision tree both the signal-like and background-like samples are tested for the next best cut parameter and value. The boosting concept takes the signal events which were labelled as background and gives additional weight in the cut selection of the next formulation of the decision tree.

The choices for the input parameters to the decision tree include the event quality parameters that are used to cut on, the number of branching levels for each decision tree, a minimum number of events in a branch for it to be considered to be split again, and a maximum number of iterations of the decision tree and boosting process before a final result is produced.

After the algorithm finds a final result, it gives each event a score from  $[-1,1]$  (see Figure 6.4), where higher numbers indicate more signal-like events. We use the scores from several different trees to characterize each event: two spectral signal weights are used, one for the expected  $E^{-2}$  spectrum for Fermi acceleration and one for a softer  $E^{-2.7}$  spectrum observed in Galactic cosmic rays below 3 PeV. Two BDTs are trained for each spectral weighting using separate sets of event quality parameters. This is found to be more computationally manageable than only using one tree with all parameters and yields similar results. The background data sample used is the data; this provides a more robust method of rejecting the background, which may include classes of events which are not produced in the simulation chain.

## 6.2 Data Selection

Data selection is done using parameters related to the quality and accuracy of the event reconstruction, including:

- **Reduced Log Likelihood:** The likelihood track reconstructions maximize the likelihood of the resulting track given the data. In practice, this likelihood increases with the number of hit DOMs ( $N_{\text{DOMs}}$ ), so a reduced log likelihood is used. The reduced log likelihood is the log likelihood divided by the number of hit channels minus five ( $\log \mathcal{L}_{\text{MPE}} / (N_{\text{DOMs}} - 5)$ ), or the number of degrees of freedom in the track fit. It is observed that this quantity has a slight dependence on the energy of the event, toward selecting higher energy events. This is modified by another method of creating a reduced log likelihood, the  $\log \mathcal{L}_{\text{MPE}} / (N_{\text{DOMs}} - 2.5)$ , which is found to be a track quality parameter which does not depend on energy.

- **Line Fit Speed**  $|\vec{v}|_{lf}$ : The magnitude of the velocity vector as calculated by the initial Line Fit reconstruction is used to identify tracks which appear to be traveling at the speed of light. This can be a useful parameter to distinguish coincident muon events.
- **Angular Uncertainty Estimator**  $\sigma_{MPE}$ : The angular uncertainty estimate is a useful discriminator, as mis-reconstructed events tend to have a larger error estimate than events where the reconstruction finds a single muon track. This makes the angular uncertainty estimate a powerful cut parameter in addition to being used in point-source analyses. The details of the angular uncertainty calculation can be found in Section 5.2.2.4.
- **Muon Energy Reconstruction**  $E_{MuE}$ : The photon density along the track is compared with the expected density corrected for the effective area of the PMTs near the track. For muon energies above 1 TeV, stochastic losses dominate, and the estimator models the track as a sum of Čerenkov light and stochastic light due to bremsstrahlung, pair production, and photo-nuclear processes along the track. For muon energies above 10 TeV the energy resolution is 0.3 in  $\log_{10}(E)$ .
- **Number and Length of Direct Hits**  $N_{DirC}$  and  $L_{DirC}$ : Given the best-fit reconstructed track, the arrival time residuals of each photon are calculated. We use a time residual window of -15 ns to +75 ns to tag photons which are not believed to be scattered, because scattering delays the photons and reduces their directional information. Tracks with many direct hits and a longer maximum distance projected along the track between direct hits are typically better reconstructed.

- **Zenith-weighted log-likelihood ratio**  $\log(\mathcal{L}_{\text{SPE}}/\mathcal{L}_{\text{Bayes}})$ : The relative log-likelihoods of a track being from a cosmic ray air shower to the best-fit reconstruction are used to reject mis-reconstructed down-going tracks, which greatly outnumber up-going neutrino events. This requires the up-going track to be significantly more likely than the best-fit down-going track in order for the event to be included in the neutrino sample.
- **Minimum Zenith angle of Split reconstructions**  $\theta_{\text{split,min}}$ : The four tracks from the time and geometry split hit series are examined and the most down-going track zenith angle is used (i.e. the track which most looks like a down-going muon). For events which have good track reconstructions, the split hit series will give roughly the same direction of the track. In practice, it is found that the zenith angle is a better cut parameter than the space angle between the split reconstructions because nearly all mis-reconstructed events originate from air showers.

### 6.2.1 40-string Event Selection

The 40-string event selection was chosen with the aim of obtaining the best sensitivity for an  $E^{-2}$  spectrum neutrino flux. A full description is available in [122], while the cut

parameters are listed here:

$$\begin{aligned}
 & \left[ \sigma_{\text{MPE}} < 3^\circ \text{ AND} \right. \\
 & \quad \log \mathcal{L}_{\text{MPE}} / (N_{\text{DOMs}} - 5) < 8.3 \text{ AND} \\
 & \quad \left( \log \mathcal{L}_{\text{MPE}} / (N_{\text{DOMs}} - 5) < 8.0 \text{ OR } \log \mathcal{L}_{\text{MPE}} / (N_{\text{DOMs}} - 2.5) < 7.1 \right) \text{ AND} \\
 & \quad \theta_{\text{split,min}} > 80^\circ \text{ AND} \\
 & \quad \left( \log(\mathcal{L}_{\text{SPE}} / \mathcal{L}_{\text{Bayes}}) > 30 \text{ OR } \theta_{\text{MPE}} < 90^\circ \right) \text{ AND} \\
 & \quad N_{\text{Dir}} \geq 5 \text{ AND} \\
 & \quad \left. L_{\text{Dir}} > 200 \text{ m} \right] \text{ OR} \\
 & \left[ \sigma_{\text{MPE}} < 1.5^\circ \text{ AND} \right. \\
 & \quad \log \mathcal{L}_{\text{MPE}} / (N_{\text{DOMs}} - 5) < 7.5 \text{ AND} \\
 & \quad \left. \log E_{\text{MuE}} > f_{\text{MuE},40}(\theta_{\text{MPE}}) \right],
 \end{aligned}$$

Without the Earth to use as a filter, muons from cosmic ray showers will overwhelm neutrino-induced muons, except in the case of hard-spectrum neutrino sources which could become discoverable using very high-energy (PeV-EeV) neutrinos. The analysis in the down-going region is set up to choose high-energy, well-reconstructed events. After a tight cut on reconstruction quality, we use a cut on reconstructed event energy to reduce the sample size in the down-going region to roughly the same size as the up-going region. The cut was designed to select a constant number of events as a function of solid angle. The zenith-dependent energy cut is denoted here as  $f_{\text{MuE},40}$ . It is calculated using a polynomial fit to events in  $\cos \theta$ , and can be seen in Figure 6.1. The rate during the year for this data sample can be seen in Figure 6.2.

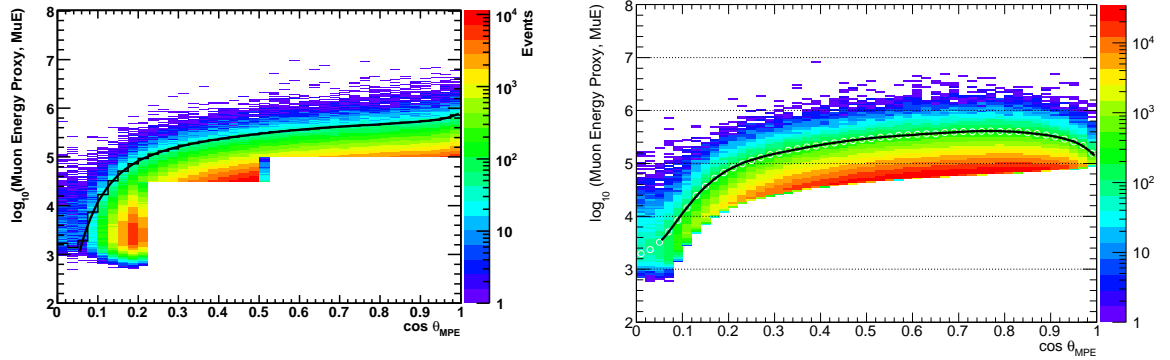


Figure 6.1 Plots illustrating the energy cuts in the down-going region for the 40-string sample (left) and for the 59-string sample which uses the IceTop veto (right).

## 6.2.2 59-string Event Selection

The 59-string event selection utilizes a BDT to select events in the up-going region and utilizes manual quality cuts combined with a veto of the IceTop detector and a final zenith-dependent energy cut to maintain a constant density of events in the down-going region. The final event rate for the 59-string detector can be seen in Figure 6.3. The up-going and down-going regions are described here separately.

### 6.2.2.1 Up-going region of 59 strings

We use the scores from several different BDTs to characterize each event using two signal spectral weights: one for the expected  $E^{-2}$  spectrum for pure Fermi acceleration and one for a softer  $E^{-2.7}$  spectrum observed in Galactic cosmic rays. Two BDTs are trained for each spectral weighting using separate sets of event quality parameters.

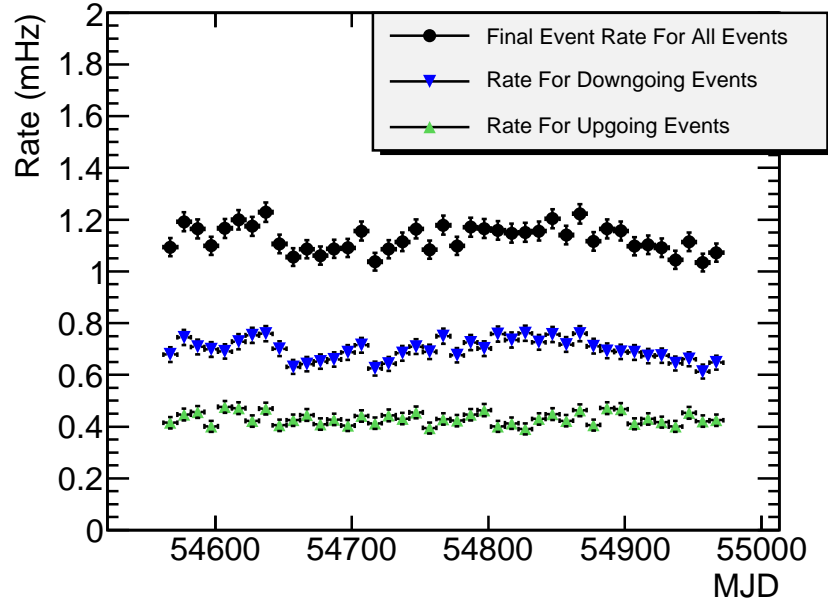


Figure 6.2 A graph of the rate of the final sample of 40-string events, in bins of 10 days. Errors are statistical. Also plotted are the individual rates of up-going and down-going events. The total fluctuation in the final data rate is  $\pm 5\%$  for down-going events and  $\pm \sim 4\%$  for up-going events.

The first BDT (*bdt1*) uses the following quality parameters:

$$\log \mathcal{L}_{\text{MPE}} / (N_{\text{DOMs}} - 2.5)$$

$$\mathcal{L}_{\text{bayes}} - \mathcal{L}_{\text{SPE}}$$

$$\theta_{\text{time-split,min}}$$

$$\theta_{\text{geo-split,min}}$$

$$\mathcal{L}_{\text{bayes,geo-split1}} - \mathcal{L}_{\text{bayes,geo-split2}} - \mathcal{L}_{\text{bayes,SPE}}$$

$$E_{\text{MuE}}$$

$$\theta_{\text{MPE}}$$

$$\sigma_{\text{MPE}}$$



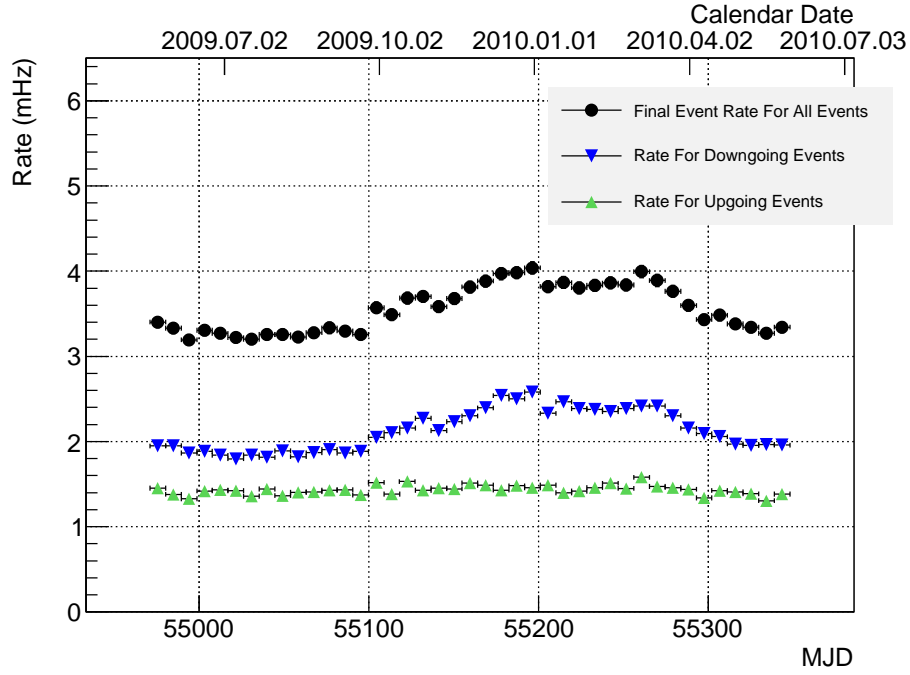


Figure 6.3 A graph of the rate of the final sample of 59-string events, in bins of 10 days. Errors are statistical. Also plotted are the individual rates of up-going and down-going events. The total fluctuation in the final data rate is  $\pm 10\%$  for down-going events and is not noticeable here for up-going events.

Where  $\mathcal{L}_{\text{bayes,geo-split1}}$  and  $\mathcal{L}_{\text{bayes,geo-split1}}$  are the likelihood values of track fits performed in the Bayesian manner with split pulse series. The second (*bdt2*) uses these parameters to separate data and signal:

$$NDir$$

$$\log \mathcal{L}_{\text{MPE}} / (N_{\text{DOMs}} - 5)$$

$$LDir$$

$$|\vec{v}|_{lf}$$

The BDT scores are combined to form two parameters: one for the BDT which uses data and  $E^{-2}$  spectrum signal ( $bdt_{\text{high}}$ ), and one which uses data and  $E^{-2.7}$  spectrum signal ( $bdt_{\text{low}}$ ):

$$bdt_{\text{low}} = (bdt1_{\text{low}} + 1) * (bdt2_{\text{low}} + 1)$$

$$bdt_{\text{high}} = (bdt1_{\text{high}} + 1) * (bdt2_{\text{high}} + 1)$$

The best cut found for the two BDT scores was:

$$bdt_{\text{low}} \geq 1.45 \text{ OR } bdt_{\text{high}} \geq 1.4$$

The distribution of the BDT scores can be seen in Figure 6.4.

### 6.2.2.2 Down-going region of 59 strings

The down-going region uses the same technique as was used in the 40-string sample to select a constant number of events per solid angle for well-reconstructed events. An additional tool was used in the vertically down-going region: the use of IceTop as a veto for cosmic ray air showers. Hits in IceTop tanks were used to reject events where the detector saw two or more hits in IceTop that were compatible with being from an air shower with the same directionality and timing as the reconstructed muon track inside the glacier. Additional cuts of  $\log \mathcal{L}_{\text{MPE}} / (N_{\text{DOMs}} - 5) < 7.4$  and  $\sigma_{\text{MPE}} < 1.5^\circ$  were used to select only very high-quality tracks.

We find that this veto rejects 99% of air showers which are vertically down-going (see Figure 6.5, and Figure 6.6 for an example vetoed event), thus reducing the energy cut which is required to obtain a constant event rate per solid angle. This reduction is found to significantly improve the sensitivity to  $E^{-2}$  spectrum sources for angles close to vertically downgoing. The energy cut is shown in Figure 6.1.

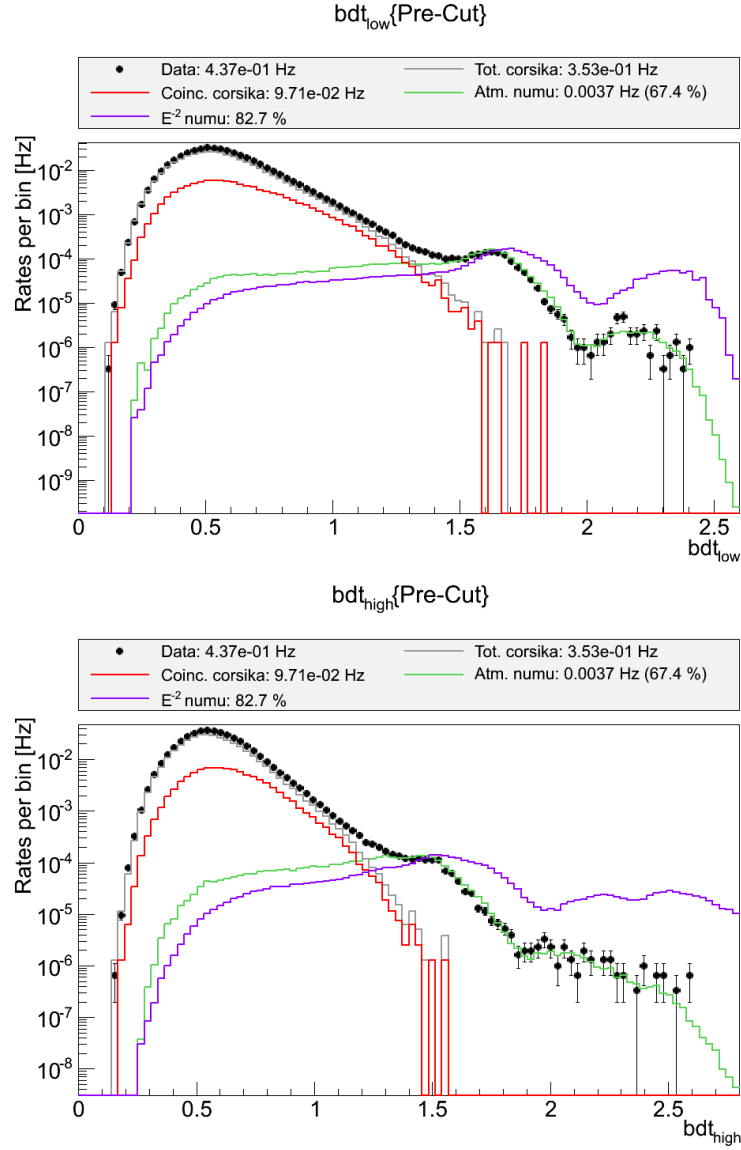


Figure 6.4 Graphs of the BDT scores of events, with the top graph showing the score trained using an  $E^{-2.7}$  spectrum, and the bottom showing the score of the tree trained on an  $E^{-2}$  spectrum. Data are plotted as black dots, while signal and background simulations (labeled as numu and corsika, respectively) are drawn as lines for comparison.

	59 Strings	40 Strings
Total Events	107,569	36,900
Up-going	43,339	14,121
Down-going	64,230	22,779
Livetime (d)	348.138	375.539

Table 6.1 Summary of the final event selections with the 40 and 59-string configurations.

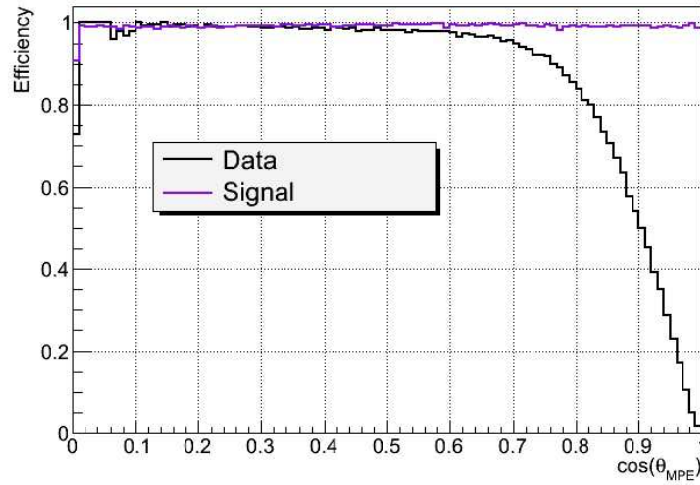


Figure 6.5 A plot of the efficiency of data and signal of the IceTop veto as a function of zenith angle ( $\cos(1)$  is directly down-going).

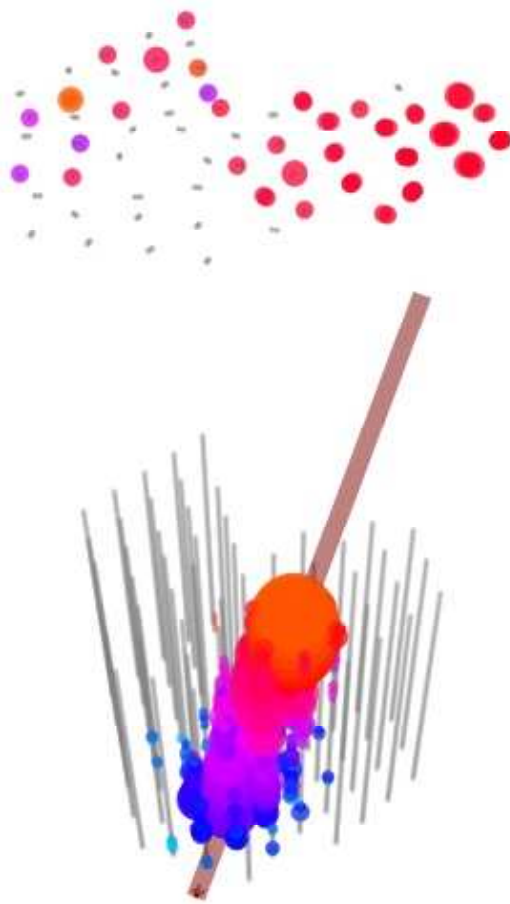


Figure 6.6 An example of an event vetoed by the IceTop array. There is an obvious air shower signature in the surface array, which is a sign of an electromagnetic shower due to a cosmic ray interaction. Muon neutrinos in the down-going region will produce a single muon, which will not have an extensive air shower signature.

## Chapter 7

### Analysis Method

In this chapter we describe the method of analyzing and giving a statistical significance to searches. The unbinned maximum likelihood method is described along with the various probability density functions (PDFs) used to model the data as a mixture of signal and background. The method allows for the use of several different distributions. Here, information about the spatial distribution of events, the spectral distribution, and also the distribution of the events in time are all used to enhance searches for neutrino point sources. The methods of calculating upper limits and discovery potentials are also described.

#### 7.1 Maximum Likelihood Method

The unbinned maximum likelihood searches performed here are based on the method described in [123] and extended to searches for time-dependent behavior in [124]. In this likelihood ratio method, a combination of signal and background populations is used to model the data. For a data set with  $N$  total events, where  $n_s$  is the number of events in the signal population, the probability density of the  $i^{th}$  event is given by:

$$\frac{n_s}{N} \mathcal{S}_i + \left(1 - \frac{n_s}{N}\right) \mathcal{B}_i. \quad (7.1)$$

where  $\mathcal{B}_i$  is the background PDF and  $\mathcal{S}_i$  is the signal PDF. The likelihood  $\mathcal{L}$  of the data given the value of  $n_s$  is the product of the individual event probabilities:

$$\mathcal{L}(n_s) = \prod_{i=1}^N \left[ \frac{n_s}{N} \mathcal{S}_i + \left(1 - \frac{n_s}{N}\right) \mathcal{B}_i \right]. \quad (7.2)$$

This likelihood is maximized with respect to  $n_s$  and any other nuisance parameters which are a part of the signal hypothesis. The maximization provides the best-fit values of these parameters.

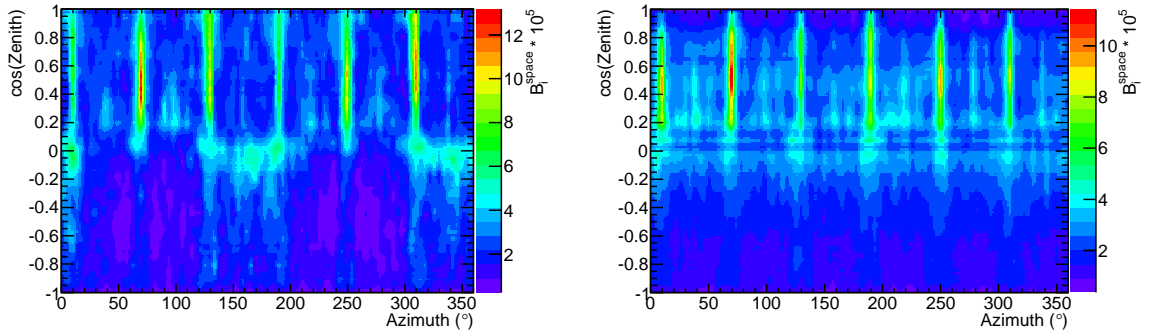


Figure 7.1 Left: The normalized event distribution of the 36,900 events in local coordinates for the 40-string data (the space term in Equation 7.3). There are two predominant effects: for up-going events (northern sky, bottom half), events traveling down the longer end of the detector are more likely to trigger and pass cuts; for down-going events (southern sky, top half), there are six peaks in the event rate. This is due to the initial filter conditions at the South Pole that select tracks more efficiently when they pass close to aligned strings. Right: The same distribution for the 107,569 events selected for the 59-string sample. The two peaks for up-going events traveling down the long end of the 40-string detector are gone.

The background PDF,  $\mathcal{B}_i$ , is given by:

$$\mathcal{B}_i = B_i^{\text{space}}(\theta_i, \phi_i) B_i^{\text{energy}}(E_i, \theta_i) B_i^{\text{time}}(t_i, \theta_i), \quad (7.3)$$

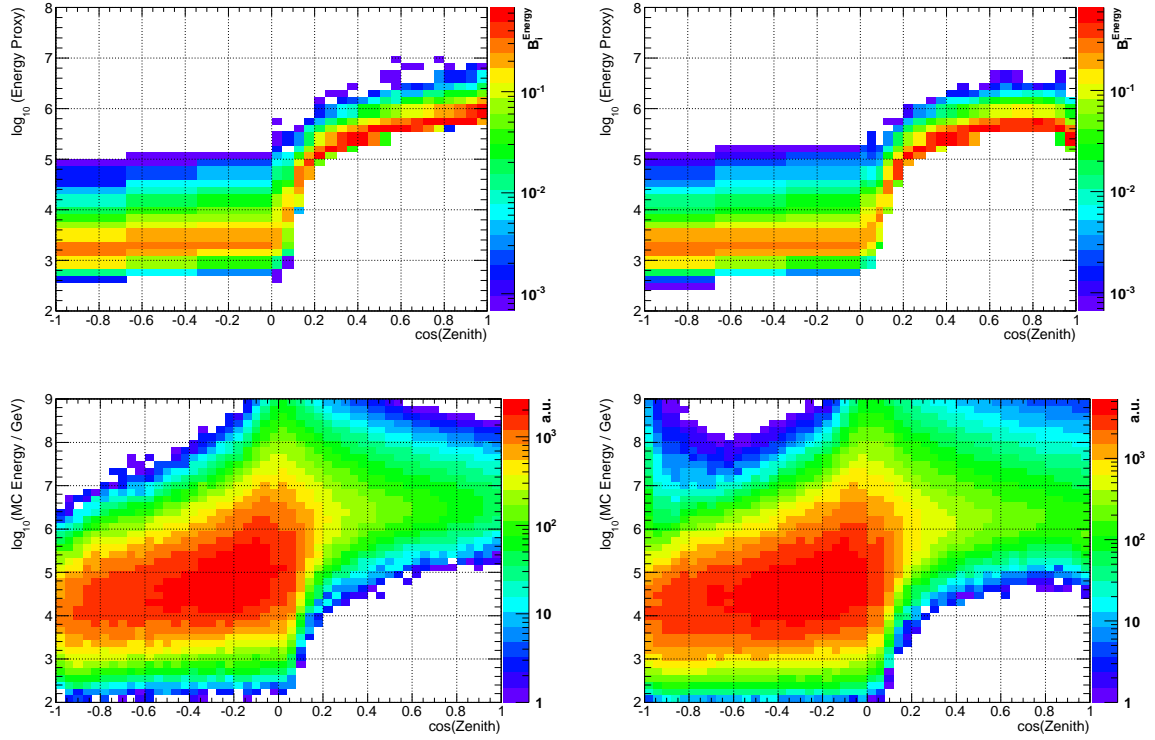


Figure 7.2 Above right: Normalized distribution of cosine of zenith for data as a function of the energy proxy  $E_{MuE}$  (the energy term in Equation 7.3) for the 40-string data. Above left: Same as above right but using the 59-string data. Lower right: The distribution (in arbitrary units) of the energy proxy  $E_{MuE}$  for an  $E^{-2}$  spectrum source with a constant flux normalization for the 40-string data. IceCube is more sensitive to an  $E^{-2}$  for declinations slightly into the Northern Hemisphere, as can be seen in the relatively high acceptance here. Lower left: Same as lower right but using the 59-string selection.

and is computed using the distribution of data itself. The spatial term  $B_i^{\text{space}}(\theta_i, \phi_i)$  is the event density per unit solid angle as a function of the local coordinates, shown in Figure 7.1. The energy probability,  $B_i^{\text{energy}}(E_i, \theta_i)$ , is determined from the energy proxy distribution of data as a function of the cosine of the zenith angle  $\cos \theta_i$  (see Figure 7.2). The energy cut for



the southern sky sample decreases for larger zenith angles, creating a strong zenith dependence of the energy in the southern sky as can be seen in Figure 7.2 (right). Note that for the northern sky the energy dependence on zenith is small. The time probability  $B_i^{\text{time}}(t_i, \theta_i)$  of the background is taken to be flat, because the expected seasonal modulations are less than  $\pm 10\%$  and depend on the zenith angle, which is negligible compared to Poissonian fluctuations of small number of signal events expected.

The signal PDF  $S_i$  is given by:

$$S_i = S_i^{\text{space}}(|\vec{x}_i - \vec{x}_s|, \sigma_i) S_i^{\text{energy}}(E_i, \theta_i, \gamma_s) S_i^{\text{time}}, \quad (7.4)$$

where  $S_i^{\text{space}}$  depends on the angular uncertainty of the event  $\sigma_i$  and the angular difference between the event coordinate  $\vec{x}_i$  and the source coordinate  $\vec{x}_s$ . It is modeled as a two-dimensional Gaussian function:

$$S_i^{\text{space}}(|\vec{x}_i - \vec{x}_s|, \sigma_i) = \frac{1}{2\pi\sigma_i^2} e^{-\frac{|\vec{x}_i - \vec{x}_s|^2}{2\sigma_i^2}}. \quad (7.5)$$

$S_i^{\text{energy}}$  is a function of the reconstructed energy proxy  $E_i$ , and the fit spectral index  $\gamma_s$  is calculated from an energy distribution of simulated signal in a zenith band that contains the event.  $S_i^{\text{time}}$ , the signal time probability, depends on the particular signal hypothesis, which is different in each search we have performed. For each search, signal is injected with the same functional form (Gaussian, box or light curve) in time as is being tested.

The test statistic ( $TS$ ) is calculated from the likelihood ratio of the background-only (null) hypothesis over the signal-plus-background hypothesis:

$$TS = -2 \log \left( \frac{\mathcal{L}(n_s = 0)}{\mathcal{L}(\hat{n}_s, \hat{\gamma}_s, \hat{T}_s)} \right). \quad (7.6)$$

The test statistic is expressed as in Equation 7.6 such that it will distribute as a chi-square

function with the number of degrees of freedom equal to the number of fit parameters. By maximizing  $TS$  the best fit parameters  $\hat{n}_s, \hat{\gamma}_s$  and any fit time parameters  $\hat{T}_s$  are obtained.

Larger values of  $TS$  are less compatible with the null hypothesis, and indicate its rejection at a confidence level equal to the fraction of the scrambled trials above the  $TS$  value found in the data. Data scrambling is done by assigning a random time to each event from a period of active data taking and performing the proper coordinate transformation to get a new right ascension and declination. The fraction of scrambled trials resulting in a value above the  $TS$  value obtained from data is referred to as the “ $p$ -value”.

## 7.2 Event Weight

The method returns a value for the signal fraction for a set of best-fit signal parameters, but in an unbinned method there is not a clear-cut way of defining particular events as signal-like or background-like, as would be done by selecting a signal region in a binned analysis. A useful parameter to describe individual events is the ratio of  $\mathcal{S}_i/\mathcal{B}_i$  given the set of parameters of the tested location and spectral index. The spectral index is used in two ways: first as the best-fit spectral index for all events and before the best spectral index is found, and also using the spectrum which will maximize the signal weight for a given event. This is used to determine the most signal-like events for purposes of calculating a first-guess set of parameters in searches.

In Figure 7.3 and 7.4, the dependence of the energy weight in the signal term can be seen for events with declination of  $16^\circ$ , which uses the events between  $0^\circ$  and  $20^\circ$  to model the background. The value of the spectral index giving the best energy weight is highlighted by a dashed black line. In Figure 7.5, we see the dependence on the spatial event weight as a function of the space angle of the event from the tested location (here at locations of RA,

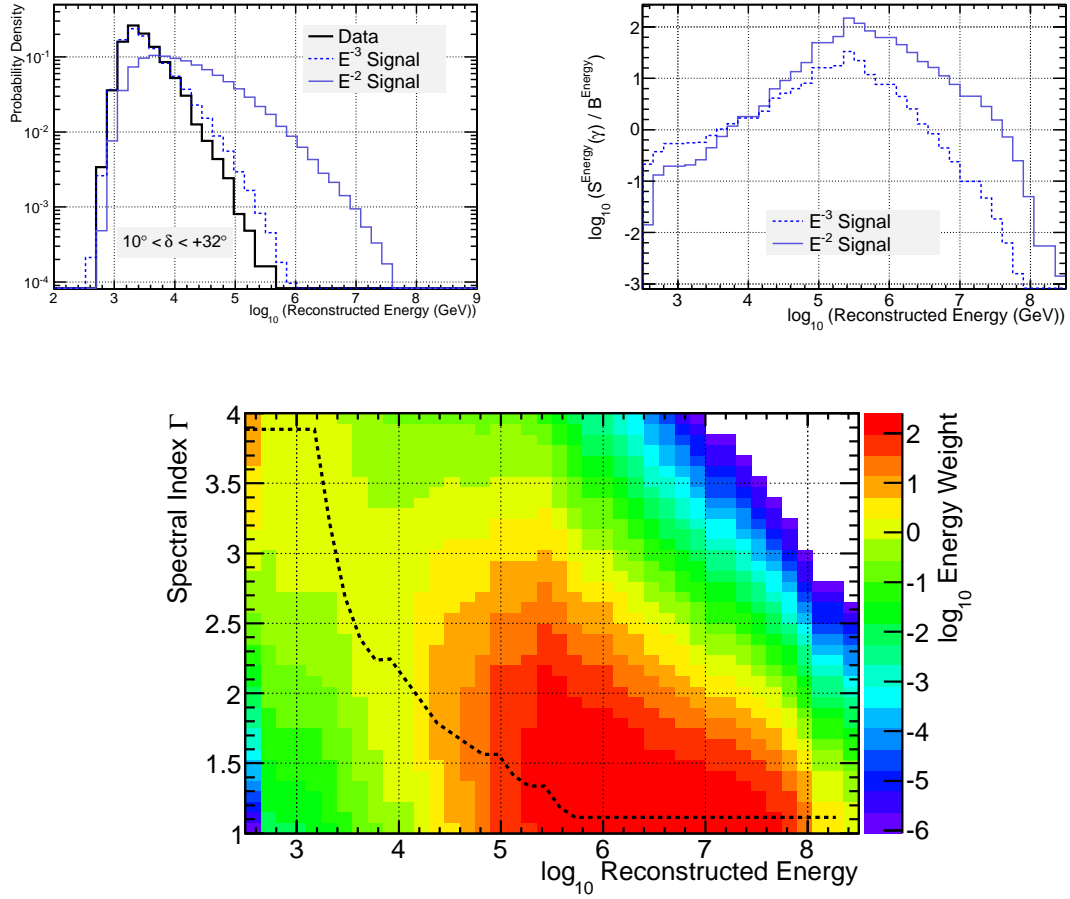


Figure 7.3 Top left: The normalized reconstructed energy distribution for the 40-string data sample and two spectra of simulated signal. The distributions are for events between  $+10$  and  $+32^\circ$  in declination. Top right: The ratios of the normalized reconstructed energy distributions for signal divided by data. This provides the ratio  $S_i^{\text{energy}}(E_i, \theta_i, \gamma_s) / B_i^{\text{energy}}(E_i, \theta_i)$  for a given declination band, reconstructed event energy  $E_i$ , and signal energy spectrum  $\gamma_s$ . To account for empty bins in the data distribution, one event is placed in the highest energy bin and distributed evenly across all previous empty bins. Bottom: The plot on the top right is expanded to include signal spectra from  $1 \leq \gamma_s \leq 4$ , with the ratio expressed as a color scale. The dashed line indicates the spectral index which maximizes the ratio for a given reconstructed energy.

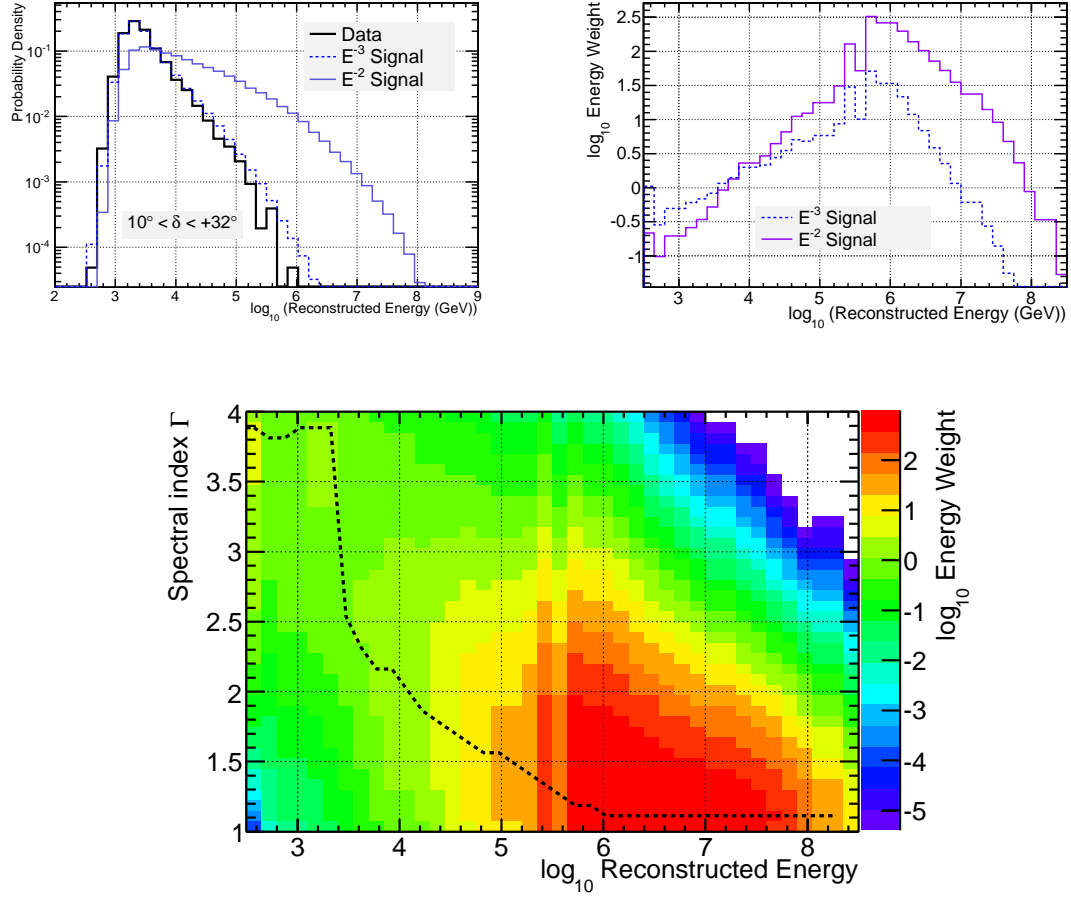


Figure 7.4 Presented here are the energy PDFs and weights in the same scheme as Figure 7.3 for events between  $+10$  and  $+32^\circ$  in declination, using the 59-string data sample instead of the 40-string sample.

dec of  $343.5^\circ$ ,  $+16.2^\circ$  and  $74.3^\circ$ ,  $-23.4^\circ$ ), calculated from an average of 10,000 scrambled maps. What we see from this distribution is that no event less than  $1^\circ$  from the tested northern sky location has a  $\mathcal{S}_i/\mathcal{B}_i$  of less than  $\sim 1000$ , and the same for the southern sky events less than  $0.5^\circ$  from the tested location. The shape of the distribution is parabolic, as is to be expected because the signal PDFs of events are modeled as two-dimensional Gaussian functions. Because the angular uncertainty is calculated on an event-by-event basis, we see a superposition of many Gaussians here.

A ratio of  $\mathcal{S}_i/\mathcal{B}_i$  of one is used as a nominal cutoff where events go from being nominally signal-like to nominally background-like. It is interesting to note that events which are nominally signal-like can come from up to  $12^\circ$  distance from the tested location.

From the energy distribution, we see that there is a broad area of events with less than roughly 13 TeV in energy and that fit spectral indices softer than  $E^{-3}$ , where the energy ratio is roughly one. The addition of the energy term does not assist in distinguishing signal from atmospheric background compared to an analysis which does not use any energy weighting.

### 7.2.1 Local Coordinate Dependence

Due to the requirements for triggering and filtering, the cuts applied, Earth absorption properties, and detector geometry, the final sample of events is not uniform in the detector local coordinates zenith ( $\theta$ ), and azimuth ( $\phi$ ). For time-integrated point-source searches, the azimuth dependence is usually neglected because it is smoothed in right ascension by the rotation of the Earth over long integration times. However, in a time-dependent analysis the azimuth dependence becomes important for time scales shorter than one day. The local coordinate (zenith and azimuth) distribution of 40 and 59-string data is shown in Figure 7.1. In the northern sky there is the effect that events traveling along the longer axis of the 40-

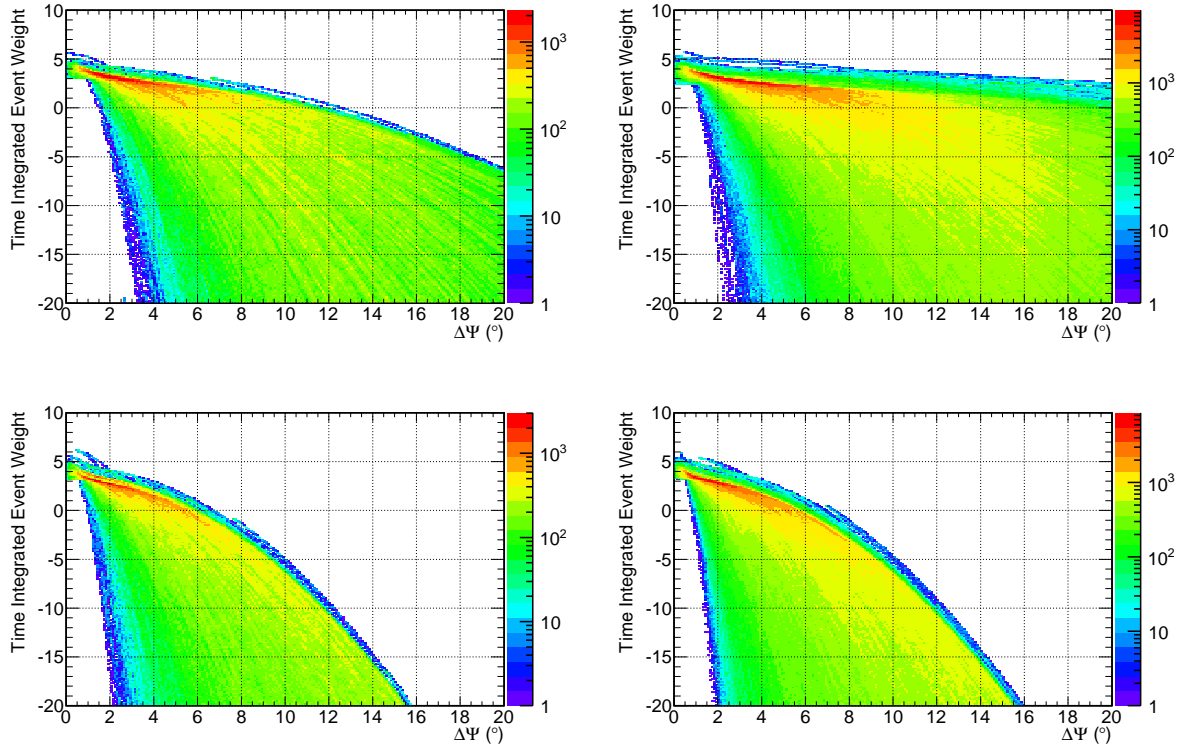


Figure 7.5 The event weight  $\log_{10}(S_i/B_i)$  plotted as a function of the angular separation from the source location ( $\Delta\Psi$ ). Two source locations are used, with a right ascension and declination of  $343.5^\circ, +16.2^\circ$  (top row) and  $74.2^\circ, -23.4^\circ$  (bottom row), for the 40 and 59-string datasets (left and right columns, respectively). The energy weight used is the maximum for each event, following the line in Figures 7.3 and 7.4. For both datasets the sample in the southern sky has a tighter cut on the angular error, so the weight falls off faster than in the Northern sky.

string (see Chapter 4) detector have a longer lever arm and are more likely to trigger the detector and be well-reconstructed. In the southern sky, there is a selection criterion on the integrated charge seen in all DOMs as part of the online muon filter. This gives a preference to events which pass near a line of strings, yielding a six-fold peak in rates corresponding

to the main axes of the detector symmetry. The effect of the growth of the detector from 40 to 59 strings can be seen in the top right of Figure 7.1; the horizontal preference for well-reconstructed events is gone. The six-fold symmetry remains due to the charge cut, and can also be seen much less strongly in the up-going region. This is due to events along these axes being slightly more well reconstructed because they typically have more hits compared to other events of similar energy, which is because they pass near a greater number of DOMs.

### 7.3 Combining Datasets

Unbinned likelihood methods are ideal for combining data sets. Each event carries its own PDF and background can be estimated for each sample. The overall likelihood is maximized for the combined data sets, assuming a uniform signal hypothesis. The event-wise PDF now depends on the particular data set of which the  $i$ th event is a part:

$$P_i = \frac{n_s^j}{n_{\text{tot}}^j} S_i^j + \left(1 - \frac{n_s^j}{n_{\text{tot}}^j}\right) B_i^j, \quad (7.7)$$

where the index  $j$  refers to the specific dataset from which the event came. In our case, it can take on values  $j = \{\text{IC40}, \text{IC59}\}$ . That is,  $n_{\text{tot}}^j$  is the total number of events in the  $j$ th data set,  $B_i^j$  is the background PDF of the for the  $j$ th data set, etc.

The likelihood is again the product of  $P_i$  over all events in each data set. The likelihood is maximized globally, assuming the same signal hypothesis (neutrino flux) in all data sets. Therefore,  $\gamma = \gamma^{\text{IC40}} = \gamma^{\text{IC59}}$ . In general, the number of signal events is not the same in all data sets, but depends on the live time, detector acceptance, and cut efficiency of each data set. Simulation is used to determine the fraction of the total number of signal events in each data set  $f^j = f^j(\gamma)$ , so that  $n_s = f^j n_s^j$ . The total number of signal events is given by:

$$n_s = \sum_j n_s^j. \quad (7.8)$$

In this way, our likelihood remains a function of the same number of parameters. The maximization of the likelihood is again done by finding the best estimate of  $n_s$  and  $\gamma$  along with any time-dependent features, now the total number of signal events in all data sets and the uniform spectral index and time hypothesis, respectively.

## 7.4 Sensitivity and Discovery Potential

Aside from the  $p$ -values from searches, in the absence of a signal upper limits can be provided. The discovery potential is defined as the average number of signal events required to achieve a  $p$ -value less than  $2.87 \times 10^{-7}$  (one-sided  $5\sigma$ ) in 50% of trials. Similarly, the sensitivity is defined as the average signal required to obtain a  $p$ -value less than that of the median of the test statistic distribution of scrambled (background-only) samples in 90% of trials. The upper limit is the average signal required to be injected to obtain a  $p$ -value less than that seen in the data. Sample test statistics for background and injected signal can be seen in Figure 7.6. The time-integrated limits from the 40-string, 59-string, and combined samples can be seen in Figure 7.7.

Upper limits on the average muon neutrino flux normalization are natural expressions for time-independent searches, because no time dependence is assumed. For time-variable sources we can place limits on the muon neutrino fluence normalization from a source, defined as the integral in time of the flux upper limit:

$$f = \int_{t_{\min}}^{t_{\max}} \Phi_0 \times dt = \Delta t \Phi_0 , \quad (7.9)$$

where  $\Phi_0$  is the time-independent upper limit on the normalization on an  $E^{-2}$  spectrum and  $t_{\max}$  and  $t_{\min}$  are the nominal limits on neutrino emission. Here the emission is modeled as a simple on-off function. There is a correspondence between the fluence and the average



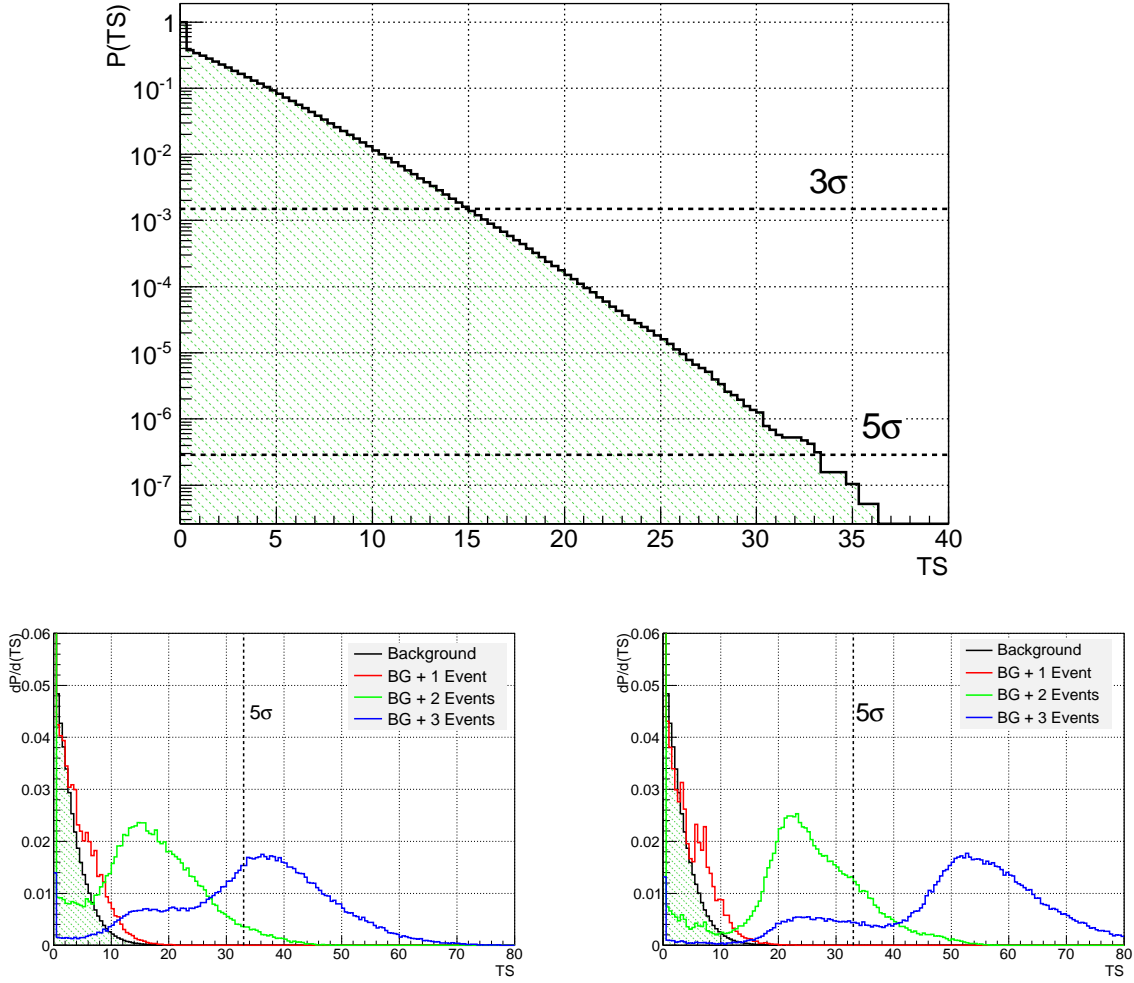


Figure 7.6 Integral distribution of the null test statistic distribution at  $\delta = +16.1^\circ$  with  $3\sigma$  and  $5\sigma$  thresholds indicated (top) following the untriggered search method described in Chapter 9. Below are the distributions of the test statistic for background and 1, 2 and 3 added signal events with a flare width of 15 minutes (bottom left) and 1, 2 and 3 added signal events with a flare width of 10 seconds (bottom right).

number of events detected, shown as a function of the declination in Figure 7.8. The limits are calculated according to the classical (frequentist) construction of upper limits outlined

by Neyman [125]. The systematic error of 16% is neglected in all upper limits because the limits are dominated by statistical fluctuations for flares. The analysis in Chapter 11 uses the ordering method of Feldman and Cousins [126] to calculate upper limits and the systematic errors. It is found that using the Feldman-Cousins implementation to calculate upper limits yields results 15% higher than using the Neyman method. The 16% systematic errors add roughly 3% to the limits calculated, because the number of events is typically near the statistical minimum.

When considering equal fluxes of muon and tau neutrinos at the Earth, the resulting upper limits on the sum of both fluxes are about a factor of 1.7 times higher than if only muon neutrinos are considered. This differs from the expected factor of two due to oscillation if no tau neutrinos would be detectable [27]. For an  $E^{-2}$  spectrum of the signal neutrino flux the contribution due to the detectable tau neutrino flux for sources at the horizon is 10% and up to 15% for sources in the Northern Hemisphere. This is due to the tau decay channel into muons with a branching ratio of 17.7% and in part to the tau leptons with energy greater than some PeVs that may travel far enough to be reconstructed as tracks in IceCube before decaying. In the up-going region we have considered tau regeneration in the Earth.

## 7.5 Systematic Errors

Point-source analyses in IceCube use scrambled data to model the background. This means analyses yield reliable results in terms of the average number of events from a given spectrum which are required for upper limits. There are systematic uncertainties in translating from a number of events to a flux or a fluence, however. These systematic uncertainties on the conversion from neutrino event to neutrino flux come mainly from the absolute DOM efficiency, propagation of photons in ice, and effects from the neutrino cross-section and

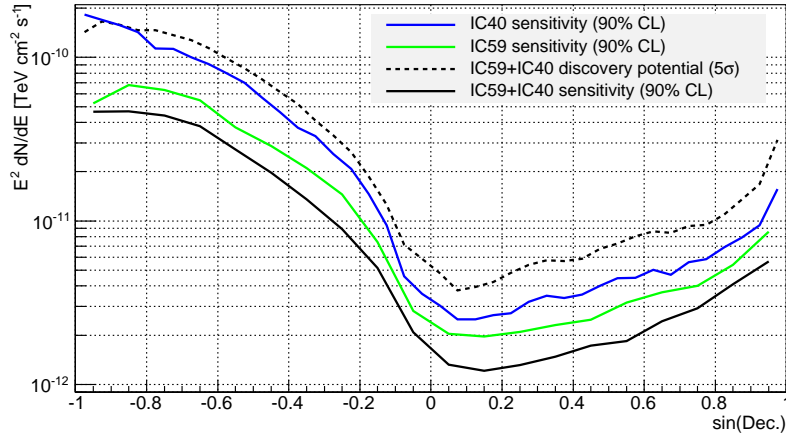


Figure 7.7 The time-integrated sensitivities to an  $E^{-2}$  spectrum muon neutrino signal plotted against declination for the 40 and 59-string configurations. The sensitivity and discovery potential are also plotted for the combined dataset.

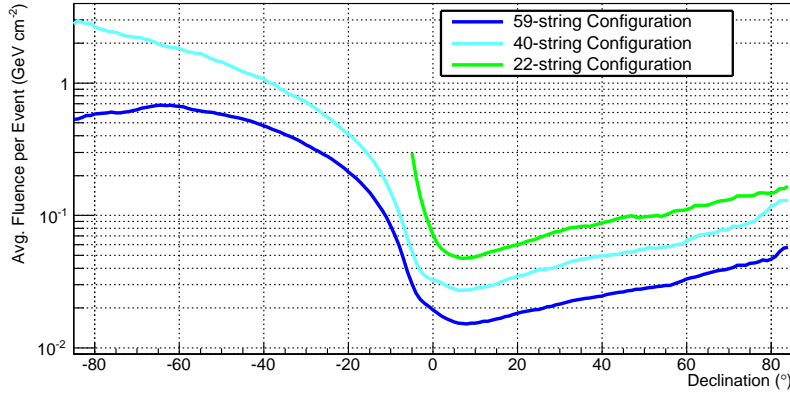


Figure 7.8 The normalization per event on the fluence as expressed in Equation 7.9 from an  $E^{-2}$  spectrum muon neutrino signal in a declination band, divided by the number of events in the band in the 22, 40 and 59-string configurations, plotted against declination.

muon energy loss in the ice (see Table 7.1).

The overall systematic error is estimated by simulating signal with different proper-

Error source	Source error	Resulting error in signal efficiency
Ice properties	$\pm 10\%$	11%
DOM sensitivity	$\pm 8\%$	9%
Cross sections, $E$ -loss	$\pm 8\%$	8%
Sum in quadrature		16%

Table 7.1 Summary of systematic errors for  $E^{-2}$  neutrino sources.

ties; resulting in more or less scattering and absorption in the ice and altering the PMT efficiency up and down. These datasets are used to estimate the change in event rate using the same cuts used for the analysis.

The systematic error is applied using the method outlined in [127], with a modification from [128]. The limit is calculated using a frequentist approach, which obtains the limit in terms of the mean number of expected events. The error is treated as a nuisance parameter with a Gaussian mean and width and is integrated over as a nuisance parameter. The upper limits for IceCube point-source searches are generally only 3–4 events, the statistical uncertainty is typically much larger than the 16% errors derived from the systematic errors. The typical increase in the limits is only approximately 3% on average after including systematic errors.

## Chapter 8

### Simulation and Detector Performance

This chapter describes the simulation of neutrinos and cosmic ray air showers used to model the signal and background for the IceCube detector. This includes simulation of cosmic ray showers for background estimation and neutrino generation for signal simulation. Computer programs are used to propagate cosmic ray air showers to the ground, neutrinos through the Earth, and charged leptons through the ice along with emitted light and secondary particles. The light is tracked to the DOMs where the PMT and electronics are simulated. At that point the simulation is in the same form of the IceCube DAQ and it is processed identically as the data.

To within the uncertainty on our simulation models, distributions of parameters used in event selection agree in data and simulation. Simulation also allows us to test the resolution of our detector and efficiency of the cuts used in point-source searches. It is also used to characterize the effectiveness of the reconstructions in terms of the angular error in a track reconstruction or in the energy reconstruction resolution.

The probabilities of point-source searches are computed using only data, but a physical interpretation of the results require the use of Monte Carlo simulation. This includes understanding the efficiency of the trigger, filters and quality cuts to obtain the final data

sample, also calculating upper limits and discovery potentials of the search methods.

## 8.1 Simulation Chain

### 8.1.1 Neutrino Simulation

Neutrinos are simulated on the ANIS (All Neutrino Interaction Simulation) program [129], the cross-sections for deep inelastic neutrino-nucleon interactions use the parton distribution functions from CTEQ5 [130]. Simulation begins at the surface of the Earth, with the neutrino propagated through the planet toward the South Pole. This takes into account energy loss due to NC interactions, and absorption and regeneration due to CC interactions. Once in the vicinity of the IceCube detector, all unabsorbed neutrinos are forced to interact – muon neutrinos can interact at a location such that the daughter muon is within range of detector. All events are given a weight to represent the probability of the simulated interaction.

Standard neutrino simulation used here generates events from 100 GeV to 10 EeV with an  $E^{-1}$  spectrum, which is then reweighted according to the desired signal spectrum. This is done to ensure that there is sufficient statistics for high energy events. Other neutrino simulation uses an  $E^{-2}$  spectrum, which has better statistics in the energy range of 1-10 TeV, the energy range of the bulk of atmospheric neutrinos seen by IceCube.

### 8.1.2 Cosmic Ray Simulation

Atmospheric muons from cosmic ray air showers are simulated using the CORSIKA (COsmic Ray SIMulations for KAscade) program [131] using the SIBYLL hadronic interaction model [132]. Because the rates can vary over the year due to temperature and

density changes in the stratosphere, where initial cosmic ray interactions typically occur, four months from different seasons are simulated to account for these temperature variations. The atmospheric muon background is generated to test the efficiency of cuts and to estimate the contamination for the final muon sample.

### 8.1.3 Propagation

Charged leptons are propagated through ice and rock by the Muon Monte Carlo (MMC) program [133]. This simulates the energy losses due to ionization, pair production, and stochastic losses from bremsstrahlung. The number of Čerenkov photons from the muon and any secondary showers along the track are also calculated.

Photons in the ice are handled with the Photonics software [134], which is designed to use the measured ice properties to guide propagation using the scattering and absorption at different points in the ice. Tables with the photon amplitudes and timing distributions are pre-calculated for grid points in the simulated volume, which makes the simulation memory-consuming but greatly speeds up the calculation of the detector response.

### 8.1.4 Detector Simulation

Once photons intercept a DOM in the Photonics package, they are then given to another package to simulate the PMT response, based on waveform calibration done on DOMs before deployment. The hits are produced by a program simulating the PMT discriminator, digitization of the waveform, and the local coincidence condition from neighboring simulated DOMs. The trigger conditions applied to simulation are the same as those run online.

The live time of the background simulation is typically less than the live time of the data due to computational constraints. For the 40 and 59-string configurations, the data

live time is roughly one year, while the simulation of cosmic ray events is roughly two weeks. Simulation datasets with harder spectrum than that measured of cosmic rays receive a different weighting, and have live times at high energies significantly longer than one year. Comparisons of data to Monte Carlo are important to determine the modeling of ice and determining of analysis cuts. Comparisons between data and Monte Carlo of the up-going 59-string analysis sample in a number of important quality parameters are shown in figure 8.1.

## 8.2 Detector Performance

The knowledge of the true direction and energy of the particles injected with simulation allows us to test the performance of the detector for point-source analyses. This requires us to have a good idea of the accuracy of the reconstructions along with the ability of the filter and event selection chain to detect neutrinos of different energies.

### 8.2.1 Neutrino Point Spread Function

We use the point spread function (PSF) to characterize the pointing ability of the detector, which is essential for point-source searches. It uses the angle ( $\Delta\Psi$ ) between the reconstructed muon track and the direction of the neutrino primary to determine the spatial spread of events from a simulated neutrino point source. The resolution of a data sample is typically defined as the angle for which 50% of neutrinos are reconstructed within the true direction. The PSF for the up-going regions of both the 40 and 59-string detectors can be found in Figure 8.2.



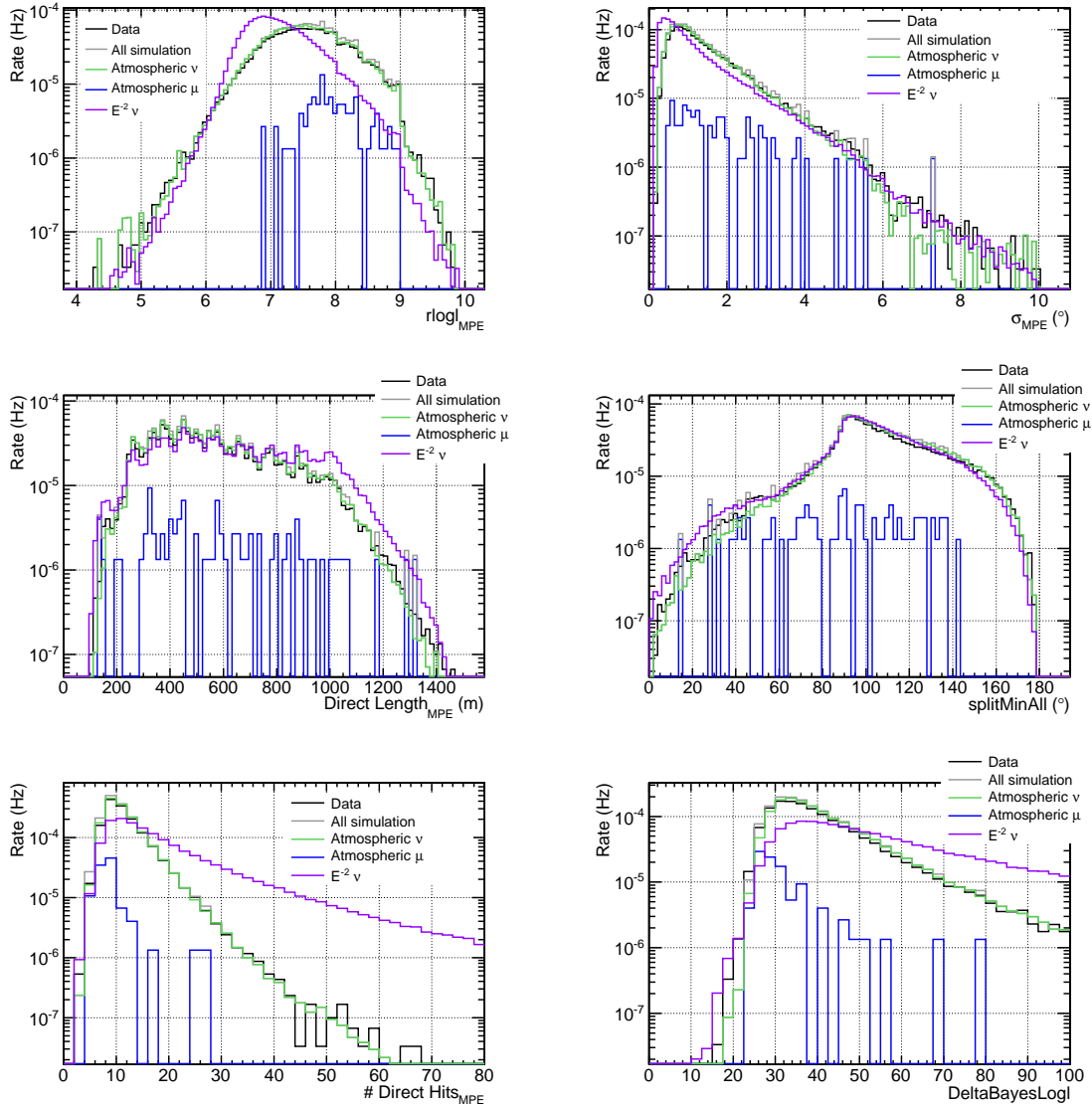


Figure 8.1 Data-to-Monte-Carlo comparisons using the up-going point-source sample from the 59 string configuration. Data is in black, the atmospheric neutrino distributions using the Bartol flux [135] is in green, while the contribution from atmospheric muons is in blue. The sum of all atmospheric simulation is gray, and the expected distribution for neutrinos with an  $E^{-2}$  spectrum is in purple, with the normalization set to match that for atmospheric neutrinos.

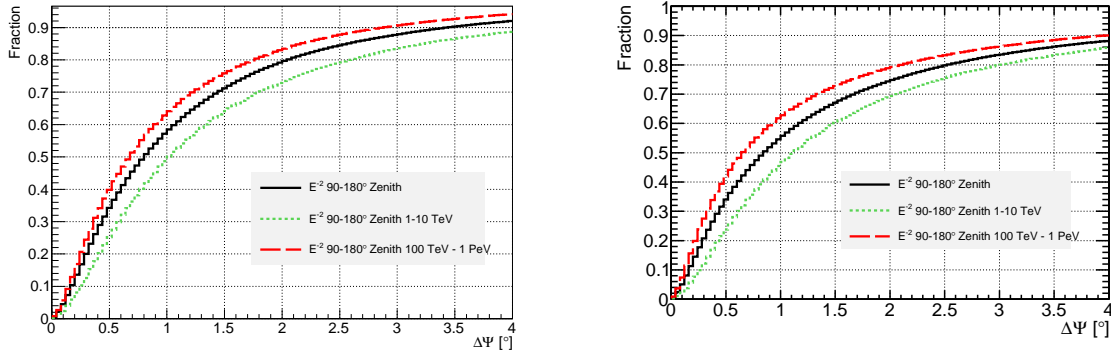


Figure 8.2 The cumulative point spread functions (angle between neutrino and reconstructed muon track) for simulated neutrino signal events following a spectrum  $d\Phi/dE \propto E^{-2}$  at analysis level in the up-going region for the 40-string (left) and 59-string (right) event selections.

### 8.2.2 Neutrino Effective Area

The neutrino effective area is a useful parameter to compare different event selections across different energy ranges. It represents the size of a detector equivalent to IceCube which would be 100% efficient at detecting neutrinos passing through. We can also use the neutrino effective area at a particular declination  $\delta$  to estimate the neutrino event rate for differential flux  $d\Phi/dE$ :

$$N_{\text{events}}(\delta) = \int dE A_{\nu}^{\text{eff}}(E_{\nu}, \delta) \frac{d\Phi_{\nu}(E_{\nu}, \delta)}{dE_{\nu}} \quad (8.1)$$

The effective areas for the 40 and 59-string event samples are shown in Figure 8.3 for different declination bands. The highest energy neutrinos are more often absorbed as they travel through the bulk of the Earth, which can be seen here. The effect of the energy cuts can be seen in the down-going region.

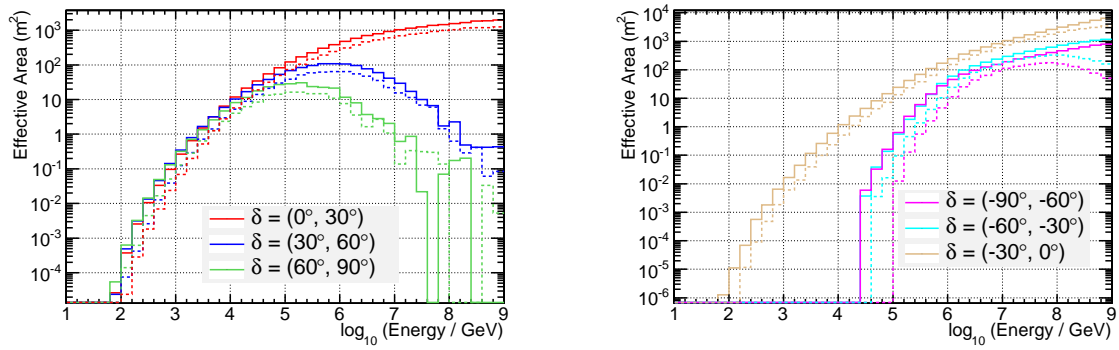


Figure 8.3 The muon neutrino effective areas for the 40 and 59-string point-source samples. Up-going declination bands are shown on the left, down-going declinations on the right. Bands are plotted in the same color for the 40 and 59-string samples, the 40-string effective area is dashed, while the 59-string sample is solid.

## Chapter 9

### All-Sky Time-Scan

In this chapter we present the most general of the searches, which is designed to search over the entire sky and live time for a clustering of events in time and space. The improvement in discovery potential and the method of reliably finding the most significant flare are described, and results are presented. The output of the analysis is any significant clustering in time and space for the period covered by the analysis, which searches for point sources of flaring emission from time scales from  $20 \mu\text{s}$  (the minimum time between events in the 40 and 59-string samples) to an entire year (or the duration of data used for analysis). The search is applied separately to the 40 and 59-string samples. The sensitivity of a flaring analysis is also time-dependent, so the sensitivity for a specific time covered by one sample is not improved by adding data from another period.

While a time-independent search has the best sensitivity to steady sources, a source which has emitted neutrinos for only a limited period of time might not be detected. The time-dependent analysis here scans for a significant excess with respect to background over all time scales (from sub-seconds to the full year) at each direction of the sky. For flares shorter than  $\sim 100$  days, the discovery potential of the time-dependent search typically becomes better than the time-integrated one, and in principle a short burst can be discovered

with only two events if they occur close enough together in time. The advantage of such untriggered searches is their ability to cover all emission scenarios, including neutrino emission without any observed counterpart in the electromagnetic spectrum.

## 9.1 Method and Expected Performance

We have adapted the method from [124] for this search to a real detector with non-uniform acceptance and deadtime. The non-uniform acceptance can be seen in Figure 7.1, deadtime compensation is shown below in Figure 9.2. The time-dependent probability density function from Equation 7.4 for this search is a Gaussian function:

$$S_i^{\text{time}} = \frac{1}{\sqrt{2\pi}\sigma_T} \exp\left(-\frac{(t_i - T_o)^2}{2\sigma_T^2}\right) \quad (9.1)$$

where  $t_i$  is the arrival time of the event, and fit parameters  $T_o$  and  $\sigma_T$  are the mean and sigma of the Gaussian describing flaring behavior in time. The maximization of the test statistic returns the best-fit values of the Gaussian mean (the time at which the flare peaks) and sigma (corresponding to the duration of the flare). Both the background and expected number of events are small, so distinguishing a box-type function from a Gaussian would require many more events than required for a  $5\sigma$  discovery, and we find that using either of these flare hypotheses performs similarly. It was found that the fitting method used in this section worked better with a continuous function, so a Gaussian functional form was chosen.

There are many more uncorrelated time windows for short time flares than large ones, giving a preference to find shorter flares. The test statistic formula of Equation 7.6 is modified to include a weighting term to correct for this effective trial factor and avoid undue preference for short flares using a Bayesian approach [124]. The weighted likelihood will

be:

$$\mathcal{L}(\vec{x}_s, n_s, \gamma) = \int_{T_o} \int_{\log \sigma_T} \mathcal{L}(\vec{x}_s, n_s, \gamma, T_o, \sigma_T) P(T_o) P(\log \sigma_T) dT_o d(\log \sigma_T), \quad (9.2)$$

where  $P(T_o) = 1/T_L$  during detector uptime. Because the search is for a localized time-dependent behavior,  $T_o$  has significant freedom over the live time  $T_L$  over many orders of magnitude for short bursts. Integrating over  $T_o$  we can approximate the integral assuming an always-on detector:

$$\int_{T_o} \mathcal{L}(\vec{x}_s, n_s, \hat{\gamma}, T_o, \hat{\sigma}_T) \frac{1}{T_L} dT_o \simeq \frac{\sqrt{2\pi}\sigma_T}{T_L} \mathcal{L}(\vec{x}_s, n_s, \hat{\gamma}, \hat{T}_o, \hat{\sigma}_T). \quad (9.3)$$

The test statistic formula that is maximized is then:

$$TS = -2 \log \left( \frac{T_L}{\sqrt{2\pi}\hat{\sigma}_T} \times \frac{\mathcal{L}(n_s = 0)}{\mathcal{L}(\hat{n}_s, \hat{\gamma}, \hat{\sigma}_T, \hat{T}_o)} \right), \quad (9.4)$$

where the first factor in the logarithm is the weighting term and the second is the likelihood ratio.  $T_L$  is the total live time of data taking,  $\hat{n}_s, \hat{\gamma}, \hat{\sigma}_T, \hat{T}_o$  are the best-fit values for the number of signal events, spectral index, width and mean of the Gaussian flare, respectively. In order to prevent the weighting term from becoming less than 1, an upper limit is placed on the flare width  $\sigma_T$ . This is done to prevent flares with zero amplitude ( $\hat{n}_s=0$ ) from having a positive test statistic, which would happen if the flare width  $\sigma_T$  were allowed to be greater than  $T/\sqrt{2\pi}$ .

The numerical maximizer needs an initial candidate flare (a “first guess”). Due to the complicated behavior of the time-dependent likelihood space, a numerical minimizer requires a starting value which is close to the true minimum. This requires manual sampling. To calculate this first guess in this analysis we use the criteria to select events with  $\mathcal{S}_i/\mathcal{B}_i > 1$ , where  $\mathcal{S}_i$  and  $\mathcal{B}_i$  are defined in Section 7, omitting the time term. A plot of

the values for this ratio as a function of the distance from the tested point-source location is shown Figure 7.5. A scan is performed over sets of  $m$  temporally consecutive events, where  $2 \leq m \leq 5$ . For a stream consisting of time-ordered events numbered 1,2,3,4,5,6,7..., the initial scan tests events (1,2), (2,3), (3,4) etc., (1,2,3), (2,3,4), (3,4,5) etc., (1,2,3,4), (2,3,4,5), (3,4,5,6) etc., and (1,2,3,4,5), (2,3,4,5,6) etc. Each set is tested using the described likelihood formula for compatibility with a flare with an  $E^{-2}$  spectrum. The candidate with the best test statistic (from Equation 9.4) is used as the initial guess for the parameters in the maximization. The 40-string analysis also performs additional scans over  $m = (10, 15)$  consecutive events, and in the 59-string analysis, where the number of events is roughly a factor of 3 higher than the 40-string sample, the number of sets of consecutive scanned events has been increased to add  $m = (10, 15, 25, 40, 65)$  improving the sensitivity to flares longer than roughly 10 days. This brings the performance of the analysis close to that of the corresponding time-integrated analysis at large time scales. Given that more than 5 events are required for discovery for  $\sigma_T > 2$  days (see Fig 9.1), if the maximum  $m$  were not increased, the method will occasionally only find a subset of the injected events, hence increasing the total signal required to cross the threshold for discovery.

Figure 9.1 shows the mean number of injected events from a Gaussian time function needed for a  $5\sigma$  discovery for 50% cases (black solid line) as a function of the duration of the flare  $\sigma_T$  for a fixed source location at declination of  $+16^\circ$  with the 40-string data. Sources at other declinations yield similar results. This is compared to the number of events needed in a time-integrated search (black dashed line): the number of events needed to discover a flare of 1 s duration is about a factor of 4 lower than for a time-integrated search. At long timescales the flare search performs only 10% worse than the time-integrated search, even

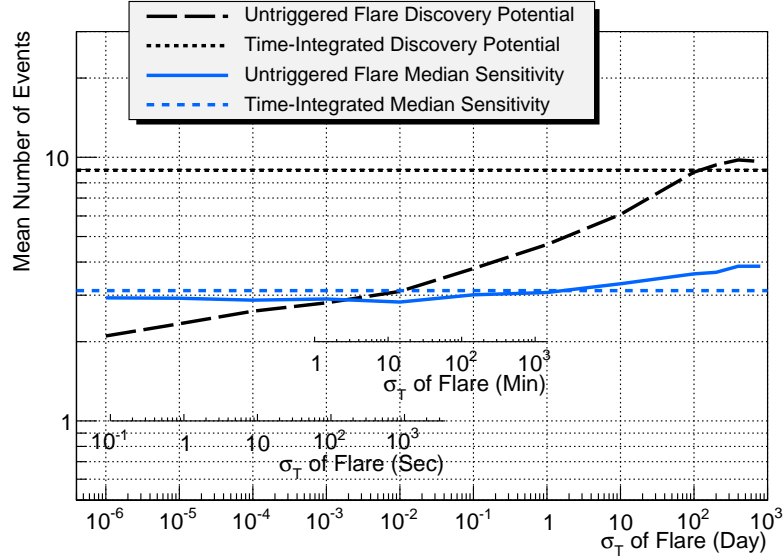


Figure 9.1 The 50%  $5\sigma$  discovery potential and 90% median sensitivity in terms of the mean number of events for a fixed source at  $+16^\circ$  declination applying the analysis to the 40-string data. The number of events for the median sensitivity and discovery potential for time-integrated searches are also shown. Flares with a  $\sigma_T$  of less than 100 days, or a FWHM of less than roughly half the total live time, have a better discovery potential than the steady search.

with 2 additional free parameters in the fit. In the same plot the median upper limits at 90% CL are shown for the time-dependent search and for the time-integrated one.

The fact that the 50%  $5\sigma$  discovery potential curve descends below the 90% median upper limit curve is due to the effect of Poisson statistics. The untriggered search must observe at least two events in order to identify a flare. For a simulated flaring source which injects a mean number of events  $\mu$ ,  $\mu$  must equal at least 1.68 for 50% of simulated trials corresponding to 2 or more signal events. Therefore, at the shortest timescales, the mean signal needed for a discovery in 50% of trials asymptotically approaches 1.68 events. We find the



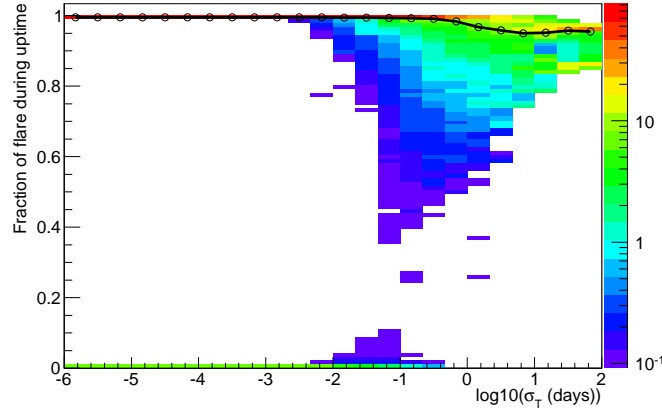


Figure 9.2 Fraction of a flare during uptime for simulated flares in the 40-string data-taking, as a function of the flare duration. The black line marks the median fraction of fluence occurring during the detector live time for a given flare duration, which is used as a correction factor for the fluence of observed flares. For instance, for flares shorter than one minute, there is approximately an 8% chance of the flare occurring completely during detector downtime. Flares longer than one day will always have some emission during uptime; on average 92% of the total emission will coincide with usable run time.

sensitivity at 90% CL saturates at 2.9 events, which is already near the time-independent sensitivity of 3.15 events and the statistical limit. This is the reason why the discovery potential curve dips lower than the sensitivity for short flares in Figure 9.1.

The method is applied as an all-sky scan over a grid ( $0.5^\circ \times 0.5^\circ$ ) in right ascension and declination. Locations which are found to have a flare are rescanned using a  $0.1^\circ \times 0.1^\circ$  grid. The final result of the analysis is the set of best fit parameters from the location with the highest test statistic value. A final  $p$ -value for this analysis is obtained by performing the same scan on scrambled data sets, and counting the fraction of scrambled sets which have a

maximum test statistic greater than or equal to the maximum found in the data.

## 9.2 Results

Using the 40-string data, the location which deviates most from the background expectation is found at  $(\text{RA}, \text{Dec}) = (254.75^\circ, +36.25^\circ)$ . Two events are found, with a best-fit spectrum  $\hat{\gamma}$  of 2.15, mean of the flare  $\hat{T}_o$  of MJD 54874.703125 (February 12, 2009) and width  $\hat{\sigma}_T$  of 15 seconds. The two events are  $2.0^\circ$  apart in space and 22 seconds apart in time. The  $-\log_{10}(\text{pretrial } p\text{-value})$  corresponding to this observation is 4.67. A clustering of higher significance is seen in 56% of scrambled skymaps, a result consistent with the null hypothesis of background-only data.

Figures 9.3 to 9.5 show maps of the pre-trial  $p$ -values and best-fit parameters  $\hat{T}_o$  and  $\hat{\sigma}_T$ . Figures 9.4 and 9.5 require that the best-fit number of signal events be greater than zero, white area corresponds to being consistent with no flare being detected.

The most significant flare in the 59-string data is found at  $(\text{RA}, \text{Dec}) = (21.35^\circ, -0.25^\circ)$ . The peak of the flare occurs on MJD 55259 (March 4, 2010), and has a width  $\hat{\sigma}_T$  of 5.5 days and a soft spectral index of  $\hat{\gamma} = 3.9$ . The  $-\log_{10}(\text{pretrial } p\text{-value})$  of the flare is 6.69, a value of which is found in 14 of 1000 of scrambled maps. Even though this  $p$ -value is somewhat rare, it is not rare enough to make a claim of a deviation from background. Figures 9.6 to 9.8 show maps of the pre-trial  $p$ -values and best-fit parameters  $\hat{T}_o$  and  $\hat{\sigma}_T$ . Figure 9.9 shows the event weights from the position of maximum significance plotted throughout the year, a clustering near the time of the best-fit parameters is clearly visible. The reconstructed directions of the 17 most signal-like events with their time-independent event weights can be seen in Figure 9.10. When we take a bin of  $2^\circ$  in space and 13 days in time centered on the peak (the FWHM of the flare), we find 13 events compared to an expected background

of 1.7. The surrounding area was scanned for candidate sources, none were found. There is also no activity from the location using the *Fermi* LAT GeV photon data since its launch.

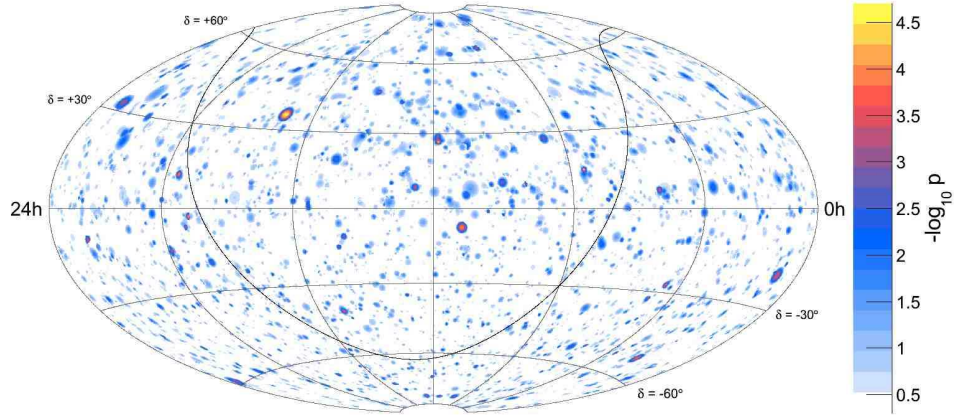


Figure 9.3 The equatorial coordinate map shows the  $p$ -value of the most significant flare in time and space during the 40-string data taking period at each location of the grid where the likelihood is calculated. The  $p$ -value is indicated on the  $z$ -scale on the right, with the maximum at 16h 59m,  $+36.25^\circ$ . The black curve is the Galactic plane.

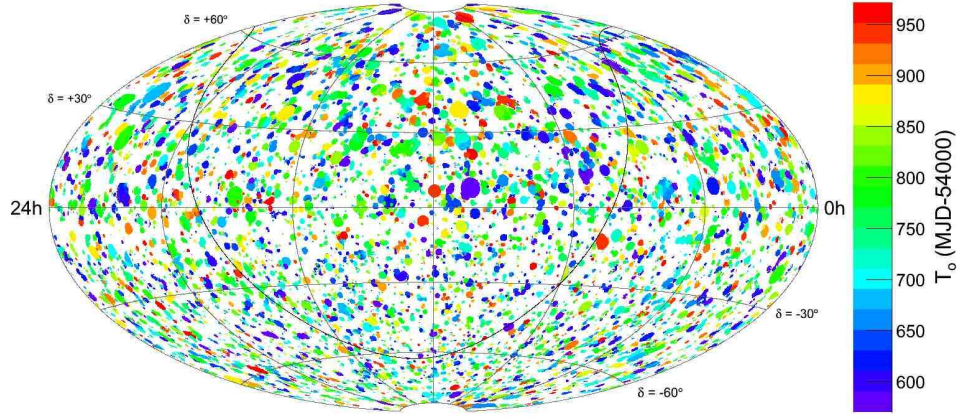


Figure 9.4 The equatorial coordinate map shows the best fit of the mean time of the flare  $\hat{T}_o$  (MJD-54,000) for the most significant flare during the 40-string data taking period found at each location of the grid where the likelihood is calculated. The black curve is the Galactic plane.

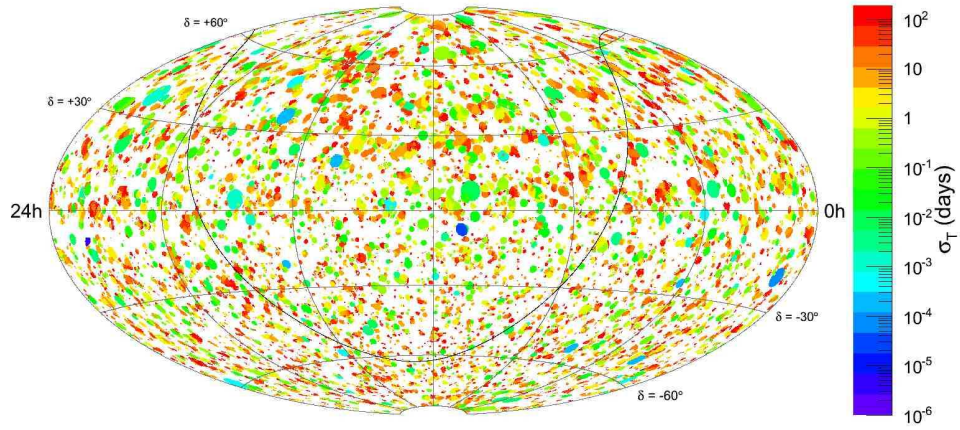


Figure 9.5 The map in equatorial coordinates of the best fit width  $\hat{\sigma}_T$ , in days, of most significant flare at a given location found using the 40-string data at each location of the grid where the likelihood is calculated in the search. The black curve is the Galactic plane.

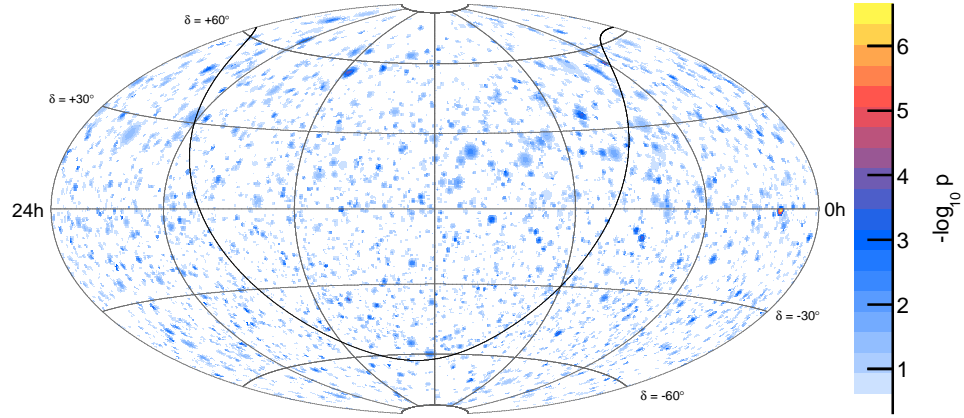


Figure 9.6 The map in equatorial coordinates of the pretrial  $p$ -value for the 59 string dataset all-sky flare search. The most significant flare can be seen in the center-right at 1h 25m,  $-0.25^\circ$ . The black curve is the Galactic plane.

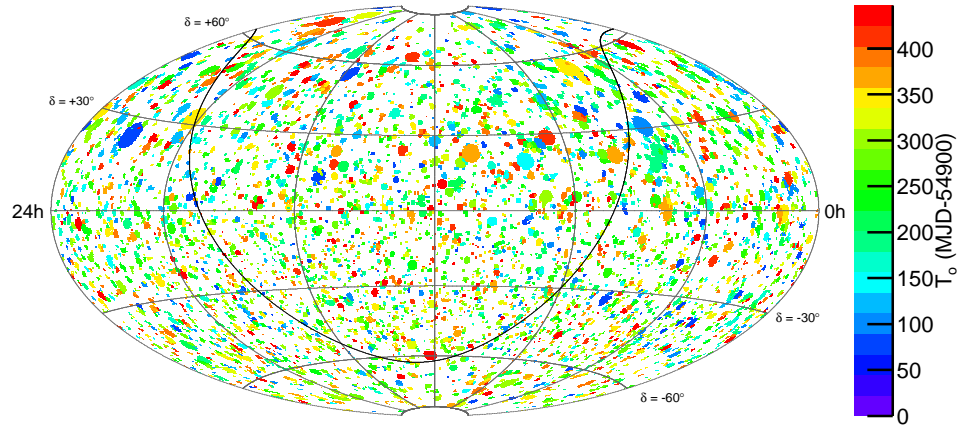


Figure 9.7 The equatorial coordinate map shows the best fit of the mean time of the flare  $\hat{T}_o$  (MJD-54,900) for the most significant flare during the 59-string data taking period found at each location of the grid where the likelihood is calculated. The black curve is the Galactic plane.

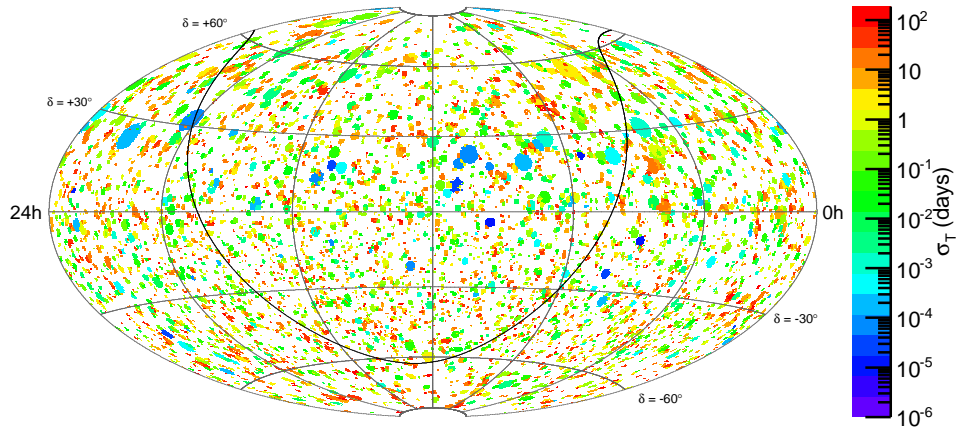


Figure 9.8 The map in equatorial coordinates of the best fit width  $\hat{\sigma}_T$ , in days, of most significant flare during the 59-string data taking period at a given location found at each location of the grid where the likelihood is calculated in the search. The black curve is the Galactic plane.

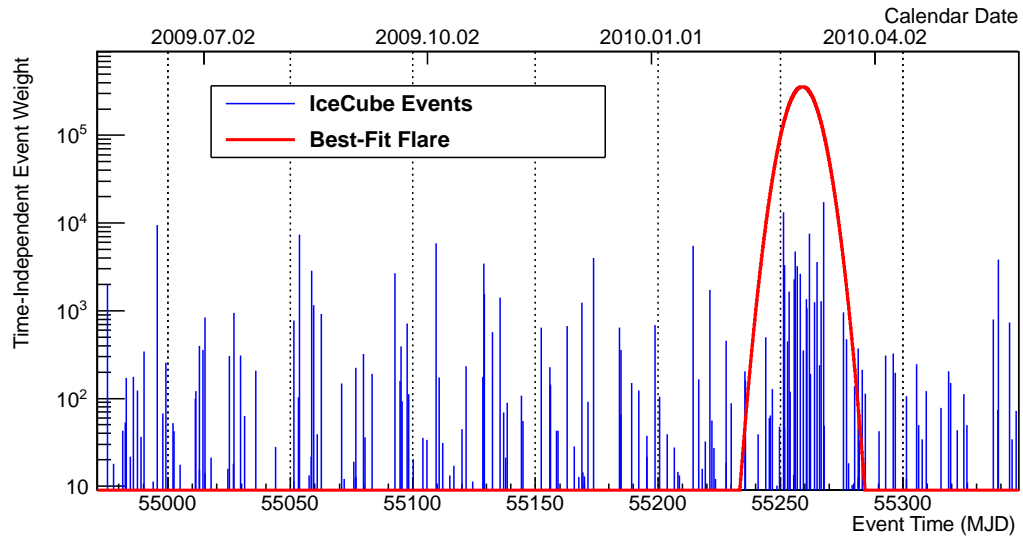


Figure 9.9 The event weights tested from the most significant flare location from the 59-string data at ( $\text{RA}=21.35^\circ$ ,  $\delta=-0.25^\circ$ ) and the best-fit spectral index of  $E^{-3.9}$ . The events are somewhat low-energy and roughly  $1^\circ$  from the hottest location, only particularly standing out by virtue of their time structure. The best-fit Gaussian flare for this location is shown in red, with an arbitrary scaling.

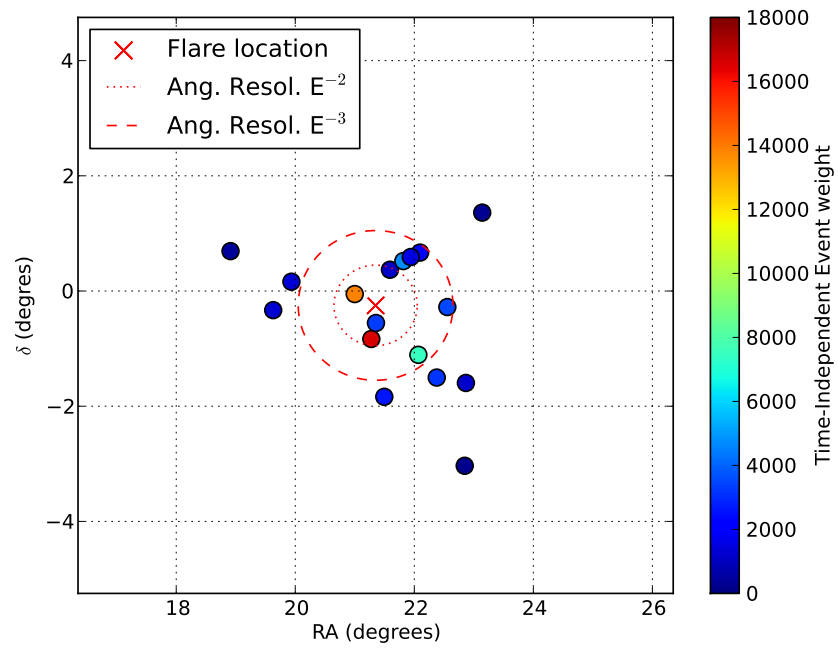


Figure 9.10 The 17 most significant events seen from the 59-string most significant flare location with their sky coordinates and time-independent event weights. Other events during the flare period are not plotted. The flare location is marked with an X, along with the median angular resolution for two different signal spectra.



## Chapter 10

# Triggered Searches for Flares of Neutrino Point Sources

This chapter presents the introduction of astronomical information as an *a priori* motivation for time-dependent neutrino point-source searches. The assumption is that for objects such as blazars, emission of neutrinos and high energy photons will be correlated. Thus, when there is an enhancement in GeV-TeV photons there will also be an enhancement for neutrinos detectable with IceCube.

Two methods are described; which is used depends on the temporal coverage of the source in a particular waveband. For both cases the method is described and results for catalogues of flaring sources are presented. The first method is used for sources with flares in wavebands where photon data is comprehensive, and at any point in time the source can be said to be in a high or low state; a second method is used for sources or bands with sporadic coverage and the source is mostly uncovered in the waveband, the MWL data is used to make an *a priori* cut in time near a flare. For flares lasting on the order of one day, MWL information can produce a discovery with about one third fewer signal events with respect to untriggered searches [124].

## 10.1 Triggered Searches Based on Continuous Photon Observations

This section describes searches for which the photon observations are comprehensive in time. The flux measurements provided by the Fermi Gamma-Ray Space Telescope are used. The source selection was motivated by Fermi alerts, which are issued for sources seen at a flux level greater than  $1.5 - 2 \times 10^{-6}$  photons  $\text{s}^{-1} \text{cm}^{-2}$ . The selected sources are listed in Table 10.1. These sources include 23 objects seen to be flaring during 40-string or 59-string data-taking, or both. They are mainly FSRQs, with several BL Lac objects. The light curves were produced for this work as described in Section 3.2.2, with two modifications to this procedure: the blazar 3C 454.3 was seen in a massive outburst before official science operation [136], for this source the published light curve is used. Also, the source PKS 1502+106 was noted to have a large outburst immediately before official science operations began, extending several days after the public information begins [57, 58]. PKS 1502+106 is taken to be flaring because the time of the alert at a fixed flux level. This flaring activity is a possible orphan flare in hard X-rays, because the SWIFT-BAT did not observe any evident flare in the 15-50 keV band while SWIFT XRT and UVOT observed a flare in soft X-rays and optical.

### 10.1.1 Method and Expected Performance

A Maximum Likelihood Block (MLB) algorithm [137, 138] is used to denoise the light curves by iterating over the data points to select periods from the light curves which are consistent with constant flux once statistical errors are taken into account. The MLB algorithm compares the likelihood that a set of points between  $x_i$  and  $x_f$  is compatible at a confidence level with the change of state between the points  $x_c$  and  $x_{c+1}$  contained in the interval. The confidence level requires that for a given set of data points from  $x_i$  to  $x_f$  that

the set of points from  $x_i$  and  $x_c$  and  $x_{c+1}$  to  $x_f$  be:

$$\log \left( \frac{\mathcal{L}(x_i, x_c) \mathcal{L}(x_{c+1}, x_f)}{\mathcal{L}(x_i, x_f)} \right) > \log C, \quad (10.1)$$

where  $\mathcal{L}(x_a, x_b)$  represents the likelihood that a set of points from  $x_a$  to  $x_b$  represents a constant flux state from the source between the points, and  $C$  is the confidence level. The level of the flux state is determined using the error-weighted mean of the points tested. The method iterates over the different possible change-points  $x_c$ , taking the most likely change-point for the entire dataset and iterating over each subsection of the data. We tested values of  $\log C$  from 1 to 1000. For values below 5, the typical denoised light curve typically follow each data point, for values from 9 to 100 very similar results for the denoised light curves were found. The final value of  $\log C$  used in the analysis was 9.

With the hypothesis that the intensity of the neutrino emission follows the intensity of the photon light curve, the signal time PDF is simply the normalized light curve itself. A slightly modified hypothesis is that the neutrino emission follows the light curve, but only when the photon flux goes above a certain threshold  $F_{\text{th}}$ . In this case, the value of  $F_{\text{th}}$  can be used as a free parameter in the analysis, finding the value of the threshold which maximizes the significance of the data. This method also avoids any penalty from making an incorrect *a priori* choice on a flaring threshold.  $F(t_i)$  is defined as the value of the denoised light curve at  $t_i$  and the fit parameter  $F_{\text{th}}$  is the flux threshold below which no neutrino emission is assumed (i.e.  $S_i^{\text{time}}=0$  if  $F(t_i) \leq F_{\text{th}}$ ). In the case of  $F(t_i) \geq F_{\text{th}}$ , the probability of neutrino emission is assumed to be proportional to the flux level above that threshold:

$$S_i^{\text{time}} = \frac{F(t_i) - F_{\text{th}}}{N_f}; \quad (10.2)$$

where the normalization factor  $N_f$  is the integral of the denoised light curve above the

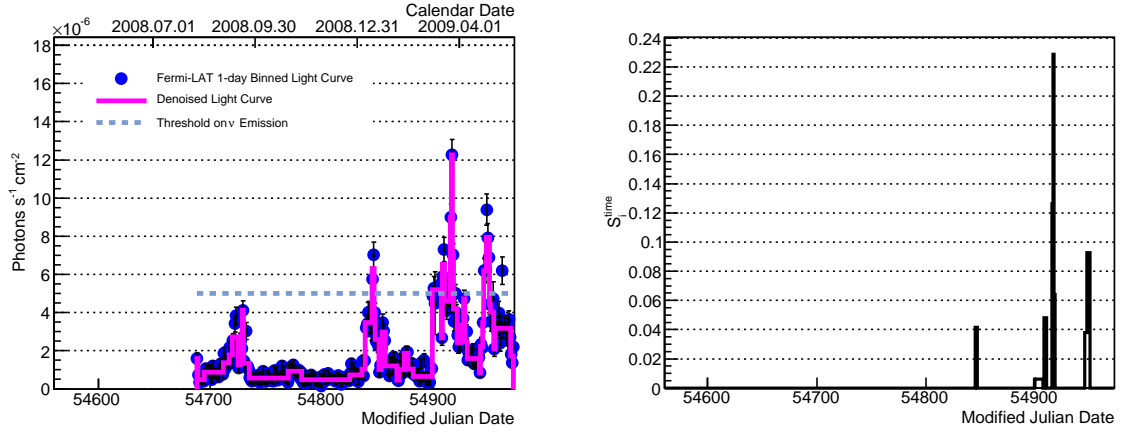


Figure 10.1 (Left) An example of the one-day binned Fermi light curve (blue points, with statistical errors) and denoised light curve (pink solid line) for the blazar PKS 1510-089 during the 40-string data taking period. The dashed line is an example fit threshold. The light curve begins here on August 10, 2008 (MJD 54688), when Fermi science operations began, while the time axis shows the entire 40-string data taking period. (Right) The time PDF used in the neutrino signal hypothesis corresponding to the example photon threshold shown in the left graph ( $5 \times 10^{-6}$  photons s<sup>-1</sup> cm<sup>-2</sup>).

threshold. This time-dependent PDF is then used as before in Equation 7.4. This method is illustrated in Figure 10.1.

The effect of adding this additional degree of freedom in the fit can be seen in Figure 10.2. The effect is small compared to the penalty of fixing the threshold to an incorrect value. The effect of allowing an unknown lag up to  $\pm 50$  days between the photon and neutrino emissions was also tested, and was found to give a marked increase in the number of events required for discovery. Hence, we used the method allowing only up to a  $\pm 0.5$  day

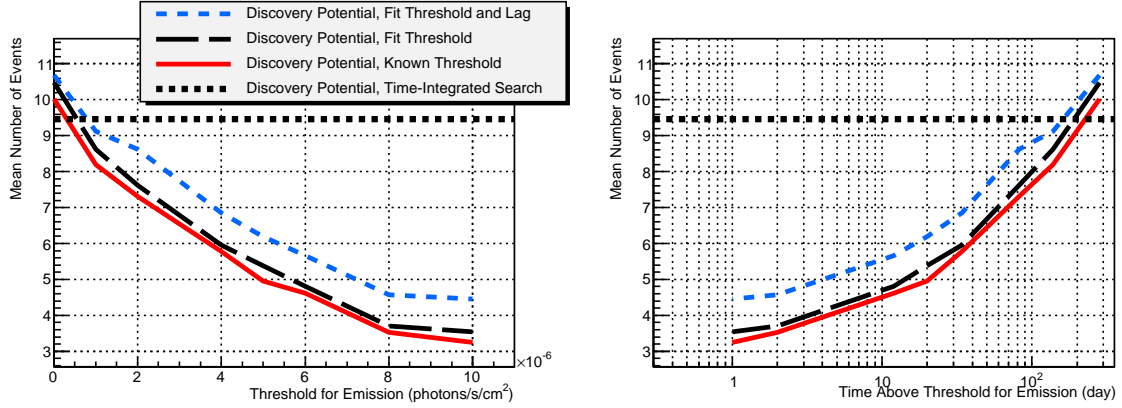


Figure 10.2 The plot of the  $5\sigma$  50% discovery potential for the source PKS 1510-089 (the corresponding light curve is shown in Figure 10.1), as a function of the true flux threshold for neutrino emission (left) and as a function of the duration the light curve spends above the threshold (right). The discovery potential curves are plotted for the time-integrated case (black short dashed line), and from bottom to top for the case where the threshold is fixed to the true threshold (solid red line), the case where the threshold is a free parameter (black long dashed line, used in this analysis) and the case where there is an unknown lag (up to  $\pm 50$  days) between GeV and neutrino emission (blue dashed line).

lag that accounts for the 1 day binning of light curves.

### 10.1.2 Results

The results from all sources using the combined 40 and 59-string data are listed in Table 10.1. The most significant source is PKS 1622-253, which has a pre-trial  $p$ -value of 8%. The method finds two events during the strongest flare during April 2010. We find a  $p$ -value which is more significant from any of the sources in 53% of scrambled samples, which is compatible with background fluctuations. The analysis was first performed using only the

40-string data, the most significant source is PKS 1502+106, with a pre-trial  $p$ -value of 5%, which occurred in 29% of scrambled trials.

Source	Location (dec <sup>[°]</sup> ,ra <sup>[°]</sup> )	p-value (pretrial)	$\hat{n}_s, \hat{\gamma}_s$ lag, $\hat{F}_{th}$	Event Plot
3C 454.3	(343.49, 16.15)	0.462	0.639 2.15 -0.227 1.77e-05	<p>The event plot for 3C 454.3 displays the event weight (blue line) and the GeV flux (red line) as a function of event time in Modified Julian Days (MJD). The x-axis ranges from 54600 to 55300 MJD. The left y-axis represents the event weight on a logarithmic scale from 10<sup>2</sup> to 10<sup>5</sup>. The right y-axis represents the GeV flux in photons/cm<sup>2</sup>/s on a logarithmic scale from 10<sup>-7</sup> to 10<sup>-4</sup>. The plot includes a legend indicating Background Events (blue line), Denoised Fermi LC (red line), and Best-Fit Threshold (dashed red line). The event weight shows significant fluctuations, with a notable peak around 55100 MJD. The GeV flux also shows a corresponding peak at this time.</p>
PKS 0805-07	(122.06, -7.85)	0.5	0.214 3.95 -0.374 0	<p>The event plot for PKS 0805-07 displays the event weight (blue line) and the GeV flux (red line) as a function of event time in Modified Julian Days (MJD). The x-axis ranges from 54600 to 55300 MJD. The left y-axis represents the event weight on a logarithmic scale from 10<sup>2</sup> to 10<sup>5</sup>. The right y-axis represents the GeV flux in photons/cm<sup>2</sup>/s on a logarithmic scale from 10<sup>-7</sup> to 10<sup>-4</sup>. The plot includes a legend indicating Background Events (blue line), Denoised Fermi LC (red line), and Best-Fit Threshold (dashed red line). The event weight shows significant fluctuations, with a notable peak around 55100 MJD. The GeV flux also shows a corresponding peak at this time.</p>

**Table 10.1 – continued from previous page**

Source	Location (dec[°],ra[°])	p-value (pretrial)	$\hat{n}_s, \hat{\gamma}_s$ lag, $\hat{F}_{th}$	Event Plot
PKS 2023-07	(306.46, -7.59)	—	0 — 0 0	
PKS 0244-47	(41.5, -46.84)	0.454	0.990 3.85 -0.245 4.05e-07	



**Table 10.1 – continued from previous page**

Source	Location (dec <sup>°</sup> ,ra <sup>°</sup> )	p-value (pretrial)	$\hat{n}_s, \hat{\gamma}_s$ lag, $F_{th}$	Event Plot
BL Lac	(330.68, 42.28)	0.498	1.81 3.00 0.09 6.07e-07	
V407 Cyg	(315.54, 45.77)	—	0 — 0 0	

**Table 10.1 – continued from previous page**

Source	Location (dec $^{\circ}$ ,ra $^{\circ}$ )	p-value (pretrial)	$\hat{n}_s, \hat{\gamma}_s$ lag, $\hat{F}_{th}$	Event Plot
PKS 1622-253	(246.44, -25.44)	0.0828	1.76 2.85 0.5 2.30e-06	
PKS 1424-418	(216.98, -42.09)	—	0 — 0 0	

**Table 10.1 – continued from previous page**

Source	Location (dec $^{\circ}$ ,ra $^{\circ}$ )	p-value (pretrial)	$\hat{n}_s, \hat{\gamma}_s$ lag, $\hat{F}_{th}$	Event Plot
J 0109+6134	(17.25, 61.34)	0.479	1.82 1.81 -0.434 0	
GB6 B1310+484	(198.18, 48.47)	—	0 — 0 0	

**Table 10.1 – continued from previous page**

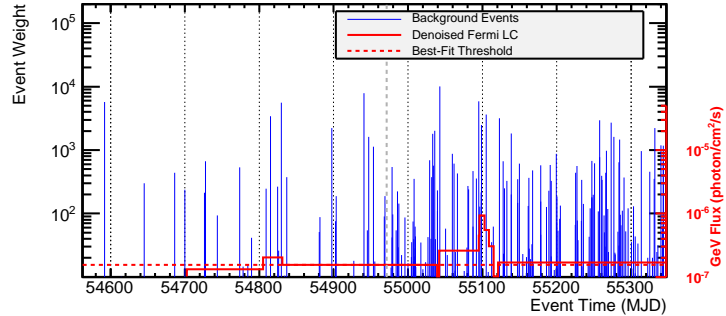
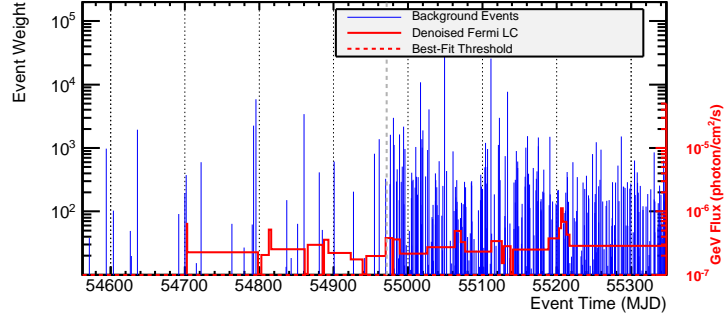
Source	Location (dec[°],ra[°])	p-value (pretrial)	$\hat{n}_s, \hat{\gamma}_s$ lag, $\hat{F}_{th}$	Event Plot
B3 1343+451	(206.39, 44.88)	0.408	2.89 2.65 -0.052 1.55e-07	
S5 1803+784	(270.19, 78.47)	0.260	6.43 3.95 -0.5 0	

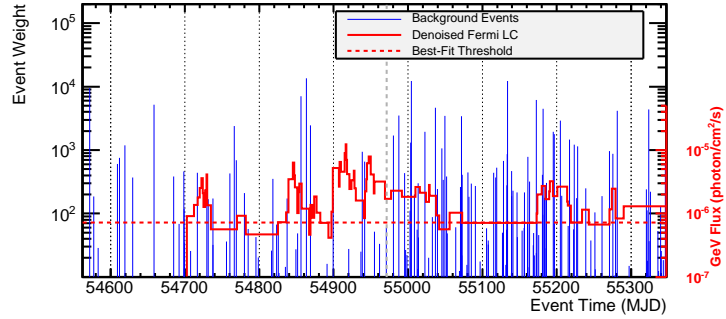
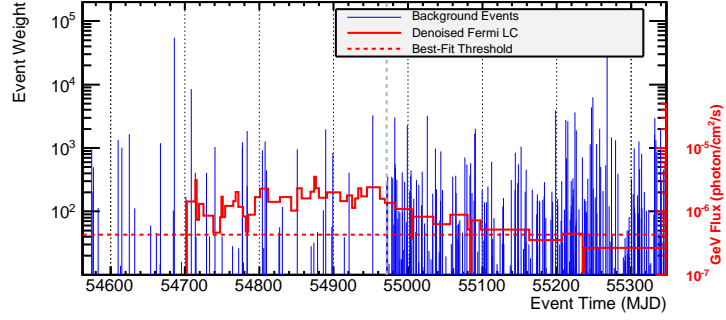
Table 10.1 – continued from previous page

Source	Location (dec[°],ra[°])	p-value (pretrial)	$\hat{n}_s, \hat{\gamma}_s$ lag, $\hat{F}_{th}$	Event Plot
PKS 1222+216	(186.23, 21.38)	—	0 — 0 0	
3C 273	(187.28, 2.05)	0.416	1.41 1.85 0.5 1.37e-06	

**Table 10.1 – continued from previous page**

Source	Location (dec[°],ra[°])	p-value (pretrial)	$\hat{n}_s, \hat{\gamma}_s$ lag, $\hat{F}_{th}$	Event Plot
OJ287	(133.70, 20.11)	0.492	1.00 2.72 0.247 3.44e-07	
4C 38.41	(248.81, 38.13)	0.217	3.83 2.05 -0.167 7.89e-07	

**Table 10.1 – continued from previous page**

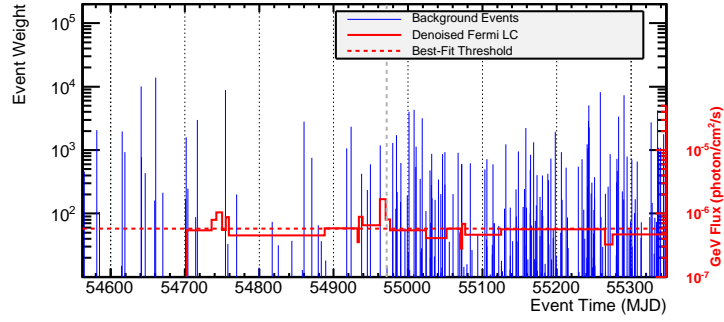
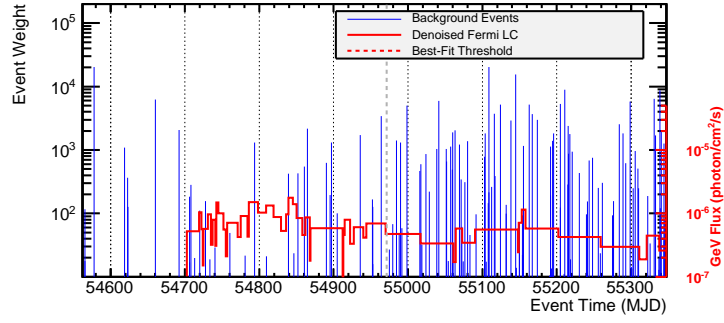
Source	Location (dec $^{\circ}$ ,ra $^{\circ}$ )	p-value (pretrial)	$\hat{n}_s, \hat{\gamma}_s$ lag, $F_{th}$	Event Plot
PKS 1510-089	(228.21, -9.10)	0.497	1.76 3.95 -0.33 7.24e-07	
PKS 1502+106	(226.10, 10.49)	—	0 — 0 0	

**Table 10.1 – continued from previous page**

Source	Location (dec[°],ra[°])	p-value (pretrial)	$\hat{n}_s, \hat{\gamma}_s$ lag, $\hat{F}_{th}$	Event Plot
PKS 1454-354	(224.36, -35.65)	0.301	6.97 3.95 0.188 3.30e-10	
3C 279	(194.05, -5.79)	0.383	0.825 3.65 0.4 2.33e-06	



**Table 10.1 – continued from previous page**

Source	Location (dec $^{\circ}$ ,ra $^{\circ}$ )	p-value (pretrial)	$\hat{n}_s, \hat{\gamma}_s$ lag, $\hat{F}_{th}$	Event Plot
3C 66A	(35.67, 43.04)	0.428	1.90 3.95 -0.355 5.79e-07	
PKS 0454-234	(74.26, -23.41)	0.264	8.26 3.95 0.0132 1.29e-10	

**Table 10.1 – continued from previous page**

Source	Location (dec[°],ra[°])	p-value (pretrial)	$\hat{n}_s, \hat{\gamma}_s$ lag, $\hat{F}_{th}$	Event Plot
J 1239+044	(189.90, 4.70)	—	0 — 0 0	

Table 10.1: The sources, locations, pretrial  $p$ -values, and best-fit parameters of the 23 objects tested with the continuous light curve search.  $P$ -values and spectral indices are not reported if the best-fit signal fraction is zero. Also plotted are the denoised light curves with the time-independent event weights at the source location from the 40 and 59-string data. A horizontal gray line marks the transition from 40-string to 59-string data-taking. If a non-zero best-fit threshold on the light curve is found, that is also plotted.

## 10.2 Triggered Searches Based on Intermittent Photon Observations

Ground based observatories such as HESS, MAGIC, and VERITAS cannot monitor sources continuously, because they can only operate when there is good night-time visibility. Their observations are nevertheless extremely important for neutrino searches, because they detect photons at TeV energies that are potentially better correlated to neutrinos of the energies to which IceCube is sensitive. While these observatories can issue alerts for source activity, they often cannot constrain the beginning or end of the activity to within a few days. For alerts such as these, the present analysis uses a simple time cut, taking a window for events one day before and after the identified flare. The catalogue corresponding to the 40-string data includes a recent suspect “orphan flare” at the level of 10 Crab from Mrk 421 observed by VERITAS and MAGIC [59, 60].

### 10.2.1 Method and Expected Performance

The nature of this analysis is a simple cut in time between  $t_{\min}$  and  $t_{\max}$ , which can be expressed as:

$$S_i^{\text{time}} = \frac{H(t_{\max} - t_i) \times H(t_i - t_{\min})}{t_{\max} - t_{\min}} \quad (10.3)$$

where  $t_i$  is the arrival time of the event,  $t_{\max}$  and  $t_{\min}$  are the upper and lower bounds of the time window defining the flare, and  $H$  is the Heaviside step function. This time-dependent signal PDF is then used in Equation 7.4. In this analysis, the signal population size  $n_s$  and spectrum index  $\gamma$  are the only fit parameters.

### 10.2.2 Results

Of the six sources tested with the 40-string data (Table 10.2), five showed no excess of events in the vicinity of the sources during the selected time periods. The final post-trial  $p$ -value for the 40 string analysis combined these flares and 11 sources seen in a heightened state with the Fermi LAT, and is 29%.

Source	dec [°]	ra [°]	Alert Ref.	Time Window (MJD)	$p$ -value (pre-trial)
Markarian 421	38.2	166.1	[139]	54586-54592	—
			[60]	54621-54631	—
W Comae	28.2	185.4	[140]	54623-54627	—
S5 0716+714	71.3	110.5	[141]	54572-54582	0.34
SGR 0501+4516	45.3	75.3	[142]	54700-54706	—
1ES 1218+304	30.2	185.3	[143]	54859-54864	—
Markarian 501	39.8	253.5	[139]	54951-54953	—

Table 10.2 Flare list seen with occasional coverage during the 40-string data-taking. References are for the alert which prompted the selection. The  $p$ -value is reported only when  $\hat{n}_s$  is greater than zero. The flare windows for Markarian 421 were added together, only one  $p$ -value for both periods is calculated.

## Chapter 11

### Periodic Emission Search

This chapter outlines a search for neutrinos emitted by binary systems in the galaxy which are thought to be particle accelerators. These binary systems typically contain a large OB or Wolf-Rayet star and a compact object such as a neutron star or black hole. Gas from the star is gravitationally pulled off by the compact object, forming an accretion disk. The result is an object which is a diminutive version of an active galaxy, objects which are seen to emit jets of matter are termed “micro-quasars.” We present the results of the search using the 40-string data, and comparisons to emission models for the binary objects tested.

The binary system LS I +61° 303 has been observed to have a periodic modulation of the photon emission in the TeV and GeV  $\gamma$  bands [144, 88], this search is extended to other microquasars and binary systems. The modulation in the LS I +61° 303 emission is interpreted as an indication of the absorption of  $\gamma$ -rays in the system depending on the relative position of the observer and the accelerator. Also included in the catalogue are sources which have not been observed in TeV  $\gamma$ -rays, but exhibit modulation in lower energy bands and have orbital periods obtained from optical observations. Photons from the jet of the compact object can be absorbed in the massive star companion when it is between the compact object and the Earth (superior conjunction), while neutrinos may be produced close

to the superior conjunction or when the jet skims the edge of the massive star [145]. It is assumed that the neutrino emission period is the same as for photons, but in this search the phase is left as a free parameter in the method, to be sensitive to possible shifts in phase between neutrinos and photons. The period for each source is taken from photon measurements, each cited in Table 11.1.

## 11.1 Method and Expected Performance

This search obtains the best fit values for the signal fraction, spectral index, and the peak phase and duration of neutrino emission by maximizing the likelihood ratio. As a signal hypothesis, a Gaussian emission repeating each orbit is assumed. Hence the time-dependent PDF is:

$$S_i^{\text{time}} = \frac{1}{\sqrt{2\pi}\sigma_T} e^{-\frac{|\varphi_i - \varphi_0|^2}{2\sigma_T^2}}, \quad (11.1)$$

where  $\sigma_T$  is the width of the Gaussian,  $\varphi_i$  is the phase of the event and  $\varphi_0$  is the phase of the peak of the emission. The fit parameters are the mean  $\sigma_T$  and width  $\varphi_0$ .

Comparing to the unbinned time-integrated analysis, the search for periodicity in neutrino emission results in a better discovery potential if the duration of the emission  $\sigma_T$  is less than about 20% of the total period (see Figure 11.1). As the time-dependent search adds two additional degrees of freedom to the analysis, the discovery potential is roughly 10% worse if neutrinos are actually emitted at a steady rate or over a large fraction of the period. If the emission has a  $\sigma_T$  of 1/50 of the period the method requires half as many events for discovery.

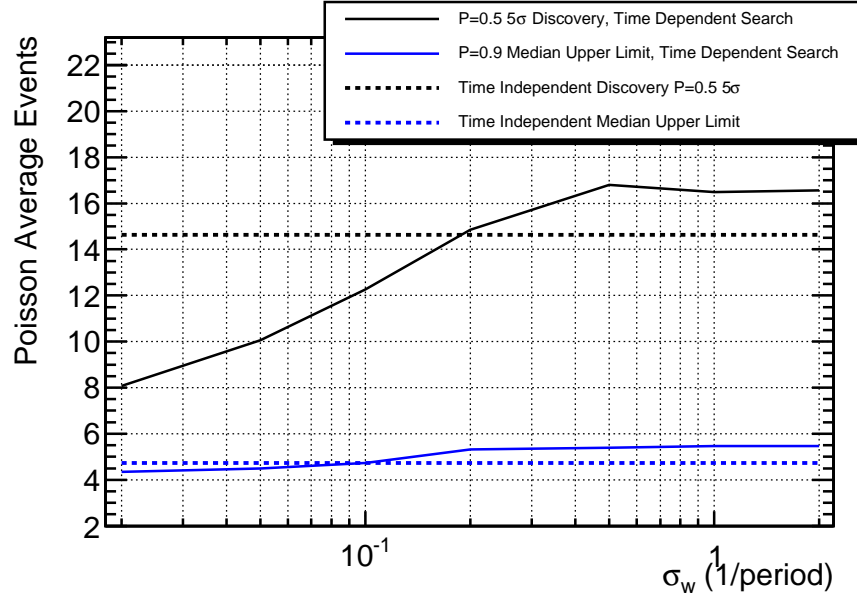


Figure 11.1 Discovery potentials ( $5\sigma$  in 50% trials, solid black lines in the plot) and the median sensitivity at 90% CL calculated with the Feldman-Cousins prescription [126] (solid and dashed blue lines) for the periodic search applied to the 40-string data. Also shown are the values for the time-integrated search [146] (dashed lines).

## 11.2 Results

Seven predefined sources listed in Table 11.1 were tested using the 40-string event selection. The most significant deviation is for Cygnus X-3. The pretrial p-value of this source is 0.00186, where an equivalent best p-value from any of the sources is found in 1.8% of scrambled samples, a result which is compatible with random fluctuations. The peak emission is found to be at phase  $\hat{\varphi}_0 = 0.82$ , and  $\hat{\sigma}_T = 0.02$ . The best-fit number of source events is  $\hat{n}_s = 4.28$  and the spectrum is soft at  $\hat{\gamma}_s = 3.75$ .

Fig. 11.2 compares the 40-string time-integrated limits to the model predictions by Distefano et al. for each source [154]. The model predicts the neutrino flux based on the

Source	Period (days)	p-value (pretrial)	$T_0$ (MJD)	$\hat{\varphi}_o$ (phase)	$\hat{\sigma}_T$ (period <sup>-1</sup> )	Reference	Time-Dependent UL (TeV <sup>-1</sup> cm <sup>-2</sup> s <sup>-1</sup> )	Time-Integrated UL (TeV <sup>-1</sup> cm <sup>-2</sup> s <sup>-1</sup> )
Cygnus X-3	0.199679	0.00186	54896.693	0.819	0.02	[147]	$3.01 \cdot 10^{-11}$	$6.64 \cdot 10^{-12}$
Cygnus X-1	5.5929	0.080	41874.707	0.031	0.02	[148]	$4.08 \cdot 10^{-12}$	$7.41 \cdot 10^{-12}$
LS I+61° 303	26.498	0.23	43366.775	0.916	0.02	[149]	$1.82 \cdot 10^{-11}$	$9.78 \cdot 10^{-12}$
GRS 1915+105	30.8	0.43	53945.7	0.502	0.045	[150]	$2.57 \cdot 10^{-12}$	$3.23 \cdot 10^{-12}$
SS 433	13.0821	0.35	50023.62	0.779	0.02	[151]	$3.15 \cdot 10^{-12}$	$3.03 \cdot 10^{-12}$
XTE J1118+480	0.169934	0.28	52287.9929	0.985	0.132	[152]	$7.29 \cdot 10^{-12}$	$8.18 \cdot 10^{-12}$
GRO J0422+32	0.21214	0.037	50274.4156	0.831	0.02	[153]	$1.46 \cdot 10^{-11}$	$6.89 \cdot 10^{-12}$

Table 11.1 System name, period, pre-trial p-value, and the time of zero phase for the binary systems tested.  $\hat{\sigma}_T$  is the fraction of the standard deviation of the best-fit Gaussian of the period of the binary system. Also included is the reference used for the orbital information. In the last columns we give the upper limits of Feldman-Cousins [126] 90% confidence intervals as the normalization on an E<sup>-2</sup> spectrum flux for the time-dependent and integrated hypotheses for the 40 strings data. The upper limits also incorporate a 16% systematic uncertainty.



radiative luminosity associated to the jet from radio observations in quiescent states and during flares. The duration of flares is specified in Tab. 4 in the paper. The figure shows limits for both the persistent case and the time dependent one for a time window similar to the observed flare but not coincident to it (because IceCube was not active at the time of radio observations noted in the paper). For the persistent case of SS 433 the model predicts more than 100 events during the 40-string data taking period, which is excluded at greater than 99% confidence level. It should be considered that the authors indicate in their paper that the model may be biased by the fact that the source is surrounded by a the diffuse nebula W50 that can affect the estimate of the radio emission used in the model for SS 433.

The main parameters on which the neutrino flux depends in this model are: the fraction of jet kinetic energy converted to internal energy of electrons and magnetic field,  $\eta_e$ ; the fraction of the jet luminosity carried by accelerated protons,  $\eta_p$ ; and the fraction of energy in pions  $f_\pi$ , which strongly depends on the maximum energy to which protons can be accelerated. The case of a 3-day burst of Cygnus X-3 is used as an example of how the parameters are constrained by the IceCube results. We assume equipartition between the magnetic fields and the electrons and the proton component ( $\eta_p = \eta_e$ ) for setting a constraint on  $f_\pi < 0.11$ . If equipartition does not apply, it is assumed that  $f_\pi = f_{\pi,peak}$  as given in Table 2 in the paper (for Cygnus X-3  $f_{\pi,peak} = 0.12$ ) and constrain  $\eta_p$  to be less than 92% of  $\eta_e$ . Deriving these limits it is assumed that the Lorentz factor of the jet is well known from radio measurements, but in many cases there is a large uncertainty on this parameter. Overall the constraints are roughly at the model predictions, but will be improved by the addition of more data.

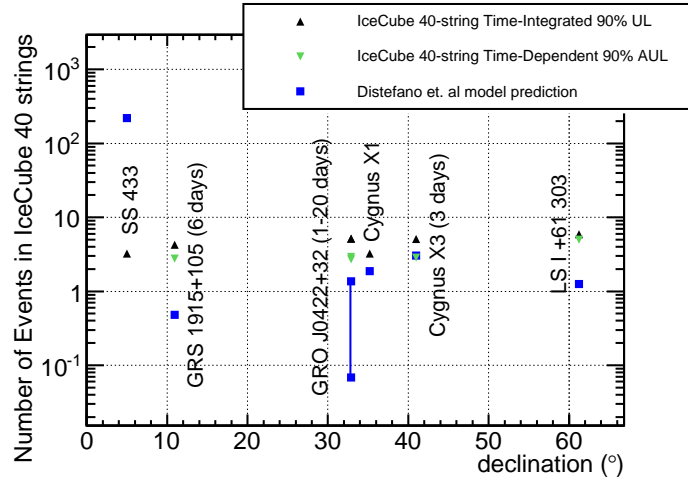


Figure 11.2 The time-integrated upper limit (UL) at 90% CL is compared to the expected number of events for model predictions according to [154] for specific sources for the 40 string configuration. The neutrino energy range used to calculate the total number of events is  $10^8 - 5 \times 10^{14}$  eV, compatible to what assumed in the model. For non persistent but flaring sources, the parameters of the model were estimated for flares observed before IceCube construction. Hence the time-dependent upper limits are calculated averaging over a duration equal to the model flare during 40-string data taking (indicated as MUL in the legend). LS I +61° 303 is assumed to be a periodic flaring source in a high state during 26% of the orbit.

## Chapter 12

### Conclusions

#### 12.1 Summary

Four searches for time-dependent point-sources of neutrinos are presented. One is “untriggered”, scanning over direction, energy and time to look for clusters of neutrino events; two others are “triggered” by multi-wavelength information covering 29 sources in total; and a final search uses orbital information about seven galactic binary systems to search for periodic neutrino emission. The all-sky scan over all directions finds that the most significant cluster of events occurs during the 59-string data-taking period with a  $p$ -value of 1.4%. The FWHM of the flare was 13 days, centered on March 4th, 2010. The location of the flare was not near any known sources of high-energy photons, and there was no corresponding emission detected by the Fermi LAT.

While the first search is generic and sensitive to flares not seen in photons, the others are enhanced due to the reduced trial factor from selecting specific catalogues of variable sources. Time-dependent searches can be more sensitive to short flares due to the reduction of the background of atmospheric muons and neutrinos over short time scales. The most significant observation of a flare from catalogues compiled using Fermi LAT and IACT alerts

during the period is PKS 1622-253, which has a  $p$ -value of 53%. This method finds two events during the strongest flare during April 2010. The search for periodicity in neutrino emission finds a  $p$ -value of 1.8% from the microquasar Cygnus X-3, with a peak at a phase of 0.82, near the peak measured by Fermi. All these results are compatible with a fluctuation of the background.

## 12.2 Outlook

The final strings of the IceCube detector have been deployed, and all 86 strings are in operation. The combination of data from the 40 and 59-string configurations improved the time-integrated sensitivity by a factor of 3 compared to 40 strings alone.

This, combined with the advent of the *Fermi* Gamma-ray Space Telescope, yields a unique possibility for multi-messenger astrophysics. The *Fermi* LAT is sensitive in an energy range which is important for distinguishing between leptonic and hadronic emission models of sources, which could help focus IceCube searches to obtain the “smoking-gun” evidence of hadronic acceleration and the sources of cosmic rays.

The methods we have developed here of time-dependent neutrino searches are and will continue to be a crucial part of multi-messenger searches, particularly as future datasets with larger effective areas. The methods will continue to give feedback and explore models with better sensitivity and search for signals proving the hadronic nature of objects such as blazars and GRBs. The limits using 40-string data on flares from galactic microquasars are near models which have a proton ratio of  $\sim 10\%$  in the jet [154].

The skills developed in selecting pure neutrino samples for offline analysis will also be applied towards selecting events on-line at Pole. Target of Opportunity programs have been running on-line since 2008 searching for doublets or triplets of events in a binned

region. Additional processing power added at the Pole in the 2010-11 Austral summer makes it possible to run more advanced reconstructions on a sub-set of events, so the final analysis sample could be produced in essentially real time. This opens opportunities for IceCube time-dependent analyses to be run quickly, providing useful and timely data to the astronomical community on the presence of or limits on any neutrino signal from an extraordinary astrophysical occurrence.

Significant improvements are being made in event reconstruction, with hints of reconstruction resolution on the order of arc minutes for events which deposit a large amount of light in the detector, compared to resolutions on the order of one degree which are possible now. Resolution is the most important factor contributing to point-source analyses, and a significantly improved event reconstruction could improve discovery potentials by a factor of three.

The low-energy neutrino improvements with DeepCore will also be instrumental in improving sensitivity, as the power-law fluxes we expect yield vastly more events at lower energies than at high energies. A dedicated event stream using DeepCore stands to dramatically improve the sensitivity for soft spectra and spectra with cut-off in the 1-10 TeV region. The DeepCore extension in the completed detector also has a layer of three IceCube strings to veto down-going muon tracks. This opens the possibility of using neutrino events which start inside the detector, yielding  $4\pi$  coverage of low-energy neutrinos.

As these improvements come to fruition, the IceCube Observatory stands able to open wide a window onto strange and violent behavior in some of the most powerful objects in the universe.

## Bibliography

- [1] W. Pauli. In Rapports du Septieme Conseil de Physique Solvay, Gauthier-Villars, Paris, 1934.
- [2] C. L. Cowan, Jr., F. Reines, F. B. Harrison, H. W. Kruse, and A. D. McGuire. Detection of the Free Neutrino: A Confirmation. Science, 124:103–104, July 1956.
- [3] C. Amsler and others (Particle Data Group). Physics Letters B, 667:1, 2008.
- [4] D. E. Groom, N. V. Mokhov, and S. I. Striganov. Muon Stopping Power and Range Tables 10 MeV-100 TeV. Atomic Data and Nuclear Data Tables, 78:183–356, July 2001.
- [5] B. Wiebel-Sooth, P. L. Biermann, and H. Meyer. Cosmic rays. VII. Individual element spectra: prediction and data. A&A, 330:389–398, February 1998.
- [6] J. K. Becker. High-energy neutrinos in the context of multimessenger astrophysics. Phys. Rep., 458:173–246, March 2008.
- [7] K. Greisen. End to the Cosmic-Ray Spectrum? Physical Review Letters, 16:748–750, April 1966.

- [8] G. T. Zatsepin and V. A. Kuz'min. Upper Limit of the Spectrum of Cosmic Rays. Soviet Journal of Experimental and Theoretical Physics Letters, 4:78, August 1966.
- [9] P. Abreu et al. Anisotropy and chemical composition of ultra-high energy cosmic rays using arrival directions measured by the Pierre Auger Observatory. JCAP, 1106:022, 2011. \* Temporary entry \*.
- [10] R. Abbasi et al. Observation of anisotropy in the arrival directions of galactic cosmic rays at multiple angular scales with icecube. Astrophys. J., 740(1):16, 2011.
- [11] R. Abbasi et al. Measurement of the Anisotropy of Cosmic Ray Arrival Directions with IceCube. Astrophys. J., 718:L194, 2010.
- [12] ENRICO Fermi. On the origin of the cosmic radiation. Phys. Rev., 75(8):1169–1174, Apr 1949.
- [13] E. Fermi. Astrophys. J., 119:1, 1954.
- [14] G. F Krymskii. Akademiia Nauk SSSR Doklady, 234:1306, 1977.
- [15] A. R. Bell. Month. Not. Roy. Astr. Soc., 182:147, 1978.
- [16] A. R. Bell. Month. Not. Roy. Astr. Soc., 182:443, 1978.
- [17] F. W. Stecker, M. G. Baring, and E. J. Summerlin. Astrophys. J Lett., 667:29, 2007.
- [18] A. Meli, J. K. Becker, and J. J Quenby. A&A, 492:323, 2008.
- [19] Raymond Davis, Don S. Harmer, and Kenneth C. Hoffman. Search for neutrinos from the sun. Phys. Rev. Lett., 20:1205, May 1968.

- [20] M Ambrosio et al. Measurement of the atmospheric neutrino-induced upgoing muon flux using macro. Physics Letters B, 434(3-4):451 – 457, 1998.
- [21] C. Berger et al. A study of atmospheric neutrino oscillations in the frjus experiment. Physics Letters B, 245(2):305 – 310, 1990.
- [22] Y. Fukuda et al. Evidence for oscillation of atmospheric neutrinos. Phys. Rev. Lett., 81:1562–1567, Aug 1998.
- [23] Z. Maki, M. Nakagawa, and S. Sakata. Remarks on the Unified Model of Elementary Particles. Progress of Theoretical Physics, 28:870–880, November 1962.
- [24] M.C. Gonzalez-Garcia and Yosef Nir. Neutrino masses and mixing: Evidence and implications. Rev.Mod.Phys., 75:345–402, 2003.
- [25] H. Athar, M. Ježabek, and O. Yasuda. Effects of neutrino mixing on high-energy cosmic neutrino flux. Phys. Rev. D, 62(10):103007, Oct 2000.
- [26] Rikard Enberg, Mary Hall Reno, and Ina Sarcevic. High energy neutrinos from charm in astrophysical sources. Phys.Rev., D79:053006, 2009. \* Brief entry \*.
- [27] R. Abbasi et al. Time-Integrated Searches for Point-like Sources of Neutrinos with 40 Strings of IceCube. Astrophys. J., 732:18, 2011.
- [28] R. Abbasi et al. Search for Point Sources of High Energy Neutrinos with Final Data from AMANDA-II. Phys. Rev. D, 79:062001, 2009.
- [29] S. Adrian-Martinez et al. First Search for Point Sources of High Energy Cosmic Neutrinos with the ANTARES Neutrino Telescope. arXiv:1108.0292, 2011. \* Temporary entry \*.



- [30] Bruce T. Cleveland, Timothy Daily, Jr. Raymond Davis, James R. Distel, Kenneth Lande, C. K. Lee, Paul S. Wildenhain, and Jack Ullman. Measurement of the solar electron neutrino flux with the homestake chlorine detector. Astrophys. J., 496(1):505, 1998.
- [31] S. Fukuda et al. Solar B-8 and hep neutrino measurements from 1258 days of Super-Kamiokande data. Phys.Rev.Lett., 86:5651–5655, 2001.
- [32] K. Hirata et al. Observation of a neutrino burst from the supernova sn 1987a. Phys. Rev. Lett., 58:1490, 1987.
- [33] R. M. Bionata et al. Observation of a neutrino burst in coincidence with supernova 1987a in the large magellanic cloud. PRL, 58:1494, 1987.
- [34] E. N. Alexeyev, L. N. Alexeyeva, I. V. Krivosheina, and V. I. Volchenko. Detection of the neutrino signal from sn 1987a in the lmc using the inr baksan underground scintillation telescope. Physics Letters B, 205(2-3):209 – 214, 1988.
- [35] A.A. Abdo et al. Gamma-ray flares from the Crab Nebula. Science, 331:739, 2011.
- [36] M. Schmidt. 3c 273: A star-like object with large red-shift. Nature, 197:1040, 1963.
- [37] Alan P. Marscher, Svetlana G. Jorstad, Francesca D. D’Arcangelo, Paul S. Smith, G.Grant Williams, et al. The inner jet of an active galactic nucleus as revealed by a radio - to - gamma-ray outburst. Nature, 452:966–969, 2008.
- [38] M.-P. Véron-Cetty and P. Véron. A catalogue of quasars and active nuclei: 13th edition. A&A, 518:A10, July 2010.

- [39] The Fermi-LAT Collaboration. Fermi Large Area Telescope First Source Catalog. Astrophys. J. Suppl., 188:405–436, 2010.
- [40] Alan P. Marscher et al. Probing the inner jet of the quasar pks 1510089 with multi-waveband monitoring during strong gamma-ray activity. Astrophys. J.L., 710(2):L126, 2010.
- [41] J. A. Gaidos et al. Very Rapid and Energetic Bursts of TeV Photons from the Active Galaxy Markarian 421. Nature, 383:319–320, 1996.
- [42] M. Blazejowski et al. A Multi-wavelength View of the TeV Blazar Markarian 421: Correlated Variability, Flaring, and Spectral Evolution. Astrophys. J., 630:130–141, 2005.
- [43] Jeyhan S. Kartaltepe and Thomas J. Balonek. The Multiple Timescales of Optical Variability of the Blazar 3C 279 During the 2001-2002 Outburst. Astron. J., 133:2866–2882, 2007.
- [44] D. Horan et al. Multiwavelength Observations of Markarian 421 in 2005 - 2006. Astrophys. J., 695:596–618, 2009.
- [45] M. Böttcher, A. Reimer, and A. P. Marscher. Implications of the VHE Gamma-Ray Detection of the Quasar 3C279. Astrophys. J., 703:1168, 2009.
- [46] F. Aharonian. An Exceptional VHE Gamma-Ray Flare of PKS 2155-304. Astrophys. J., 664:L71–L78, 2007.
- [47] J. Albert et al. Variable VHE gamma-ray emission from Markarian 501. Astrophys. J., 669:862, 2007.

- [48] A. Neronov and M. Ribordy. IceCube Sensitivity for Neutrino Flux from Fermi Blazars in Quiescent States. Phys.Rev., D80:083008, 2009.
- [49] Markus Böttcher. Models for the Spectral Energy Distributions and Variability of Blazars. 2010. arXiv:1006.5048.
- [50] Markus Böttcher. Modeling the Emission Processes in Blazars. Astrophys. Space Sci., 309:95–104, 2007.
- [51] A. A. Abdo et al. Fermi large area telescope observations of markarian 421: The missing piece of its spectral energy distribution. Astrophys. J., 736(2):131, 2011.
- [52] Henric Krawczynski et al. Multiwavelength observations of strong flares from the TeV-blazar 1ES 1959+650. Astrophys. J., 601:151–164, 2004.
- [53] E. Bernardini et al. Neutrino emission in the hadronic Synchrotron Mirror Model: the 'orphan' TeV flare from 1ES 1959+650. In Workshop on Particles and Radiation from Cosmic Accelerators, Chiba, Japan, 2005. <http://www.astro.phys.s.chiba-u.ac.jp/ca2005/>.
- [54] F. Halzen and D. Hooper. High energy neutrinos from the TeV blazar 1ES 1959+650. Astropart. Phys., 23:537–542, 2005.
- [55] Anita Reimer, M. Böttcher, and S. Postnikov. Neutrino emission in the hadronic Synchrotron Mirror Model: the 'orphan' TeV flare from 1ES 1959+650. Astrophys. J., 630:186–190, 2005.
- [56] A. Achterberg et al. On the selection of AGN neutrino source candidates for a source stacking analysis with neutrino telescopes. Astropart. Phys., 26:282–300, 2006.

- [57] S. Ciprini. GLAST LAT detection of a possible new gamma-ray flaring blazar: PKS 1502+106. The Astronomer's Telegram, 1650:1–+, August 2008.
- [58] : A. A. Abdo and The Multifrequency Campaign others. PKS 1502+106: a new and distant gamma-ray blazar in outburst discovered by the Fermi Large Area Telescope. Astrophys. J., 710:810–827, 2010.
- [59] V.A. Acciari et al. Simultaneous Multiwavelength Observations of Markarian 421 During Outburst. Astrophys. J., 703:169–178, 2009.
- [60] V. Vittorini et al. The June 2008 flare of Markarian 421 from optical to TeV energies. Astrophys. J., 691:L13–L19, 2009.
- [61] Peter Meszaros. Gamma-Ray Bursts. Rept. Prog. Phys., 69:2259–2322, 2006.
- [62] Tsvi Piran. The physics of gamma-ray bursts. Rev. Mod. Phys., 76:1143–1210, 2004.
- [63] Eli Waxman. Gamma-ray bursts: The underlying model. Lect. Notes Phys., 598:393, 2003.
- [64] Peter Meszaros and M. J. Rees. . Astrophys. J., 405:278, 1993.
- [65] R. Abbasi et al. Search for muon neutrinos from Gamma-Ray Bursts with the Ice-Cube neutrino telescope. Astrophys. J., 710:346–359, 2010.
- [66] R. Abbasi et al. Search for high-energy muon neutrinos from the 'naked-eye' GRB 080319B with the IceCube neutrino telescope. Astrophys. J., 701:1721–1731, 2009.
- [67] R. Abbasi et al. Limits on neutrino emission from gamma-ray bursts with the 40 string icecube detector. Phys. Rev. Lett., 106:141101, 2011.

- [68] N Whitehorn. Results from high-energy neutrino searches from gamma-ray bursts with icecube. TAUP conference, Munich, Germany, aug 2011.
- [69] S. Chandrasekhar. The Maximum Mass of Ideal White Dwarfs. Astrophys. J. Lett., 74:81–+, July 1931.
- [70] S. Chandrasekhar. The highly collapsed configurations of a stellar mass (Second paper). Mon. Not. Roy. Astron. Soc., 95:207–225, January 1935.
- [71] F. Aharonian et al. Observations of the Crab Nebula with H.E.S.S. Astron.Astrophys., 457:899–915, 2006.
- [72] E. Aliu et al. Detection of Pulsed Gamma Rays Above 100 GeV from the Crab Pulsar. arXiv:1108.3797, 2011. \* Temporary entry \*.
- [73] D. Caprioli, E. Amato, and P. Blasi. The contribution of supernova remnants to the galactic cosmic ray spectrum. Astropart.Phys., 33:160–168, 2010. \* Brief entry \*.
- [74] Sandro Mereghetti. The strongest cosmic magnets: Soft Gamma-ray Repeaters and Anomalous X-ray Pulsars. Astron. Astrophys. Rev., 15:225–287, 2008.
- [75] Francis Halzen, Hagar Landsman, and Teresa Montaruli. TeV photons and neutrinos from giant soft-gamma repeaters flares. ArXiv Astrophysics e-prints, 2005. arXiv:astro-ph/0503348.
- [76] K. Ioka et al. TeV - PeV neutrinos from giant flares of magnetars and the case of SGR 1806-20. Astrophys. J., 633:1013–1017, 2005.
- [77] Xue-Wen Liu, Xue-Feng Wu, and Tan Lu. Diffuse high energy neutrinos and cosmic rays from hyperflares of soft-gamma repeaters. New Astron., 15:292–296, 2010.

- [78] A. Achterberg et al. Limits on the high-energy gamma and neutrino fluxes from the SGR 1806-20 giant flare of December 27th, 2004 with the AMANDA-II detector. Phys. Rev. Lett., 97:221101, 2006.
- [79] Harsha S. Kumar, Alaa. I. Ibrahim, and Samar Safi-Harb. SWIFT-BAT observations of the recently discovered magnetar SGR 0501+4516. Astrophys. J., 716:97–105, 2010.
- [80] B Carrol and D. Ostlie. An Introduction to Modern Astrophysics. Benjamin Cummings, 2nd edition, 2006.
- [81] Amir Levinson and Eli Waxman. Probing microquasars with TeV neutrinos. Phys. Rev. Lett., 87:171101, 2001.
- [82] J. Albert et al. Variable very high energy gamma-ray emission from the microquasar LS I +61 303. Science, 312:1771–1773, 2006.
- [83] James C.A. Miller-Jones, Katherine M. Blundell, Michael P. Rupen, Amy J. Mioduszewski, Peter Duffy, et al. Time-sequenced multi-radio-frequency observations of Cygnus X-3 in flare. Astrophys.J., 600:368–389, 2004.
- [84] G. E. Romero, A. T. Okazaki, M. Orellana, and S. P. Owocki. Accretion vs. colliding wind models for the gamma-ray binary LS I +61 303: an assessment. A&A, 474:15–22, October 2007.
- [85] P. C. Gregory, A. R. Taylor, D. Crampton, J. B. Hutchings, R. M. Hjellming, D. Hogg, H. Hvatum, E. W. Gottlieb, P. A. Feldman, and S. Kwok. The radio, optical, X-ray, gamma-ray star LSI +61 deg 303. Astron. J., 84:1030–1036, July 1979.

- [86] F. A. Harrison, P. S. Ray, D. A. Leahy, E. B. Waltman, and G. G. Pooley. Simultaneous X-Ray and Radio Monitoring of the Unusual Binary LS I +61 deg303: Measurements of the Light Curve and High-Energy Spectrum. Astrophys. J., 528:454–461, January 2000.
- [87] L. Sidoli, A. Pellizzoni, S. Vercellone, M. Moroni, S. Mereghetti, and M. Tavani. XMM-Newton observation of a spectral state transition in the peculiar radio/X-ray/ $\gamma$ -ray source LS I +61 303. A&A, 459:901–907, December 2006.
- [88] A. A. Abdo et al. Fermi LAT Observations of LS I +61 303: First detection of an orbital modulation in GeV Gamma Rays. Astrophys. J., 701:L123–L128, 2009.
- [89] J. Albert et al. Periodic very high energy gamma-ray emission from LS I +61 303 observed with the MAGIC telescope. Astrophys. J., 693:303–310, 2009.
- [90] V.A. Acciari et al. Multiwavelength Observations of LS I +61° 303 with Veritas, Swift, and RXTE. Astrophys. J., 700(2):1034, 2009.
- [91] V. Bosch-Ramon, G. E. Romero, and J. M. Paredes. A broadband leptonic model for gamma-ray emitting microquasars. A&A, 447:263–276, February 2006.
- [92] G. Dubus, B. Cerutti, and G. Henri. Relativistic Doppler-boosted emission in gamma-ray binaries. A&A, 516:A18, June 2010.
- [93] A. M. Hillas. The origin of ultra-high-energy cosmic rays. Annual Review of Astronomy and Astrophysics, 22(1):425, 1984.
- [94] V. A. Acciari et al. TeV and Multi-wavelength Observations of Mrk 421 in 2006–2008. Astrophys. J., 738:25, 2011.

- [95] M. Voge. Time-dependent search for astrophysical neutrinos from microquasar cygnus x-3 using icecube and amanda. Master's thesis, Max Planck Institute for Nuclear Physics, Heidelberg, 2011.
- [96] D Tody. The IRAF Data Reduction and Analysis System, volume 627, pages 733–+. 1986.
- [97] D. Tody. IRAF in the Nineties. In R. J. Hanisch, R. J. V. Brissenden, & J. Barnes, editor, Astronomical Data Analysis Software and Systems II, volume 52 of Astronomical Society of the Pacific Conference Series, page 173, January 1993.
- [98] M. Villata, C. M. Raiteri, L. Lanteri, G. Sobrito, and M. Cavallone. BVR photometry of comparison stars in selected blazar fields. I. Photometric sequences for 10 BL Lacertae objects. A&A, 130:305–310, June 1998.
- [99] N. Gehrels et al. The Swift Gamma-Ray Burst Mission. Astrophys. J., 611:1005–1020, August 2004.
- [100] W. B. Atwood et al. The large area telescope on the fermi gamma-ray space telescope mission. Astrophys. J., 697(2):1071, 2009.
- [101] Charles Meegan et al. The Fermi Gamma-Ray Burst Monitor. Astrophys. J., 702:791–804, 2009.
- [102] A. A. Abdo et al. The First Catalog of Active Galactic Nuclei Detected by the Fermi Large Area Telescope. Astrophys. J., 715:429–457, 2010.
- [103] A. A. Abdo et al. Fermi Large Area Telescope Bright Gamma-ray Source List. Astrophys. J. Suppl., 183:46–66, 2009.



- [104] A. A. Abdo et al. Gamma-ray light curves and variability of bright fermi-detected blazars. Astrophys. J., 722(1):520, 2010.
- [105] A. A. Abdo et al. Bright AGN Source List from the First Three Months of the Fermi Large Area Telescope All-Sky Survey. Astrophys.J., 700:597–622, 2009.
- [106] Henric Krawczynski, D.A. Carter-Lewis, C. Duke, J. Holder, G. Maier, et al. Gamma-Hadron Separation Methods for the VERITAS Array of Four Imaging Atmospheric Cherenkov Telescopes. Astropart.Phys., 25:380–390, 2006.
- [107] M.F. Cawley et al. Exper. Astron., 173:1, 1990.
- [108] Robert W. Atkins et al. Tev gamma-ray survey of the northern hemisphere sky using the milagro observatory. Astrophys. J., 608(2):680, 2004.
- [109] Andres Sandoval et al. Performance of the first prototype of the HAWC Gamma Ray Observatory. In 2009 Fermi Symposium, 2009. arXiv:0912.3329.
- [110] F. Halzen and D. Hooper. High-energy neutrino astronomy: the cosmic ray connection. Reports on Progress in Physics, 65:1025–1078, July 2002.
- [111] A. Achterberg et al. First year performance of the IceCube neutrino telescope. Astropart. Phys., 26:155–173, 2006.
- [112] R. Abbasi et al. Calibration and Characterization of the IceCube Photomultiplier Tube. Nucl. Instrum. Meth., A618:139–152, 2010.
- [113] R. Abbasi et al. The IceCube Data Acquisition System: Signal Capture, Digitization, and Timestamping. Nucl. Instrum. Meth., A601:294–316, 2009.

- [114] Serap Tilav et al. Atmospheric Variations as observed by IceCube. In Proc. of the 31st Int. Cosmic Ray Conf, Lodz, Poland, Jul 2009. arXiv:1001.0776.
- [115] M. Ackermann et al. Optical properties of deep glacial ice at the South Pole. J. Geophys. Res., 111:D13203, 2006.
- [116] P.B. Price, K. Woschnagg, and D. Chirkin. Age vs depth of glacial ice at South Pole. Geophys. Res. Lett., 27:2129, 2000.
- [117] Harold and Yepes-Ramirez. Water absorption length measurement with the antares optical beacon system. Nuclear Instruments and Methods in Physics Research Section A: Accelerators, Spectrometers, Detectors and Associated Equipment, 626-627, Supplement(0):S118 – S119, 2011.
- [118] D. Chirkin et al. Study of south pole ice transparency with icecube flashers. In Proc. of the 32nd Int. Cosmic Ray Conf., Beijing, China, Aug 2011.
- [119] F. James and M. Roos. Minuit - a system for function minimization and analysis of the parameter errors and correlations. Computer Physics Communications, 10:343–367, December 1975.
- [120] The AMANDA Collaboration: J. Ahrens. Muon track reconstruction and data selection techniques in amanda. NUCL.INSTRUM.METH.A, 524:169, 2004.
- [121] Till Neunhoffer. Estimating the angular resolution of tracks in neutrino telescopes based on a likelihood analysis. Astropart. Phys., 25:220–225, 2006.
- [122] Jonathan Dumm. Searches for Point-like Sources of Neutrinos with the 40-String IceCube Detector. PhD thesis, University of Wisconsin, Madison, April 2011.

- [123] Jim Braun et al. Methods for point source analysis in high energy neutrino telescopes. Astropart. Phys., 29:299–305, 2008.
- [124] Jim Braun et al. Time-Dependent Point Source Search Methods in High Energy Neutrino Astronomy. Astropart. Phys., 33:175–181, 2010.
- [125] J. Neyman. Outline of a theory of statistical estimation based on the classical theory of probability. Phil. Trans. Royal Soc. London, Series A, 236:333–80, 1937.
- [126] Gary J. Feldman and Robert D. Cousins. A Unified Approach to the Classical Statistical Analysis of Small Signals. PRD, 57:3873–3889, 1998.
- [127] Jan Conrad, O. Botner, A. Hallgren, and Carlos Perez de los Heros. Including systematic uncertainties in confidence interval construction for Poisson statistics. Phys.Rev., D67:012002, 2003.
- [128] Gary C. Hill. Comment on 'Including systematic uncertainties in confidence interval construction for Poisson statistics'. Phys.Rev., D67:118101, 2003.
- [129] Askhat Gazizov and Marek P. Kowalski. ANIS: High energy neutrino generator for neutrino telescopes. Comput. Phys. Commun., 172:203–213, 2005.
- [130] H. L. Lai et al. Global QCD analysis of parton structure of the nucleon: CTEQ5 parton distributions. Eur. Phys. J., C12:375–392, 2000.
- [131] D. Heck, J. Knapp, J. N. Capdevielle, G. Schatz, and T. Thouw. CORSIKA: a Monte Carlo code to simulate extensive air showers. February 1998.

- [132] Eun-Joo Ahn, Ralph Engel, Thomas K. Gaisser, Paolo Lipari, and Todor Stanev. Cosmic ray interaction event generator SIBYLL 2.1. Phys.Rev., D80:094003, 2009.
- [133] Dmitry Chirkin and Wolfgang Rhode. Muon Monte Carlo: A high-precision tool for muon propagation through matter. 2004. hep-ph/0407075.
- [134] Johan Lundberg et al. Light tracking for glaciers and oceans: Scattering and absorption in heterogeneous media with photonics. Nucl. Instrum. Meth., A581:619–631, 2007.
- [135] G. D. Barr et al. A three-dimensional calculation of atmospheric neutrinos. Phys. Rev. D, 70:023006, 2004.
- [136] A. A. Abdo et al. Early Fermi Gamma-ray Space Telescope Observations of the Quasar 3C 454.3. Astrophys. J., 699:817–823, 2009.
- [137] Jeffrey D. Scargle. Studies in astronomical time series analysis. v. bayesian blocks, a new method to analyze structure in photon counting data. Astrophys. J., 504(1):405, 1998.
- [138] E. Resconi et al. On the classification of flaring states of blazar. Astron. Astrophys., 502:499–504, 2009.
- [139] Ana Pichel. Highlights from the Whipple 10-m VHE Blazar Monitoring Program. In Proc. of the 31st Int. Cosmic Ray Conf., Lodz, Poland, Jul 2009. arXiv:0908.0010.
- [140] V. A. Acciari et al. Multiwavelength observations of a TeV-Flare from W Comae. Astrophys. J., 707:612–620, 2009.

- [141] D. Mazin et al. Discovery of Very High Energy gamma-rays from the famous blazar S5 0716+714. In Proc. of the 31st Int. Cosmic Ray Conf, Lodz, Poland, Jul 2009.
- [142] N. Rea et al. The first outburst of the new magnetar candidate sgr0501+4516. Mon. Not. Roy. Astron. Soc., 396(4):2419–2432, 2009.
- [143] V. A. Acciari et al. Discovery of Variability in the Very High Energy Gamma-Ray Emission of 1ES 1218+304 with VERITAS. Astrophys. J., 709:L163–L167, 2010.
- [144] J. Albert et al. Variable very high energy gamma-ray emission from the microquasar LS I +61 303. Science, 312:1771–1773, 2006.
- [145] Felix A. Aharonian, Luis A. Anchordoqui, Dmitry Khangulyan, and Teresa Montaruli. Microquasar LS 5039: A TeV gamma-ray emitter and a potential TeV neutrino source. J.Phys.Conf.Ser., 39:408–415, 2006.
- [146] R. Abbasi et al. First Neutrino Point-Source Results From the 22-String IceCube Detector. Astrophys. J., 701:L47–L51, 2009.
- [147] A. A. Abdo. Modulated High-Energy Gamma-Ray Emission from the Microquasar Cygnus X-3. Science, 326(5959):1512–1516, 2009.
- [148] C. Brocksopp, A. E. Tarasov, V. M. Lyuty, and P. Roche. An improved orbital ephemeris for Cygnus X-1. A&A, 343:861–864, March 1999.
- [149] V. A. Acciari et al. VERITAS Observations of the gamma-Ray Binary LS I +61 303. Astrophys. J., 679:1427, 2008. arXiv:astro-ph/0802.2363.

- [150] Ethan T. Neil, Charles D. Bailyn, and Bethany E. Cobb. IR Monitoring of the Microquasar GRS 1915+105: Detection of Orbital and Superhump Signatures. Astrophys. J., 657:409–414, 2007.
- [151] T. C. Hillwig and D. R. Gies. Spectroscopic observations of the mass donor star in ss 433. Astrophys. J. Lett., 676(1):L37, 2008.
- [152] Jeffrey E. McClintock et al. Multiwavelength Spectrum of the Black Hole XTE J1118+480 in Quiescence. Astrophys. J., 593:435, 2003.
- [153] N. A. Webb, T. Naylor, Z. Ioannou, P. A. Charles, and T. Shahbaz. A TiO study of the black-hole binary GRO J0422+32 in a very low state. Mon. Not. Roy. Astron. Soc., 317:528, 2000.
- [154] C. Distefano, D. Guetta, E. Waxman, and A. Levinson. Neutrino flux predictions for known galactic microquasars. Astrophys. J., 575:378–383, 2002.